DOT/FAA/AR-96/110

Office of Aviation Research
Washington, D.C. 20591

Evaluation of Lightweight Material Concepts for Aircraft Turbine Engine Rotor Failure Protection

July 1997

Final Report

U.S. Department of Transportation
Federal Aviation Administration

NOTICE

Technical Report Documentation P

1. Report No.	2. Government Accession No.	3. Recipient's Catalog No.
DOT/FAA/AR-96/110		

4. Title and Subtitle	5. Report Date
EVALUATION OF LIGHTWEIGHT MATERIAL CONCEPTS FOR AIRCRAFT TURBINE ENGINE ROTOR FAILURE PROTECTION	July 1997
	6. Performing Organization Code

7. Author(s)	8. Performing Organization Report No.
Dy D. Le	AIR-447200P

9. Performing Organization Name and Address	10. Work Unit No. (TRAIS)
U.S. Army Research Lab/Naval Air Warfare Center Aircraft Division-Trenton 1440 Parkway Ave. Trenton, NJ 08628-0176	1047
	11. Contract or Grant No. Interagency Agreement DTFA03-95-X-90010 and DTFA03-88-A-00029

12. Sponsoring Agency Name and Address			13. Type of Report and Period Covered
U.S. Department of Transportation Federal Aviation Administration Atlantic City International Airport New Jersey 08405	and	U.S. Army Research Laboratory Arsenal Street Watertown, MA 02171-0001	Final Report
			14. Sponsoring Agency Code AAR-430

15. Supplementary Notes

The FAA William J. Hughes Technical Center COTR is Bill Emmerling, AAR-431.

16. Abstract

Results of the evaluation of lightweight materials for aircraft turbine engine rotor failure protection are presented in this report. The program consisted of two phases. Phase 1 was an evaluation of a group of composite materials which could possibly contain the impact energies of 1.0×10^6 inch-pounds generated by T53 rotor fragments. Phase 2 refined system composition and weight of the optimum materials selected from phase 1 and determined their performance under elevated temperatures. Based on the results of phase 1, the aluminum lined fiberglass is the best system, so far. The Aramid system with an aluminum liner performed almost as effective as aluminum lined fiberglass under ambient conditions. Dry Kevlar performed better than Kevlar impregnated with phenolic resin. Under elevated temperatures, the performances of the aluminum lined fiberglass system, based on energy per weight and thickness, reduced by 50 and 33 percent respectively. An increase of 92 percent in containment ring weight and 304 percent in its thickness is required to compensate for the degradation of the fiberglass system performance under high temperatures. Fabric composite systems absorbed the kinetic energy of fragments through elastic deformation and interlaminated shear of composite layers.

17. Key Words	18. Distribution Statement
Rotor disc burst, Containment ring ,Rotor fragment Uncontained turbine engine failure, Tri-hub failure, Kevlar, Fiberglass, Aramid	This document is available to the public through the Nationa Technical Information Service, Springfield, Virginia 22161

19. Security Classif. (of this report)	20. Security Classif. (of this page)	21. No. of Pages	22. Price
Unclassified	Unclassified	86	

Form DOT F1700.7 (8-72) **Reproduction of completed page authorized**

PREFACE

The entire program was sponsored by the FAA William J. Hughes Technical Center, Atlantic City International Airport, New Jersey 08405. This report was prepared by the Naval Air Warfare Center Aircraft Division, Trenton, New Jersey 08628, according to the Interagency Agreement No. DTFA03-95-X-90010 agreed upon by the William J. Hughes Technical Center Atlantic City International Airport, NJ, and the Naval Air Warfare Center Aircraft Division-Trenton, NJ (NAWCAD-TRN). Monsieurs Bruce Fenton, Robert Pursel, John Reinhardt, and William Emmerling of the William J. Hughes Technical Center served as FAA program monitors for the program. Dr. Steve Petrie of the University of Massachusetts, Lowell, Massachusetts 01854, and Monsieurs John Deluca, and Jay Connors of the U.S. Army Research Laboratory (ARL), Aberdeen Proving Ground, Maryland 21005, served as Army program monitors for the development and fabrication of containment rings. Their contributions and assistance during this program were greatly appreciated.

Program managers at NAWCAD-TRN who were responsible for this program were James Salvino from 1989 through 1994 and Dy Le from 1994 to completion. Project engineers assigned were Tracy Russo and Robert Delucia.

The author would like to commend Monsieurs Edward Schaeffer, John Grotheer, Glenn Myers, Bruce Rymovich, and Paul Lane, NAWCAD-TRN's aircraft engine mechanics, for their hard work and dedication to the program. This program would not have been successfully completed without their professional support.

Rejected T53 second power turbine discs used in the burst tests were provided by the Corpus Christi Army Depot, Corpus Christi, Texas 78419. Ms. Robin Bonham processed and handled all disc shipments to NAWCAD-TRN. Her assistance and contributions were essential to the success of the program and were also greatly appreciated.

TABLE OF CONTENTS

LIST OF FIGURES

LIST OF TABLES

EXECUTIVE SUMMARY

The Federal Aviation Administration William J. Hughes Technical Center, Atlantic City International Airport, NJ, and the U.S. Army Research Laboratory (ARL), Watertown, Massachusetts, conducted research and development under an interagency agreement to identify the state-of-the-art lightweight material concepts that could provide suitable containment and/or isolation from the worst case small turbine engine rotor disc failure hazard. The Naval Air Warfare Center Aircraft Division, Trenton, NJ, was tasked by the William J. Hughes Technical Center and ARL to conduct rotor disc burst containment tests on the containment rings designed and fabricated by ARL. A fully bladed Textron-Lycoming T53-L-11 second stage engine power turbine rotor, was designed and modified to fail into three fragments in order to evaluate the containment materials. This program consisted of two phases:

1. The purpose of phase 1 was to screen a group of composite materials which possibly would be capable of containing the impact energies of 1.0×10^6 inch-pounds generated by T53 rotor fragments in the NAWCAD-TRN rotor spin chamber under the ambient condition. The results obtained from phase 1 were incorporated into phase 2.

2. The purpose of phase 2 was to refine system composition and weight of the materials selected from phase 1 to the minimum for the designated protection level under predetermined elevated temperatures. The service temperature required for the selected materials was between 500 and 1,000°F. The selected candidate materials, screened from phase 1, were experimentally evaluated as panels by high energy impact tests and later as cylindrical ring specimens in the NAWCAD-TRN rotor spin chamber under the elevated temperature of 500°F or higher.

1. INTRODUCTION.

The Naval Air Warfare Center Aircraft Division located in Trenton, New Jersey, was tasked by the FAA William J. Hughes Technical Center and the U.S. Army Research Laboratory to conduct the engine rotor containment tests in its rotor spin chamber. This program was sponsored by the William J. Hughes Technical Center under the Interagency Agreement DTFA03-95-X-90010 and DTFA03-88-A-00029. The purpose was to identify the state-of-the-art lightweight materials which could provide suitable containment and/or isolation from the worst case small turbine engine rotor failure hazard. These materials might be considered for possible use in helicopter turbine engine rotor containment structures.

Uncontained failure of engine rotating components in turbine engine aircraft is considered a serious safety hazard to occupants and to the aircraft itself. Rotating components include turbine, compressor, and fan disc, as well as blades and other rotating components. They can release high-energy fragments which are capable of penetrating the engine cowling and damaging the fuel tank, hydraulic lines, auxiliary power units, and other accessories.

According to the Aerospace Information Report 4003 (AIR-4003) prepared by the Society of Automobile Engineers (SAE) in 1987, there were a total of 315 uncontained rotor failures from 1976 to 1983 in commercial, general, and rotorcraft aviation. For events causing significant and severe commercial transport aircraft damage, 52 percent of uncontained rotor failures recorded were due to discs; 2 percent were caused by fan blades. In general aviation, two incidents were due to turbine blades and three were from turbine discs. In rotorcraft aviation, 93 percent of uncontained failures which resulted in significant and severe aircraft damage were due to discs and spacers.

The uncontained failure of a gas turbine engine rotor is defined as a rotor failure that produces fragments which penetrate and escape the confines of the engine casing. Based on field experience in the past, aircraft engine turbine and compressor discs usually fail into three fragments (tri-hub failure), approximately 120 degrees apart.

The William J. Hughes Technical Center, recognizing the threat, established the Aircraft Catastrophic Failure Prevention Research Program in complying with the Omnibus Reconciliation Act of 1990. This act requires that the FAA develop technologies and methods to assess the risk and to prevent defects, failures, and malfunctions of products, parts, processes, and articles manufactured for use in aircraft, engines, propellers, and appliances which could result in a catastrophic failure of an aircraft. In the area of turbine engine failure prevention, three tasks have been identified and are being performed: (1) failure characterization, (2) vulnerability assessment, and (3) mitigation.

Tasks 1 and 2 were not directly performed by NAWCAD-TRN and ARL and are not discussed in this report. The goals of task 3 include the development of analytical models which would simulate and evaluate the effectiveness of containment and shielding materials. Under the same task a parallel research effort is the evaluation of light weight ballistic armor materials and its technology to select materials that are cost-effective and, yet, are capable of containing or mitigating the potential damage of burst rotor fragments.

In response to the William J. Hughes Technical Center's initiative in the hazard threat protection area, task 3, NAWCAD-TRN and ARL proposed a composite material research and evaluation program which was divided into two phases. The first phase was to screen a group of material systems which consisted of high-temperature, ballistic, fiber materials. Some of those composite fiber materials, with different weaving patterns, were combined with different resins and/or metallic alloys. More than two composite material systems were selected for the second phase of the program when system composition and weight were refined to the minimum for the designated protection level. In the second phase, selected composite material systems were tested under a minimum temperature of 500 °F.

2. TEST PROGRAM.

Materials development, equipment development, fabrication technique, and testing of the generic containment rings against the fully bladed T53 second stage power turbine were critical and fully studied in this project. ARL developed the materials and fabrication techniques. NAWCAD-TRN performed all the spin burst tests of ARL's containment rings in a vacuum spin chamber. NAWCAD-TRN was also tasked, at the conclusion of the test

program, to analyze test results and write a final report for FAA publication. Three testing techniques were performed to determine the capability of a material for containing turbine rotor fragments: subscale rotor fragment simulation testing, full-scale simulation testing, and spin testing. A detailed explanation of the first two techniques may be found in reference 1.

2.1 MATERIAL DEVELOPMENT.

During the subscale rotor fragment simulation testing phase, a standard ballistic V_{50} impact criterion and test were used. This subscale test was selected because it was cost-effective and widely used. The baseline V_{50} ballistic criterion, a velocity for which a projectile would have 50 percent probability of penetrating and perforating a certain containment system thickness, was derived. Based on the previous NAWCAD-TRN's spin test data, a cast steel ring 1.0 inch long and 0.625 inch thick is capable of containing all rotor fragments generated from the General Electric T58 power turbine. This initial containment value, during this analytical process, was used. Existing ballistic data, experimentally determined by Mascianica [2] was also extrapolated to predict a V_{50} criterion of 2,000 feet per second. Before conducting a ballistic test of flat panels of candidate materials, a mathematical model using similitude analysis was developed to obtain a set of scaled factors of the actual rotor spin burst test conditions. The kinematic properties of the T53 second stage power turbine and of the prototype, the properties of candidate materials, and the responses of containment ring materials upon impact were incorporated in the analysis. The scaled factors obtained from the similitude analysis were then applied to the model for a ballistic test. A 20-mm smooth bore gun barrel and 20-mm masses which simulated the T53 turbine fragments were used for the subscale tests. The results of the tests were used to estimate the areal density required for the rotor spin burst tests conducted at NAWCAD-TRN. A detailed description of the mathematical model and V_{50} subscale tests are explained in reference 1.

Based on the results from the V_{50} subscale tests, a full-scale projectile testing was developed as a screening containment test before rotor spin burst testing began. The work involved single and triple full mass projectiles utilizing explosive devices. A detailed procedure and description of the experiments are explained in reference 1.

Seven general candidate material systems which include phenolic and polyester thermosetting resins were selected and compared against the all cast steel system for the full-scale projectile testing, table 1. Titanium 6AL-4V was the only metallic material which would be evaluated against steel due to lighter weight. High-strength fiberglass (S-2) and aramid (Kevlar 29) materials which have been extensively used in armor protection systems were also selected. Steel material was also used as a liner for fiberglass and phenolic and for fiberglass and polyester systems. Titanium was additionally used as a liner with aramid and phenolic system. A separate system which contained aramid impregnated with phenolic was also made. Two fiberglass composite systems were created: fiberglass fibers impregnated with polyester and fiberglass fibers impregnated with phenolic resin. Polyester and phenolic resin temperature capability is rated at approximately 350°F.

TABLE 1. INITIAL CONTAINMENT RING PROPERTY CHARACTERISTICS

Materials	Areal Density (psf)	Thickness (in)	Estimated Weight (lbs)	Weight Saving (%)
Cast Steel (300 BHN)	25.6	0.625	75.4	Baseline
Titanium (6AL-4V)	14.0	0.620	41.2	45.3
Steel-Fiberglass-Phenolic	19.3	0.953	56.8	24.7
Steel-Fiberglass-Polyester	19.3	0.953	56.8	24.7
Titanium-Aramid-Phenolic	12.4	1.110	36.4	51.7
Aramid-Phenolic	10.7	1.600	31.5	58.2
Fiberglass-Polyester	15.0	1.500	44.2	41.4

Fiberglass-Phenolic	15.0	1.500	44.2	41.4

Cast steel, 300 BHN, and titanium 6AL-4V were the metallic materials used in some containment rings and as liners in other fabric systems.

Aramid material selected for testing was 1500 denier Kevlar 29, 35 x 35, 2 x 2, 13.6 ounce per square yard basket-weave fabric. Three thousand denier Kevlar 29, 17 x 17, 13.6 ounce per square yard plain weave fabric was also used for testing.

The fiberglass material was a 24 ounce per square yard woven roving produced with high-strength S-2 grade fiberglass.

Table 1 contains the areal density and containment thickness results from the subscale and full-scale simulation testing.

2.2 EQUIPMENT DEVELOPMENT.

Several types of equipment were utilized to fabricate containment rings for testing at NAWCAD-TRN. A McClean Anderson model W-60, three-axis filament winder was used because of its large mandrel capacity. A different mandrel was designed and built to wind all composite containment rings which were 14 inches in diameter and 9 inches in axial length. It was capable of fabricating the three test specimens mentioned earlier. This mandrel could withstand the 100 pounds per square inch autoclave pressure required for processing the phenolic matrix materials. A fabric dispensing stand was also built to dispense the preimpregnated fabric with controllable tension. A compaction stand was constructed to improve the compaction of the materials as they were fed to the winding mandrel. Finally, a fabric splitting stand was also built to slit the preimpregnated fabric from its original width to the width required for the containment rings to be tested at NAWCAD-TRN rotor spin facility (RSF). Detail design, machining, and operation of these items of equipment are explained in reference 1.

2.3 RING FABRICATION TECHNIQUE.

Composite containment rings were fabricated from preimpregnated fabric. This was because fabric is easier to construct, and their ballistics properties are superior to those of filament wound yarns. The critical parameter is the ring thickness which must be precisely controlled to achieve uniformity. Two characteristics were required for achieving uniformity of ring thickness: controllable tension of fabric and fabric movement while being wound.

Several fabrication techniques were developed and attempted before making the test containment rings. Generally, the composite cylinders would have to be completely wound and cured before being machined to a final length. Wound and cured cylinders of fabric materials were then placed on the lathe and cut by a diamond cutting wheel to the exact length required.

The metallic systems were fabricated and machined to their final dimensions without a lengthy process as that of fabric systems. The metal lined composite containment rings were fabricated differently. One-sixteenth-inch-thick metallic liners were machined to their final dimensions and then were used as winding mandrels upon which the fabric materials were wound. The metallic liners remained within the composite system.

The details of the technique for each system is explained by Deluca [1].

3. ROTOR SPIN FACILITY (RSF).

3.1 RSF MISSION.

The rotor spin facility at NAWCAD-TRN features the U.S. Navy's largest spin chamber. The RSF's general mission is to provide the experimental support for the engine rotor stress analysis, rotor low- and high-cycle fatigue

evaluation, rotor structural integrity investigation, rotor burst characterization studies, and blade and disk containment evaluation.

The U.S. Navy aircraft propulsion component tests are conducted, under simulated engine conditions, to evaluate rotor stress distribution, critical stress locations, and crack initiation and propagation phenomena. RSF performs spin testing to evaluate exploratory and advanced development concepts as well as to verify component life prediction methodology developed by engine manufacturers. Spin testing of the U.S. Navy propulsion rotating components such as low-cycle fatigue and overspeed tests is used for qualification and release to production. Rotor vibration and diagnostics can be studied using a sophisticated diagnostic vibration instrument system. Centrifuge testing can be used to evaluate new materials for rotating components as well as for commercial containment applications.

3.2 RSF DESCRIPTION.

The facility has four vertical vacuum chambers which have different sizes to accommodate various sizes of rotor assemblies. The spin chamber has a removable lid which when removed allows access to the interior. The selected drive turbine and test vehicle assembly can be configured and built under the lid overhung from the steel tower located in the work-built area. The chamber lid and wall can accommodate various sizes of drive turbines, instrumentation sensors, and other accessories. Other component accessories such as high-speed cameras can be adapted to the spin chamber wall. A typical spin chamber has an outer cylindrical steel shell which has several ports, an air space, an inner laminated steel liner, and an inner containment chamber liner. Materials for the inner containment chamber liner may be wood, lead, or aluminum. The outer shell and inner liners are capable of absorbing up to 100 million in-lbs of the energy generated from rotor burst fragments when testing. Although all vacuum chambers can be modified to adapt various auxiliary equipment, the largest chamber is the only one which has been modified to accommodate a high-speed camera for the FAA containment burst tests. Figure 1 is the schematic of the largest chamber, 110 inches in working diameter and 72 inches in height. RSF is equipped with four oil seal vacuum pumps ranging from 15 to 20 hp. Each vacuum pump has the capacity of providing a spin chamber vacuum in millitorr. Air for the spin testing is provided by the axial/centrifugal and reciprocating air compressors which are capable of producing air flow rates from 750 to 4,050 cubic feet per minute (cfm).

The NEFF Series 4000 Differential Multiplexer is a complete high-speed analog data application system designed to capture real-time test data and output them to the RSF automatic data acquisition and computer system for processing. The system is capable of allowing simultaneous multiple tests and unattended operations and providing up to 256 channels. Data sampling and recording are performed at a controlled rate of 100 samples per second (s/s).

RSF is also equipped with four state-of-the-art strip chart recording and analyzing devices. Each system is capable of recording up to 8 channels and can be upgraded to a maximum of 32 channels. Failure events can be captured, plotted, and automatically stored in the 1-gigabyte hard disk drive. Each system has 16 megabytes of random access memory.

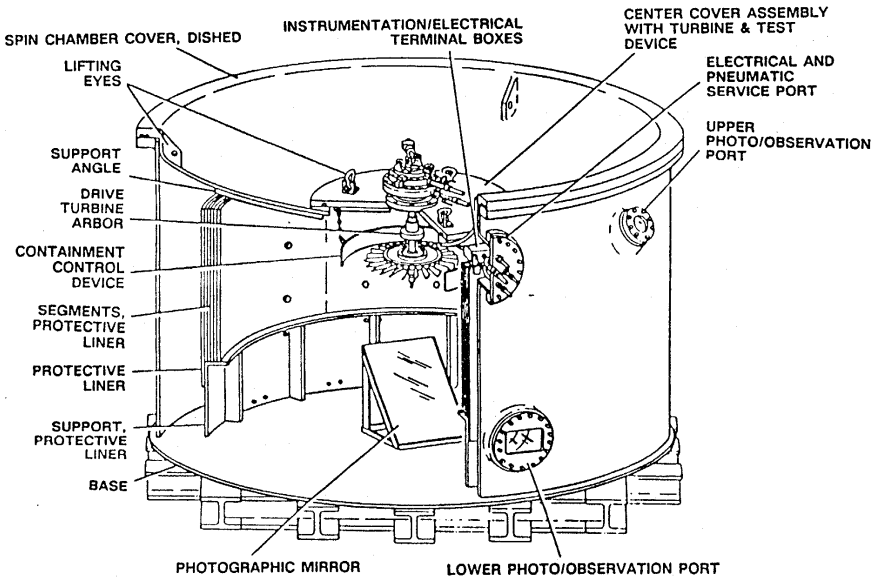

FIGURE 1. NAWCAD-TRN LARGEST SPIN CHAMBER

4. DESIGN OF TRI-HUB DISC FAILURE.

4.1 FRAGMENT ENERGY.

In order to evaluate the containment rings, fully bladed unserviceable Textron-Lycoming second power turbine wheels of the T53-L-13 engine were analyzed. They were designed to fail into three equal fragments at approximately 120 degrees apart and at a speed which was capable of producing a specific amount of kinetic energy at burst. The tri-hub rotor burst was designed to simulate the worst case failure of an actual turbine engine rotor. The burst energy of the rotor was selected to be 1.0×10^6 in-lbs which approximated the amount of the total kinetic energy produced by a turbine rotor of a medium-size commercial turboshaft engine. The calculated speed of this particular rotor, which produced 1.0×10^6 in-lbs of kinetic energy at burst, equated to approximately 20,400 rpm using equation 23 of appendix A. Figure 2 is a drawing of the T53-L-13 modified turbine rotor with its material properties. The slot terminal radius (STR) or b-cut was defined as the distance from the center of the turbine rotor to the end of the cut. Appendix A shows the derivations for the kinetic energy of disk fragments having a sector angle ϕ.

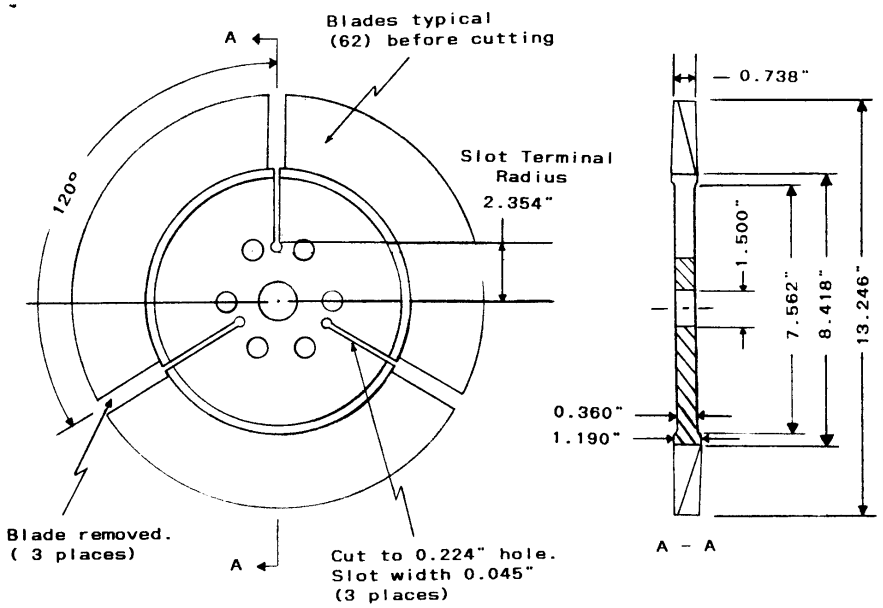

	DISK	BLADES	
ROTOR: T53-L-13 Power Turbine Materials	AMS-5509	AMS-5391	
DESCRIPTION: 3 Fragment Modification	PROPERTIES		
ROTOR WEIGHT: 10.80 lbs	SU (KPSI):	175	110 (min)
FRAGMENT CENTROIDAL DISTANCE: 3.235 inches	SY (KPSI):	125	100 (min)
FRAGMENT INERTIA (1/3): 54.61 lb-in^2	EU, t> 0.032 inch	8%	3%

FIGURE 2. T53 POWER TURBINE—THREE FRAGMENT MODIFICATION

Figure 3, which comes from equations 22-25 in appendix A, shows that the maximum translational kinetic energy (KE_t) of a fragment is obtained when the fragment sector angle is equal to 133.6 degrees. The total KE_t at this angle, however, is lower than the total KE_t as the sector angle becomes smaller or the number of fragments increases. In the design of the disk failure for the containment tests, the severe translational kinetic energy produced by a 120-degree disk fragment is interesting since the difference of KE_ts between the 120 and 133.6 degrees is insignificant. At the moment of the disk failure, KE_t of a one-third fragment reaches 21% and the rotational kinetic energy (KE_r) accounts for 12.3% of the total kinetic energy (KE). However, because of the fragment energy loss due to the friction from the rubbing of the disk against the containment ring, only approximately one-half (6.1%) of the rotational kinetic energy exists. Therefore, most of the damage to engine casings or other components is caused by the translational kinetic energy of the fragments. It should also be noted from figure 3 that the translational kinetic energy decreases and reaches zero as the fragment sector angle increases and reaches 360°. At this point, the total

energy comes completely from the rotational kinetic energy. On the other hand, as the number of fragments increases, the rotational kinetic energy of a fragment decreases and becomes small. KE_t, however, becomes larger and approaches its limit of 92.6%. At this limit KE_r is very small.

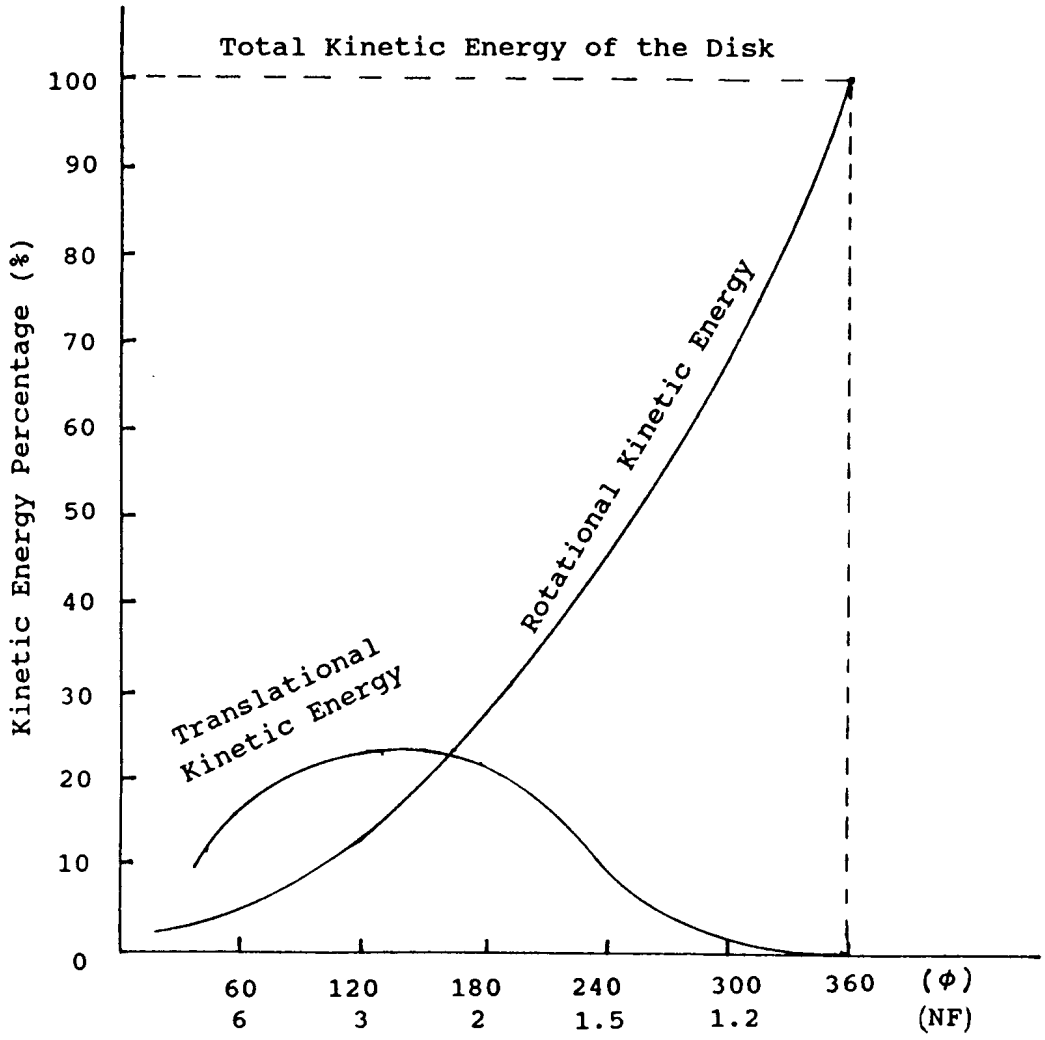

FIGURE 3. DISTRIBUTION OF TRANSLATIONAL AND ROTATIONAL KINETIC ENERGY OF ROTOR BURST FRAGMENT AS A FUNCTION OF FRAGMENT ANGLE (ϕ)

4.2 ROTOR FRAGMENT GENERATOR ANALYSIS.

Most of the experimental work on the rotor fragment generator had been performed at NAWCAD-TRN. Appendix B shows the detail of the analysis, extracted from reference 3, to come up with the notches to fail the T53 second power turbine into three equal pieces at a predetermined speed.

5. METHOD OF TEST.

A fully bladed Textron-Lycoming T53 second power turbine rotor, which was modified to fail into three equal fragments, was mounted to the spin chamber lid and connected to a Barbour Stockwell 8-inch air drive turbine by a Trans Torque coupling and an eight-inch drive spindle. The containment ring, 9 inches in axial length and 15 inches in inner diameter, designed and fabricated by ARL was freely suspended from mounting brackets and was concentrically positioned around the T53 engine power turbine rotor. Reflective tape was used on the bottom of the containment ring to illuminate the ring circumference and improve its dynamic images on 35-mm film when burst. The axial midsection of the ring was positioned to coincide with the rotor plane of rotation, and the radial clearance between the tip of the rotor blades and inner diametrical surface of containment ring was approximately 0.5 inch.

Figure 1 shows a typical test setup for the containment tests. The mounted rotor was placed inside the spin chamber which was evacuated to approximately 8 Torrs. The rotor was then accelerated to the burst speed of 20,400 rpm. To record the failure event on film, parallel foil stripes were attached on the inner perimeter of a containment ring in the plane of disc rotation. The lights were flashed when the parallel foils stripes were shorted by a rotor fragment upon failure. Two 12-million-candle power lights were used for the exposure. A high-speed framing camera, which was mounted through a port on the side of the spin chamber, was focused on the surface of a mirror which angled at 45 degrees and viewed the event from the bottom of the chamber. The spin chamber was completely dark with the camera aperture fully opened and the camera drum rotating at approximately 13,000 frames per second. When a failure occurred, the rotor released fragments made contact with the foil stripes on the inner surface of the ring. The contact interrupted the low voltage signal of the trip circuit which engaged the strobe lights thereby causing the failure events to be captured on film. Figure 4 is the typical sequence of the rotor failure measured in milliseconds just after the impact. The rotor speed was monitored by two independent magnetic pickups and displayed on the digital tachometers and graphic display terminals in the RSF control room. All parameters were visually monitored in the control room and recorded on a magnetic tape by the automatic data acquisition and processing system at a rate of 100 samples per second. Figure 5 is a typical plot of the speed versus time. The duration of the test normally lasted less than seventy seconds. At burst, a sudden drop of the load caused a jump in the speed of the drive turbine momentarily before the drive turbine sharply decelerated as seen in figure 5. Figure 6 shows a pretest picture of the fiberglass-phenolic ring. Figure 7 shows the pretest setup of the containment burst test taken in the radial direction of the ring. Figure 8 shows the pretest setup taken in the axial direction from the bottom of the ring. Notice the reflective tape at the bottom of the ring to make the circumferential cross section of the ring visible during burst event. Figure 9 is the picture of the containment ring and rotor fragments after failure. Figure 10 shows the picture of three equal pieces of failed rotor fragments.

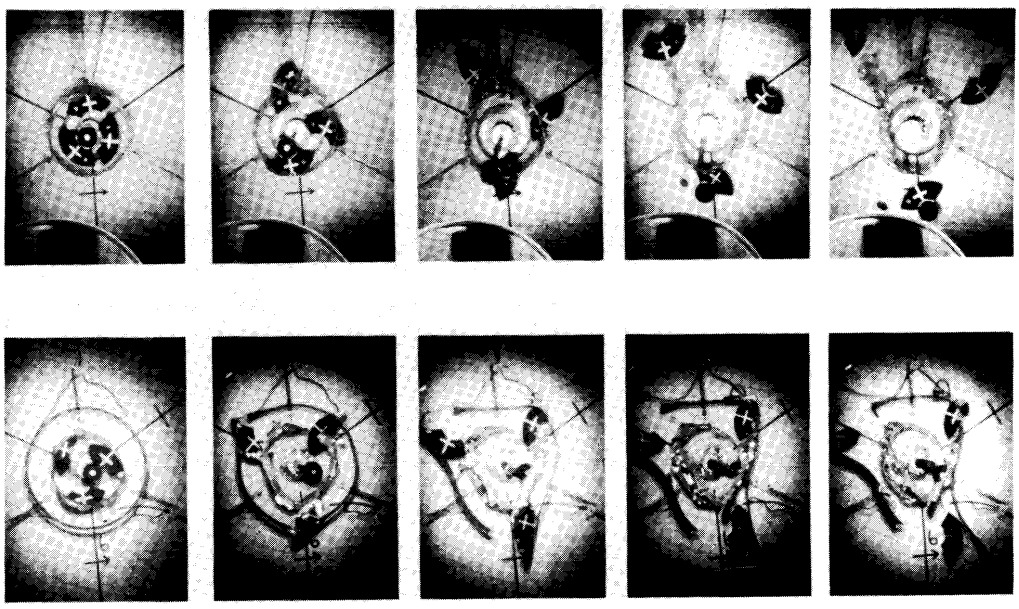

FIGURE 4. SEQUENCE OF ROTOR FAILURE MEASURED IN MILLISECONDS (MS)

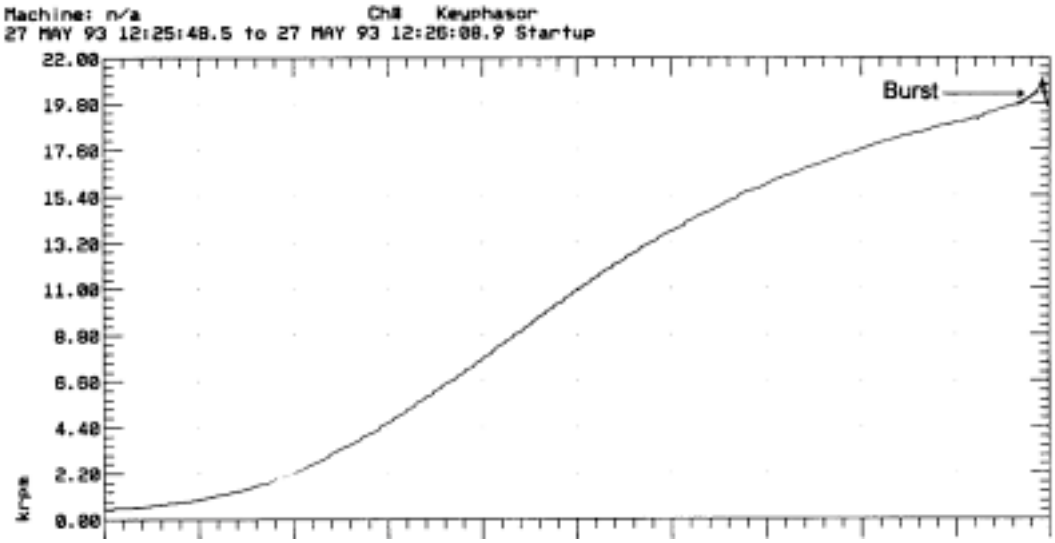

FIGURE 5. TYPICAL PLOT OF THE CONTAINMENT RING BURST TEST

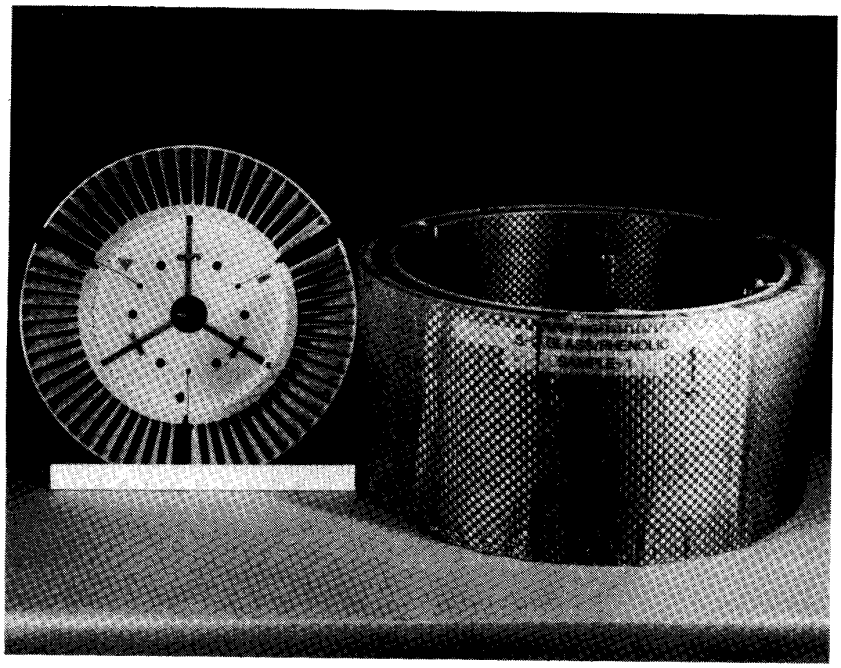

FIGURE 6. A TYPICAL CONTAINMENT RING AND A MODIFIED T53 TURBINE

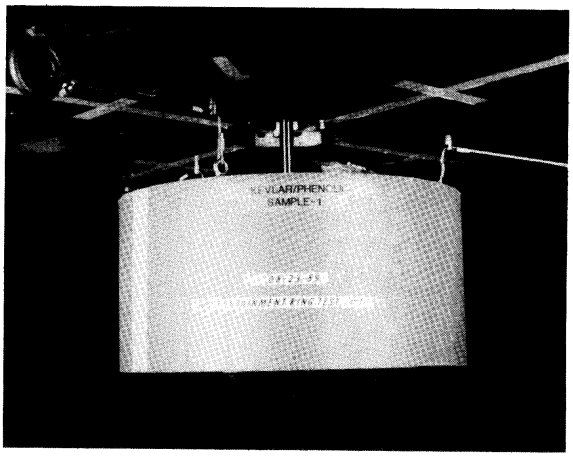

FIGURE 7. A TYPICAL CONTAINMENT RING BURST TEST SETUP (RADIAL DIRECTION)

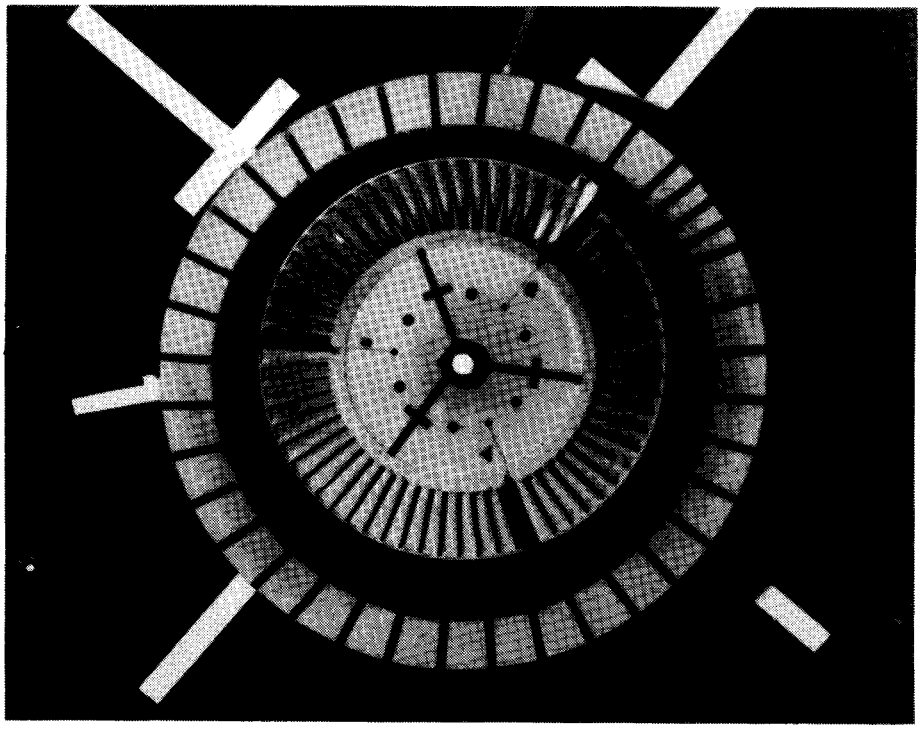

FIGURE 8. A TYPICAL CONTAINMENT RING BURST TEST SETUP (AXIAL DIRECTION)

FIGURE 9. A TYPICAL DEFORMED CONTAINMENT RING AFTER BURST

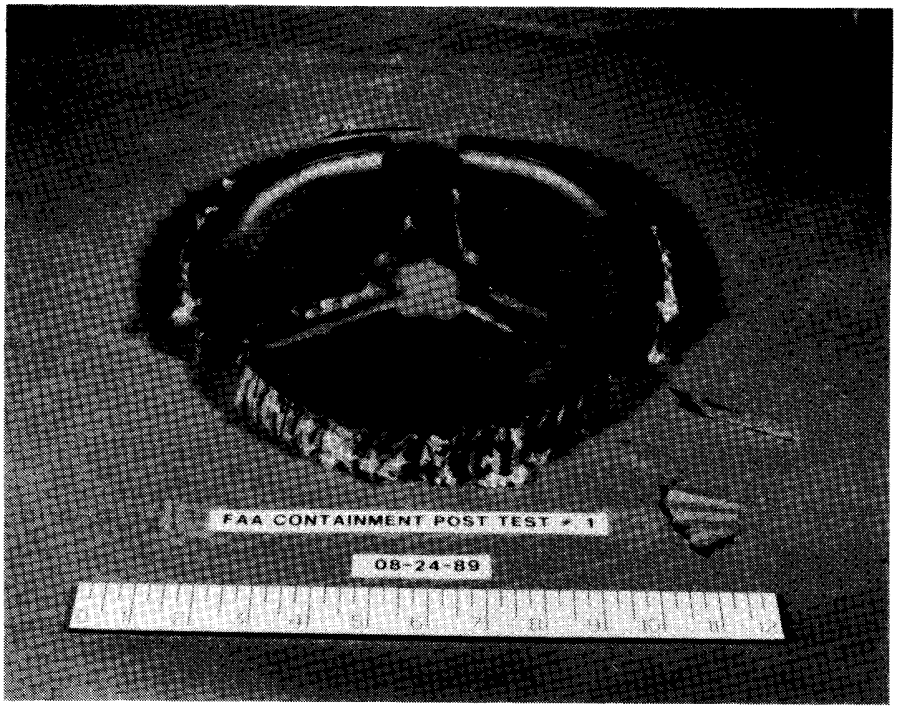

FIGURE 10. FAILED ROTOR FRAGMENTS

For heated burst tests in the range of 500-1,000°F, high-temperature and high-impedance silicon based adhesive was used to attach an aluminum foil stripe on the inner perimeter of the containment ring. Six Thermolyne Briskheat flexible electric heating tapes, four 620-watt, and two 836-watt tapes were used to cover the outer surface of the containment ring in the area where it would be in the same plane of disc rotation. Three J-typed thermocouples were installed. One thermocouple was attached on the inner surface of the containment ring. The second thermocouple was embedded in the middle of the ring and was on the same plane of rotation of the T53 rotor. The third thermocouple was attached on or close to the outer surface of the ring. Heat soaking was done under the vacuum. As soon as the whole ring temperature reached between 500-1,000°F, air drive would be introduced into the drive system to accelerate the T53 rotor to 20,400 rpm when the rotor would burst into three equal fragments.

6. CONTAINMENT RING DAMAGE ASSESSMENTS AND TEST RESULTS.

When a fully bladed disc burst, the containment ring might or might not contain all fragments. Sometimes, some of the blade debris escaped and penetrated the containment ring. This is due to the fact that the ring might not contain small and sharp-edge blade fragments because of its smaller local impact area. However, these blade debris were so small compared to the disc fragments that the residual energy might be insignificant. These debris might, hence, present no severe threat to the surrounding accessories.

Another phenomenon was that, during the burst event, blades were pushed through the rings by impacting rotor disc fragments. The blades could have penetrated through the containment ring thickness, but the rotor fragment might only embed inside the ring. Under these two situations, the ring would be considered to contain all disc fragments.

A thin aluminum sheet witness ring was used for each test to record the trajectory of rotor disc fragments which penetrated and escaped the containment ring. Sometimes, a fragment at burst impacted the inner ring surface, flipped over the top of the ring, penetrated the witness ring, and landed on the chamber floor outside the deformed ring.

The metallic and fiber composite material systems behaved differently upon being impacted by rotor fragments. All metallic material systems absorbed the kinetic energy of fragments through permanent deformation and failed either in perforation or in tensile as shown in figures 11 and 12. The fiber composite material systems, however, absorbed the kinetic energy of fragments through elastic deformation and interlaminated shear of composite layers. No evidence of tensile failure of fibers was found in tested fabric rings.

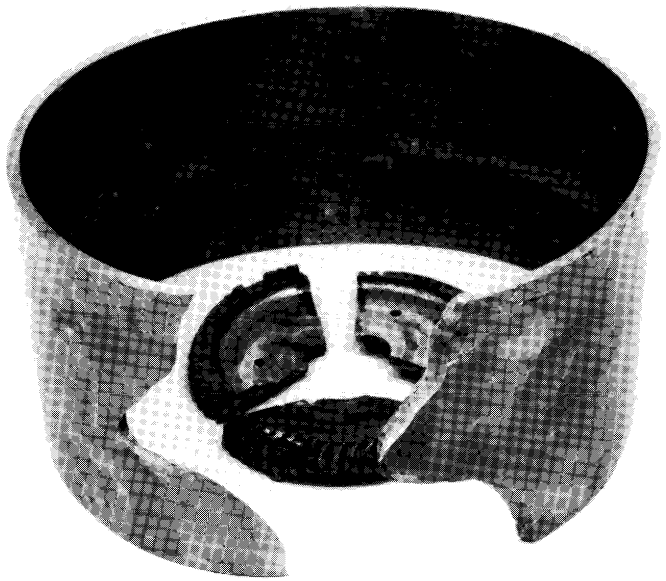

FIGURE 11. CONTAINMENT RING PERFORATION FAILURE

In the fiber composite material systems, when the fragments were impacting the inner surface of the fabric ring, they were still rotating and tended to unravel the wraps or layers in the direction
of their rotation. Because of this phenomenon, fabric layers were wrapped in the opposite direction of rotor rotation. This measure, however, did not eliminate the unraveling effect of the dry fabric containment ring as shown in figure 13.

FIGURE 12. CONTAINMENT RING TENSILE FAILURE (SOURCE: SALVINO 1977)

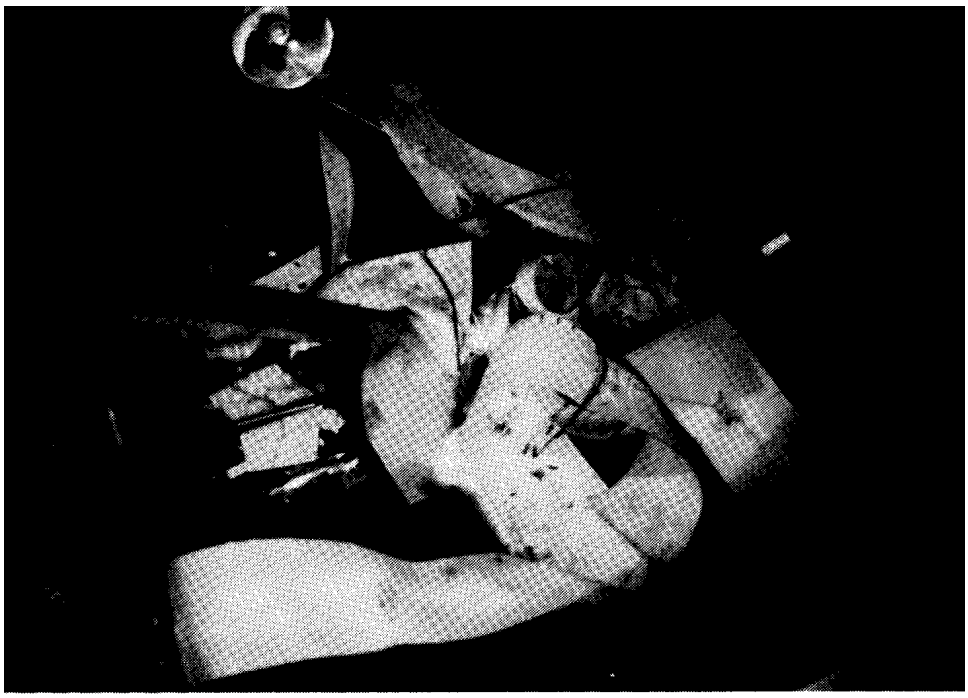

FIGURE 13. UNRAVELED EFFECT OF FABRIC CONTAINMENT RING

Another observation during testing is that, sometimes, high-speed photographs taken during the burst event of the fiber composite systems were not as definite and clear as that of all metallic systems. This is due to the small debris generated from the fabric containment ring.

The test results of candidate materials were analyzed and ranked in the order of their capability to contain the burst energy of rotor disk fragments. Containment is defined as the capability of the ring to fully contain all rotor fragments. The process is to define the threshold containment capability of each group of candidate material systems. This could be done by varying the weight, thickness, or the number of wraps of a candidate system until a system would contain all rotor fragments. However, since the burst speed was not exactly the same on every test, a containment ring system, in a group, which contained all fragments and provided the highest energy per weight was used for ranking. Two parameters which were not considered in the ranking were the number of wraps and weaving patterns due to insufficient data and records available.

Ranking was based on the energy per normalized weight (E/w_t), energy per thickness (E/t), and the combination of the energy per normalized weight and the energy per thickness. Containment ring normalized weight was obtained by multiplying the ratio of its weight per actual axial length to 9 inches. In aircraft design and application, weight is one of the critical criteria. The normalized weight of containment rings, therefore, would be of primary interest. The condition for the test results to be valid was that the generated energy must be greater than 925×10^3 in-lbs and less than $1{,}060 \times 10^3$ in-lbs. This range is based on the average burst energy of $992 \times 10^3 \pm 67 \times 10^3$ in-lbs for all tests conducted at NAWCAD-TRN. If the generated energy is greater than $1{,}060 \times 10^3$ in-lbs and the ring contained all fragments, the test was valid and included in the result.

Ranking was done by screening out all candidate systems which contained all rotor fragments. There were a total of 24 systems which met the containment criterion. A system which contained a threshold configuration or highest energy in each group was selected. This process gave ten different systems which contained all fragments. The system that had a highest energy per weight or energy per thickness, in this group of ten candidates, would be given a rank of ten. The containment ring material or composite system that had the highest weight ranking would be the best system. The system that had a lowest energy per weight or energy per thickness would be given a rank of one. A combined ranking per weight and per thickness could be obtained by multiplying the weight ranking of a system to its thickness ranking.

Table 2 shows all candidate systems with their characteristics and performance which had been tested in chronological order. Table 3 shows the results of containment tests, contained or not contained, of candidate composite materials and metals tested in group order. There were a total of ten groups. Table 4 shows rings which contained all rotor fragments.

TABLE 2. FAA/ARMY COMPOSITE MATERIALS

Ring No.	Materials	Weight (lbs)	Normal-ized Weight (lbs)	Radial Thickness (in)	Axial Length (in)	No. of High-Speed Photos	Failed Speed (rpm)	Contained (C) or Not Contained (NC)	Test Temp-erature (°F)
1	Kevlar 29-Phenolic	32.00	28.83	1.62	9.99	38	20400	C	ambient
2	Fiberglass-Phenolic	48.25	46.84	1.63	9.27	0	20400	C	ambient
3	Fiberglass-Polyester	49.00	47.52	1.65	9.28	44	20945	C	ambient
4	Ti-Kevlar-Phenolic	37.25	37.13	1.10	9.03	42	20700	C	ambient
5	Titanium (6A14V)	44.00	43.95	0.62	9.01	1	20550	C	ambient
6	Steel-Fiberglass-Phenolic	60.00	58.82	1.00	9.18	1	21400	C	ambient
7	Steel-Fiberglass-Polyester	65.75	63.90	1.20	9.26	28	20700	C	ambient
8	Titanium (6A14V)	27.25	26.37	0.40	9.30	1	20300	NC	ambient
9	Fiberglass-Polyester	36.75	36.51	1.18	9.06	40	20400	C	ambient
10	Fiberglass-Phenolic	34.00	34.00	1.07	9.00	40	21120	C	ambient
11	Kevlar 29-Phenolic	19.25	19.25	0.93	9.00	41	21400	NC	ambient
12	Ti-Kevlar-Phenolic	22.50	22.38	0.63	9.05	41	21080	NC	ambient
13	Steel-Fiberglass-Phenolic	35.00	35.00	0.63	9.00	42	21360	C	ambient
14	Steel-Fiberglass-Polyester	39.50	39.50	0.71	9.00	0	19040	C	ambient
15	Ti-Kevlar-Phenolic	27.50	27.50	0.73	9.00	37	20556	C	ambient
16	Kevlar 29-Phenolic	20.00	20.00	0.98	9.00	40	20665	NC	ambient
17	Fiberglass-Polyester	22.00	22.00	0.71	9.00	37	21584	C	ambient
18	Titanium (6A14V)	35.00	35.00	0.50	9.00	37	21583	C	ambient
19	Steel-Fiberglass-Polyester	29.00	29.00	0.59	9.00	37	19750	C	ambient
20	Fiberglass-Phenolic	18.50	18.50	0.58	9.00	37	20060	NC	ambient
21	Steel-Fiberglass-Phenolic	26.00	26.00	0.60	9.00	37	20570	NC	ambient
22	Kevlar 29	18.00	18.00	1.50	9.00	37	19760	C	ambient
23	Kevlar 29	24.00	21.60	1.56	10.00	0	15000	C	ambient
24	Fiberglass-Polyester	21.00	20.86	0.69	9.06	67	20583	C	ambient
25	Kevlar 29-Phenolic	22.50	22.50	1.67	9.00	4	21260	NC	ambient
26	Fiberglass-Phenolic	18.75	18.26	0.58	9.06	0	20280	C	ambient
27	Kevlar 29-Al Liner	24.75	24.08	1.5/0.063	9.25	0	20240	C	ambient
28	Fiberglass-Polyester	14.75	14.70	0.50	9.03	40	20640	NC	ambient
29	Kevlar 29-Al Liner	20.25	18.26	1.1/0.063	9.98	0	19800	C	ambient
30	Kevlar 29	17.00	13.91	1.10	11.00	38	20588	NC	ambient
31	Fiberglass-Al Liner	17.50	14.32	0.76	11.00	39	21280	NC	ambient
32	Kevlar 29-Al Liner	12.00	10.65	0.76	10.14	38	20140	NC	ambient
33	Kevlar 29-Al Liner	21.50	18.61	1.1/0.063	10.40	39	21300	C	ambient
34	Kevlar 29-Al Liner	18.50	16.00	0.96/0.063	10.40	38	19675	C	ambient
35	Fiberglass-Al Liner	23.50	20.53	0.95/0.063	10.30	39	20790	NC	ambient
36	Fiberglass-Al Liner	19.25	15.75	0.69/0.063	11.00	43	20500	C	ambient
37	Fiberglass-Al Liner	15.00	15.00	0.44/0.063	9.00	0	21700	NC	ambient

TABLE 3. FAA/ARMY COMPOSITE MATERIAL GROUPS

Group	Ring No.	Materials	Weight (lbs)	Normal-ized Weight (lbs)	Radial Thickness (in)	Axial Length (in)	No. of High-Speed Photos	Failed Speed (rpm)	Contained (C) or Not Contained (NC)	Test Temp-erature (°F)
1	31	Fiberglass-Al Liner	17.50	14.32	0.76	11.00	39	21280	NC	ambient
	35	Fiberglass-Al Liner	23.50	20.53	0.95/0.063	10.30	39	20790	NC	ambient
	36	Fiberglass-Al Liner	19.25	15.75	0.69/0.063	11.00	43	20500	C	ambient
	37	Fiberglass-Al Liner	15.00	15.00	0.44/0.063	9.00	0	21700	NC	ambient
2	2	Fiberglass-Phenolic	48.25	46.84	1.63	9.27	0	20400	C	ambient
	10	Fiberglass-Phenolic	34.00	34.00	1.07	9.00	40	21120	C	ambient
	20	Fiberglass-Phenolic	18.50	18.50	0.58	9.00	37	20060	NC	ambient
	26	Fiberglass-Phenolic	18.75	18.26	0.58	9.06	0	20280	C	ambient
3	3	Fiberglass-Polyester	49.00	47.52	1.65	9.28	44	20945	C	ambient
	9	Fiberglass-Polyester	36.75	36.51	1.18	9.06	40	20400	C	ambient
	17	Fiberglass-Polyester	22.00	22.00	0.71	9.00	37	21584	C	ambient
	24	Fiberglass-Polyester	21.00	20.86	0.69	9.06	67	20583	C	ambient
	28	Fiberglass-Polyester	14.75	14.70	0.50	9.03	40	20640	NC	ambient
4	22	Kevlar 29	18.00	18.00	1.50	9.00	37	19760	C	ambient
	23	Kevlar 29	24.00	21.60	1.56	10.00	0	15000	C	ambient
	30	Kevlar 29	17.00	13.91	1.10	11.00	38	20588	NC	ambient
5	27	Kevlar 29-Al Liner	24.75	24.08	1.5/0.063	9.25	0	20240	C	ambient
	29	Kevlar 29-Al Liner	20.25	18.26	1.1/0.063	9.98	0	19800	C	ambient
	32	Kevlar 29-Al Liner	12.00	10.65	0.76	10.14	38	20140	NC	ambient
	33	Kevlar 29-Al Liner	21.50	18.61	1.1/0.063	10.40	39	21300	C	ambient
	34	Kevlar 29-Al Liner	18.50	16.00	0.96/0.063	10.40	38	19675	C	ambient
6	1	Kevlar 29-Phenolic	32.00	28.83	1.62	9.99	38	20400	C	ambient
	11	Kevlar 29-Phenolic	19.25	19.25	0.93	9.00	41	21400	NC	ambient
	16	Kevlar 29-Phenolic	20.00	20.00	0.98	9.00	40	20665	NC	ambient
	25	Kevlar 29-Phenolic	22.50	22.50	1.67	9.00	4	21260	NC	ambient
7	6	Steel-Fiberglass-Phenolic	60.00	58.82	1.00 0.31/0.69	9.18	1	21400	C	ambient
	13	Steel-Fiberglass-Phenolic	35.00	35.00	0.63 0.18/0.45	9.00	42	21360	C	ambient
	21	Steel-Fiberglass-Phenolic	26.00	26.00	0.60 0.13/0.49	9.00	37	20570	NC	ambient
8	7	Steel-Fiberglass-Polyester	65.75	63.90	1.20 0.31/.89	9.26	28	20700	C	ambient
	14	Steel-Fiberglass-Polyester	39.50	39.50	0.71 0.19/0.52	9.00	0	19040	C	ambient
	19	Steel-Fiberglass-Polyester	29.00	29.00	0.59 0.12/0.47	9.00	37	19750	C	ambient
9	4	Ti-Kevlar-Phenolic	37.25	37.13	1.10 0.31/0.79	9.03	42	20700	C	ambient
	12	Ti-Kevlar-Phenolic	22.50	22.38	0.63	9.05	41	21080	NC	ambient
	15	Ti-Kevlar-Phenolic	27.50	27.50	0.73 0.25/0.48	9.00	37	20556	C	ambient
10	5	Titanium (6A14V)	44.00	43.95	0.62	9.01	1	20550	C	ambient
	8	Titanium (6A14V)	27.25	26.37	0.40	9.30	1	20300	NC	ambient
	18	Titanium (6A14V)	35.00	35.00	0.50	9.00	37	21583	C	ambient

TABLE 4. FAA/ARMY COMPOSITE MATERIAL RINGS (CONTAINED ALL FRAGMENTS)

Group	Ring No.	Materials	Normalized Weight (W_t) (lbs)	Radial Thickness (t) (in)	Failed Speed (rpm)	Kinetic Energy (KE) x1000 (in.lbs)	KE/W_t x1000 (in.lbs/lb)	KE/t x1000 (in.lbs/in)	Test Temperature ($^{\circ}$F)
1	36	Fiberglass-Al-Liner	15.75	0.75	20500	977	62	1303	ambient
2	2	Fiberglass-Phenolic	46.84	1.63	20400	968	21	594	ambient
	10	Fiberglass-Phenolic	34.00	1.07	21120	1038	31	970	ambient
	26	Fiberglass-Phenolic	18.62	0.58	20280	957	52	1650	ambient
3	3	Fiberglass-Polyester	47.52	1.65	20945	1021	21	619	ambient
	9	Fiberglass-Polyester	36.50	1.18	20400	968	26	820	ambient
	17	Fiberglass-Polyester	22.00	0.71	21584	1084	49	1527	ambient
	24	Fiberglass-Polyester	20.86	0.69	20583	986	47	1429	ambient
4	22	Kevlar 29	18.00	1.50	19760	908	50	605	ambient
	23	Kevlar 29	21.60	1.56	15000	523	24	335	ambient
5	27	Kevlar 29-Al Liner	24.08	1.53	20240	953	40	623	ambient
	29	Kevlar 29-Al Liner	18.26	1.19	19800	912	50	766	ambient
	33	Kevlar 29-Al Liner	18.61	1.16	21300	1055	57	910	ambient
	34	Kevlar 29-Al Liner	16.00	1.02	19675	901	56	883	ambient
6	1	Kevlar 29 -Phenolic	28.83	1.62	20400	968	34	598	ambient
7	6	Steel-Fiberglass-Phenolic	58.82	1.00	21400	1065	18	1065	ambient
	13	Steel-Fiberglass-Phenolic	35.00	0.63	21360	1061	30	1698	ambient
8	7	Steel-Fiberglass-Polyester	63.90	1.20	20700	996	16	831	ambient
	14	Steel-Fiberglass-Polyester	39.50	0.71	19040	843	21	1187	ambient
	19	Steel-Fiberglass-Polyester	29.00	0.57	19750	907	31	1591	ambient
9	4	Ti-Kevlar-Phenolic	37.13	1.10	20700	997	27	906	ambient
	15	Ti-Kevlar-Phenolic	27.50	0.73	20556	983	36	1347	ambient
10	5	Titanium (6A14V)	43.95	0.62	20550	982	22	1584	ambient
	18	Titanium (6A14V)	35.00	0.50	21583	1084	31	2168	ambient

Four dry fiberglass systems (rings 31, 35, 36, and 37), group 1, using aluminum liners were fabricated and tested. Ring 31 did not contain all fragments. As shown in the high-speed photographs, two fragments fully penetrated the outer layers of the containment ring at approximately 0.75 milliseconds. Ring 37 did not contain all fragments. One disc fragment penetrated the ring and escaped. Ring 36 contained all fragments. Its normalized weight was 15.75 lbs. Its radial thickness was 0.75 inch. The rotor burst at 20,500 rpm generating 62 kips/lb (10^3 in-lbs/lb) of kinetic energy per normalized weight (KE_w) and 1,303 kips/in of kinetic energy per thickness (KE_t). These values represented the threshold configuration of aluminum lined fiberglass system. Three fragments were embedded in the inner layers of the containment ring. Ring 35 was heavier and thicker. It did not, however, contain all fragments. The rotor burst at 20,790 rpm producing 1,005 kips of total kinetic energy. One disc fragment penetrated the ring and escaped. In both rings, 35 and 36, their weight and thickness were close to the design threshold and the overspeed burst increases the kinetic energy of the rotor fragments, which would be sufficient to penetrate the containment system. Additionally, containment ring performance may not be directly proportional to the ring thickness and the number of ply due to variations in fabrication technique. Figure 14 shows the posttest pictures of rings 31, 35, 36, and

37. Figure 15 shows the failure event of rings 31 and 36 recorded by the Cordin high-speed camera. Time at burst (t_b), the time when the trip circuit was hit by the blades momentarily after burst, was set at zero. Initial impact time was t_i, the time when the disc surface first impacted the inner surface of the ring. The time when one or all fragments just completely penetrated and escaped the containment ring outer surface was t_e. The duration of complete penetration was the period between t_i and t_e. Last recorded event shows the last picture recorded by the high speed camera at time t_l.

Figure 16 shows the threshold containment and a typical residual kinetic energy. The residual energy of the fragment leaving ring 31 was 13.3 kips. It was derived from the estimated penetrating duration taken from the high-speed film. Based on this approximation, the uncontained fragment was leaving ring 31 at the speed of approximately 1,690 inches per second, an equivalence of 96 miles per hour.

(1) RING 31

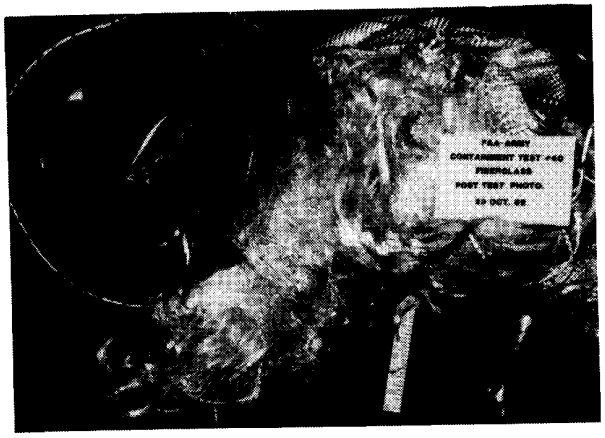

(2) RING 35

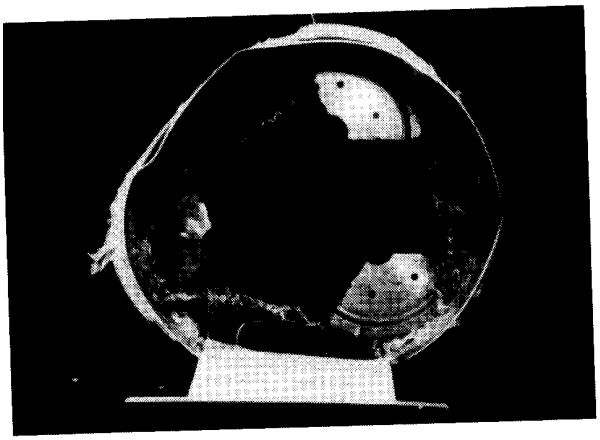

(3) RING 36

(4) RING 37

FIGURE 14. POSTTEST PICTURES OF RINGS 31, 35, 36, AND 37

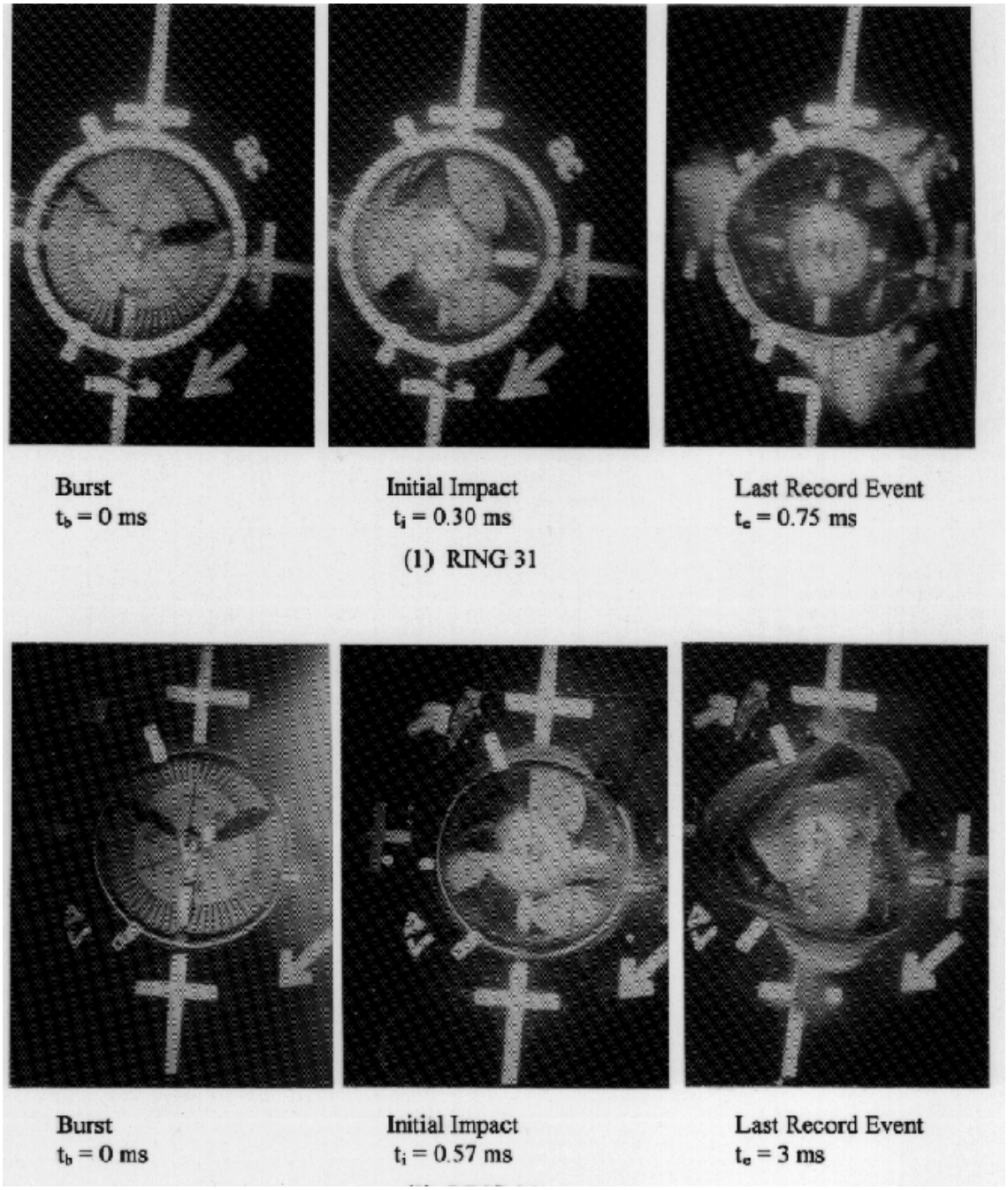

FIGURE 15. FAILURE EVENT OF RINGS 31 AND 36

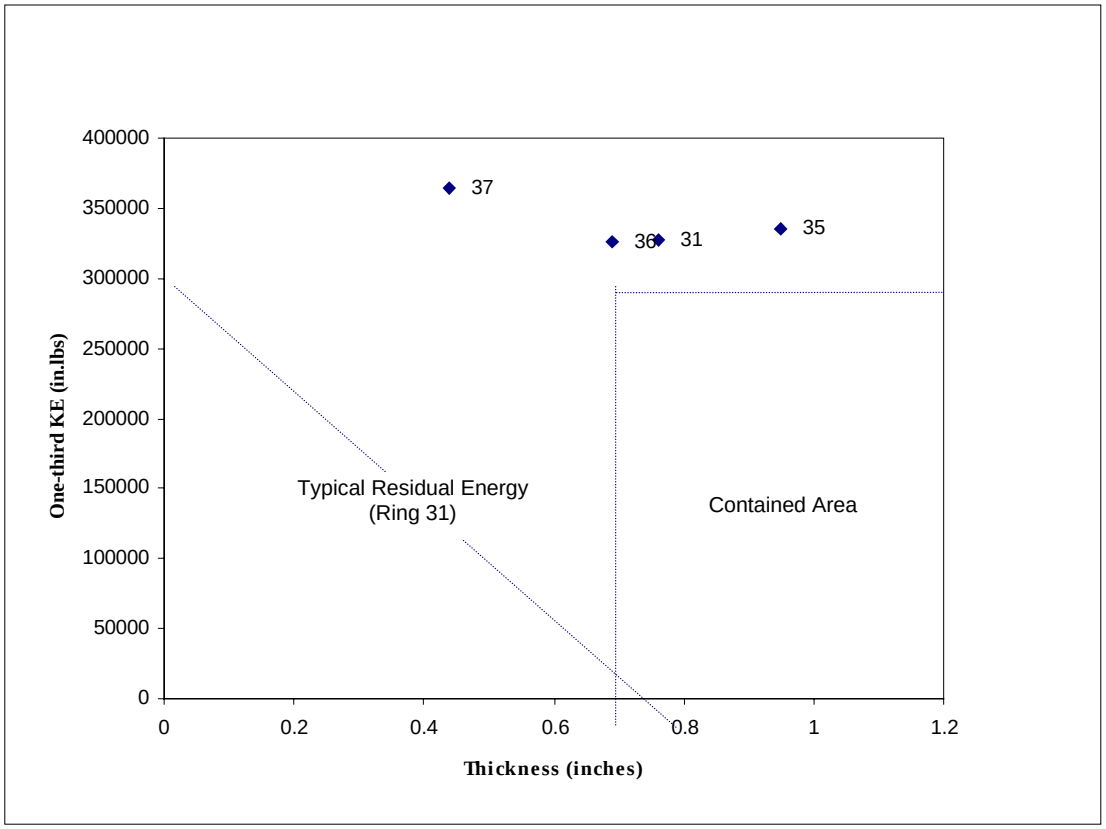

Group	Ring No.	Materials	Weight (lbs)	Normal-ized Weight (lbs)	Radial Thickness (in)	Axial Length (in)	No. of High-Speed Photos	Failed Speed (rpm)	Contained (C) or Not Contained (NC)	Test Temp-erature (°F)
1	31	Fiberglass-Al liner	17.50	14.32	0.76	11.00	39	21280	NC	ambient
	35	Fiberglass-Al liner	23.50	20.53	0.95/0.063	10.30	39	20790	NC	ambient
	36	Fiberglass- Al liner	19.25	15.75	0.69/0.063	11.00	43	20500	C	ambient
	37	Fiberglass-Al liner	15.00	15.00	0.44/.0063	9.00	0	21700	NC	ambient

FIGURE 16. GROUP 1—FIBERGLASS-ALUMINUM

Group 2, fiberglass impregnated with phenolic resin, had four systems (rings 2, 10, 20, and 26). Rings 2, 10, and 26 contained all fragments. Normalized weight and thickness of ring 2 were 46.84 lbs and 1.63 inches, ring 10 were 34.00 lbs and 1.07 inches, and ring 26 were 18.62 lbs and 0.58 inch respectively. KE_w and KE_t of ring 2 were 21 kips/lb and 594 kips/in, ring 10 were 31 kips/lb and 970 kips/in, and ring 26 were 52 kips/lb and 1,650 kips/in respectively. System 26 provided threshold values for this group. One disc fragment penetrated ring 20 and escaped. Rings 10 and 2 inner fiberglass layers were severely damaged. Two-thirds of the outer most layers were not significantly distorted. Figure 17 shows the posttest pictures of rings 2, 10, and 20. Figure 18 shows the failure event of ring 10. Figure 19 shows the contained area and threshold containment of group 2.

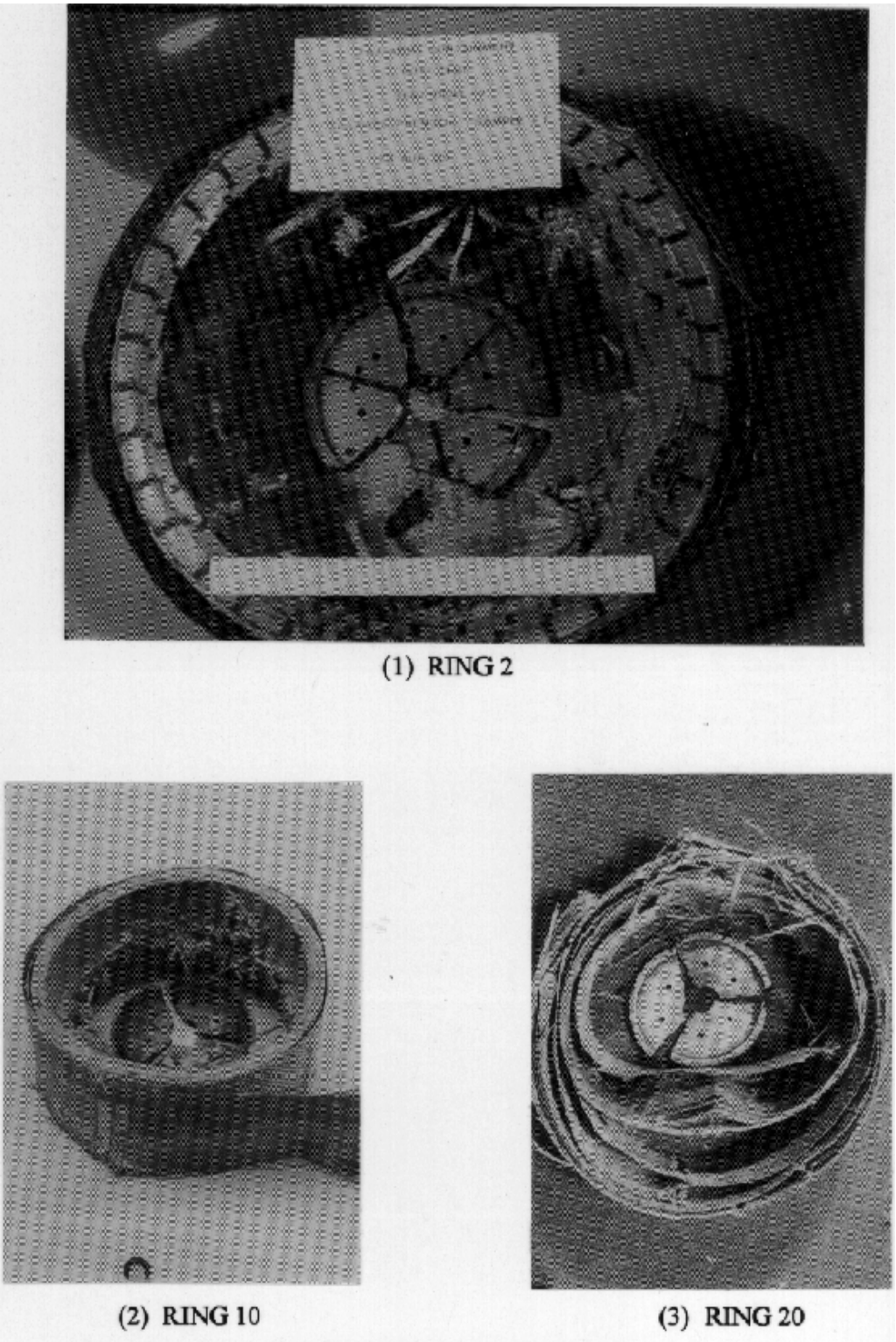

FIGURE 17. POSTTEST PICTURES OF RINGS 2, 10, AND 20

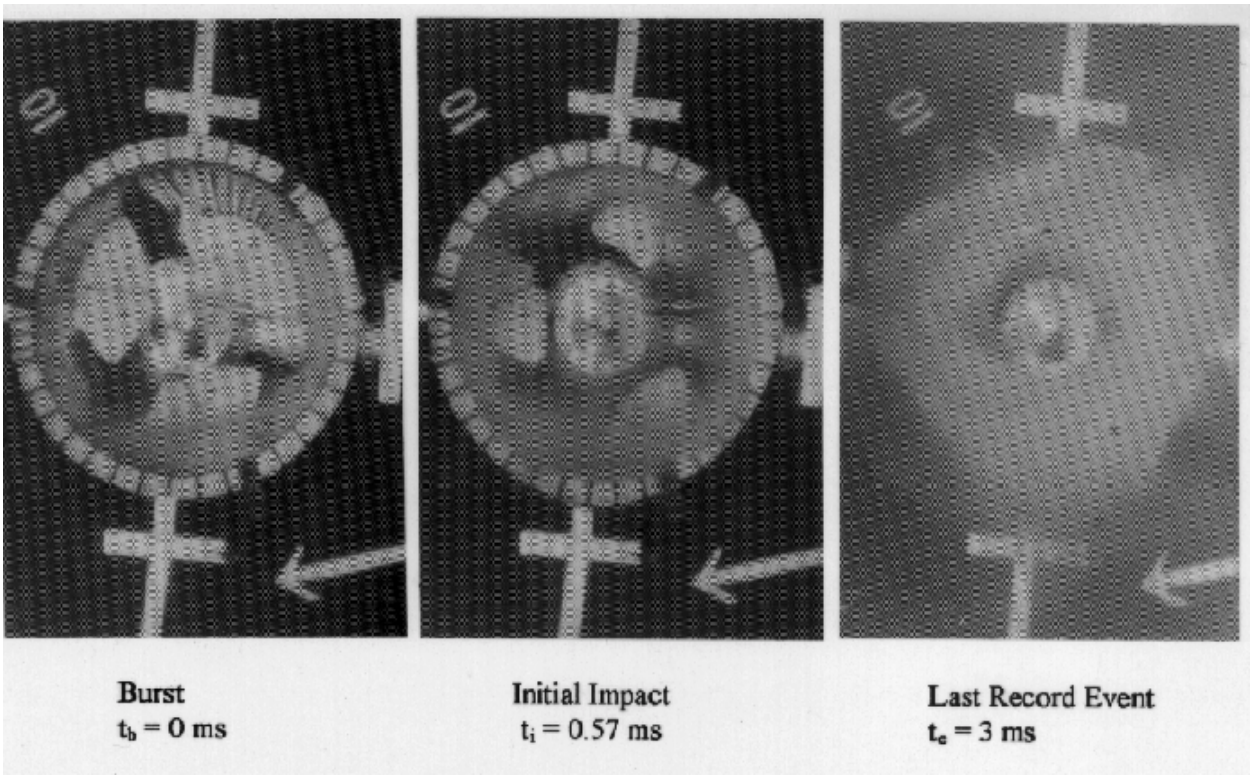

FIGURE 18. FAILURE EVENT OF RING 10

Group 3, fiberglass impregnated with polyester resin, had five systems (rings 3, 9, 17, 24, and 28). Rings 3, 9, 17, and 24 contained all fragments. No significant damage on the outer most layers of these rings was recorded. Normalized weight and thickness of ring 3 were 47.52 lbs and 1.65 inches, ring 9 were 36.50 lbs and 1.18 inches, ring 17 were 22.00 lbs and 0.71 inch, and ring 24 were 20.86 lbs and 0.69 inch respectively. KE_w and KE_t of ring 3 were 21 kips/lb and 619 kips/in, ring 9 were 26 kips/lb and 820 kips/in, ring 17 were 49 kips/lb and 1,527 kips/in, and ring 24 were 47 kips/lb and 1,429 kips/in respectively. System 24 represented the threshold configuration. System 17, however, provided higher energy absorbed per unit weight, and it was selected for ranking. One disc fragment penetrated ring 28 and escaped. Figure 20 shows the posttest pictures of rings 3, 9, and 17. Figures 21 and 22 show the failure event of ring 3, 9, 17, and 24. Figure 23 shows the failure event and posttest pictures of ring 28. Figure 24 shows the contained area of group 3. The residual energy of the fragment leaving ring 28 at the speed of 317 inches per second or 18 miles per hour was approximately 467 in-lbs.

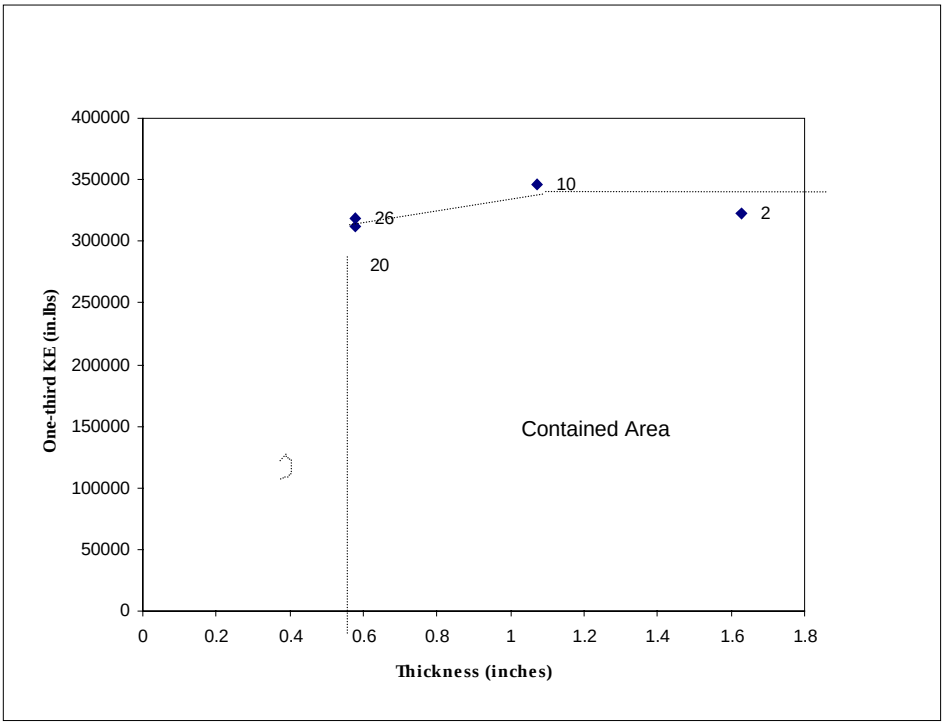

Group	Ring No.	Materials	Weight (lbs)	Normal-ized Weight (lbs)	Radial Thick-ness (in)	Axial Length (in)	No. of High-Speed Photos	Failed Speed (rpm)	Contained (C) or Not Contained (NC)	Test Temp-erature (˚F)
2	2	Fiberglass-phenolic	48.25	46.84	1.63	9.27	0	20400	C	ambient
	10	Fiberglass-phenolic	34.00	34.00	1.07	9.00	40	21120	C	ambient
	20	Fiberglass-phenolic	18.50	18.50	0.58	9.00	37	20060	NC	ambient
	26	Fiberglass-phenolic	18.75	18.26	0.58	9.06	0	20280	C	ambient

FIGURE 19. GROUP 2—FIBERGLASS-PHENOLIC

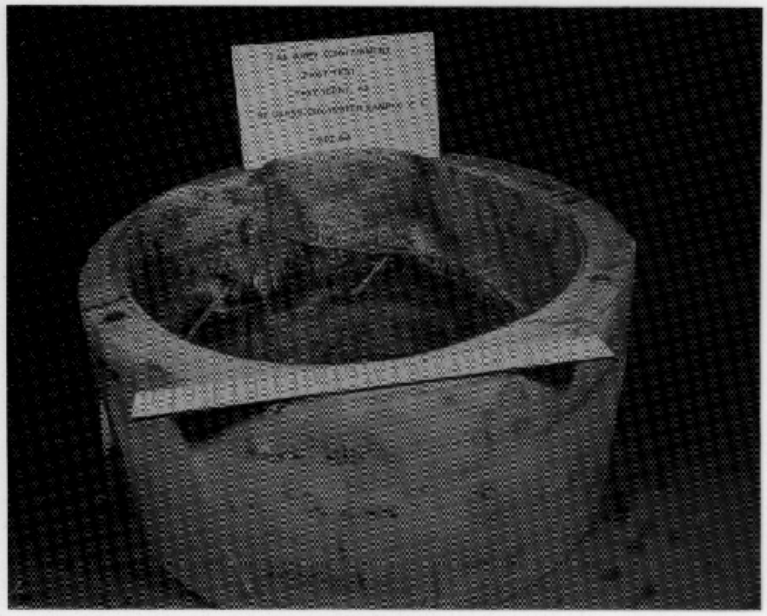

(1) RING 3

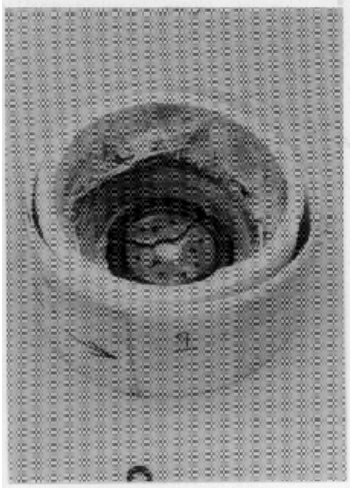

(2) RING 9

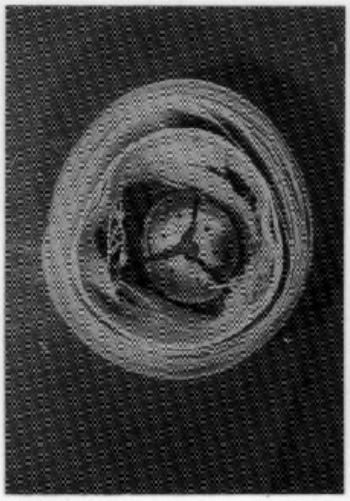

(3) RING 17

FIGURE 20. POSTTEST PICTURES
OF RINGS 3, 9, AND 17

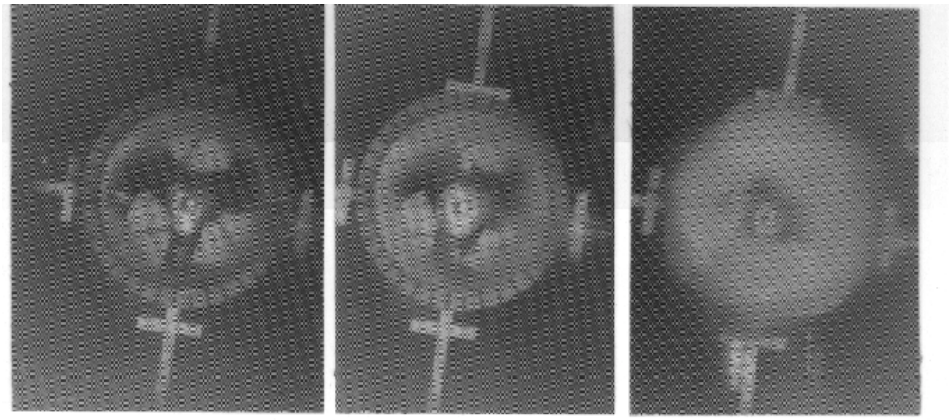

Burst
$t_b = 0$ ms

Initial Impact
$t_i = 0.24$ ms

Last Record Event
$t_l = 3$ ms

(1) RING 3

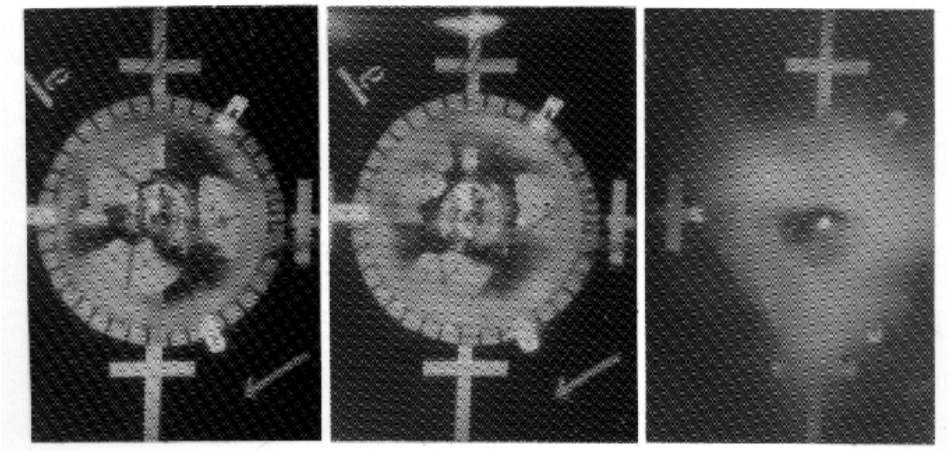

Burst
$t_b = 0$ ms

Initial Impact
$t_i = 0.27$ ms

Last Record Event
$t_l = 3$ ms

(2) RING 9

Figure 21. FAILURE EVENT OF RINGS 3 AND 9

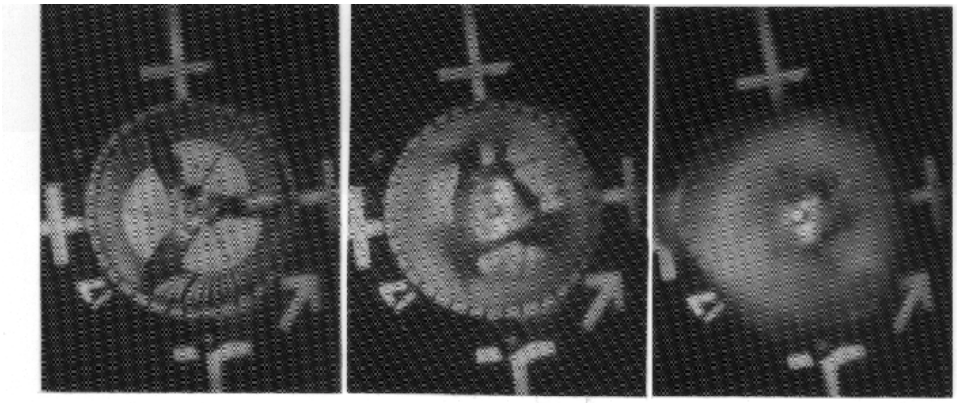

Burst
$t_b = 0$ ms

Initial Impact
$t_i = 0.32$ ms

Last Record Event
$t_l = 3$ ms

(1) RING 17

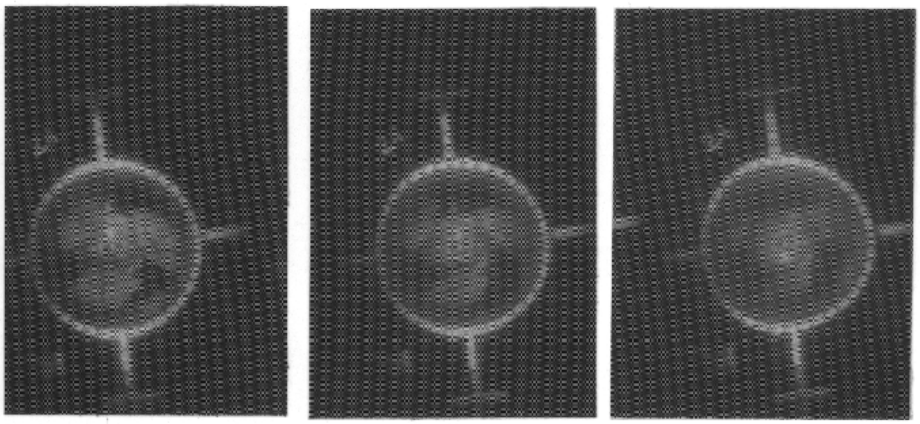

Burst
$t_b = 0$ ms

Initial Impact
$t_i = 0.18$ ms

Last Record Event
$t_l = 1.65$ ms

(2) RING 24

FIGURE 22 FIALURE EVENT OF RINGS 17 AND 24

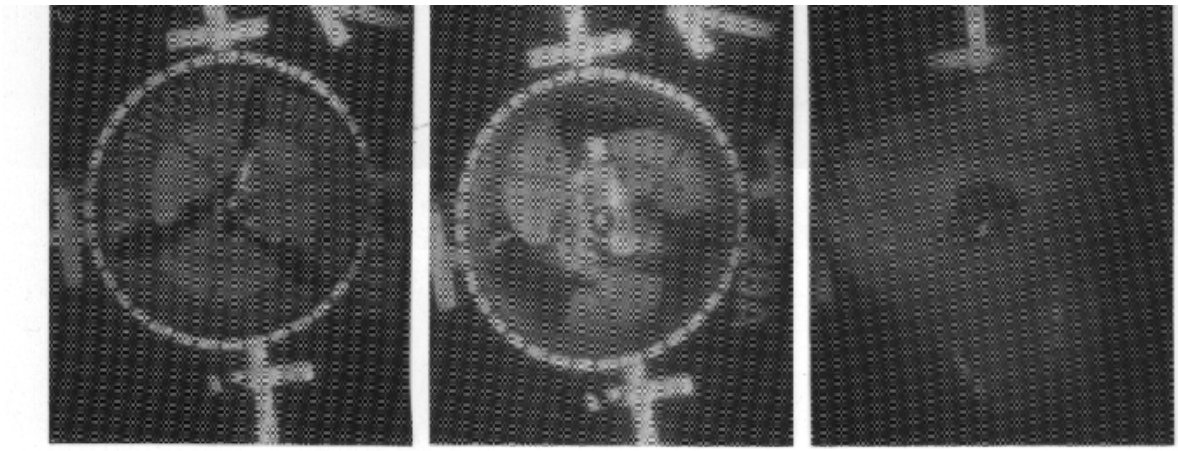

Burst
$t_b = 0$ ms

Initial Impact
$t_i = 30$ ms

Near Complete Penetration
$t_i = 1.88$ ms

(1) FAILURE EVENT OF RING 28

(2) RING 28

(3) WITNESS SHIELD

FIGURE 23. FAILURE EVENT AND POSTTEST PICTURES OF RING 28

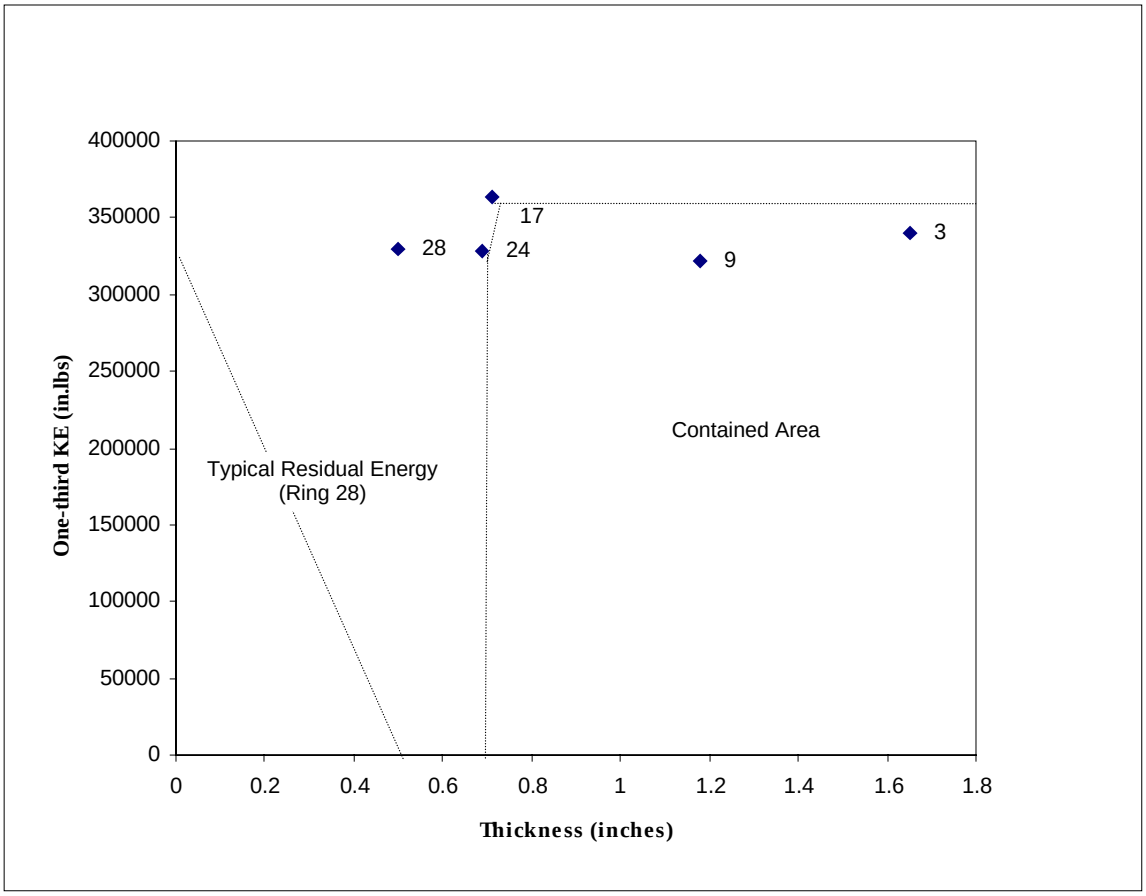

Group	Ring No.	Materials	Weight (lbs)	Normal-ized Weight (lbs)	Radial Thick-ness (in)	Axial Length (in)	No. of High-Speed Photos	Failed Speed (rpm)	Contained (C) or Not Contained (NC)	Test Temp-erature (°F)
3	3	Fiberglass-polyester	49.00	47.52	1.65	9.28	44	20945	C	ambient
	9	Fiberglass-polyester	36.75	36.51	1.18	9.06	40	20400	C	ambient
	17	Fiberglass-polyester	22.00	22.00	0.71	9.00	37	21584	C	ambient
	24	Fiberglass-polyester	21.00	20.86	0.69	9.06	67	20583	C	ambient
	28	Fiberglass-polyester	14.75	14.70	0.50	9.03	40	20640	NC	ambient

FIGURE 24. GROUP 3—FIBERGLASS-POLYESTER

Groups 4 and 5 had Kevlar 29 systems. The systems in group 4 did not have aluminum liners. Rings 22 and 23 contained all fragments. Normalized weight and thickness of ring 22 were 18.00 lbs and 1.50 inches and ring 23 were 21.60 lbs and 1.56 inches respectively. KE_w and KE_t of ring 22 were 50 kips/lb and 605 kips/in and ring 23 were 24 kips/lb and 335 kips/in respectively. System 22 therefore represented the threshold configuration for this group. One disc fragment penetrated ring 30 and escaped. Figure 25 shows the posttest pictures of rings 22 and 30. Figure 26 shows the failure event of ring 30.

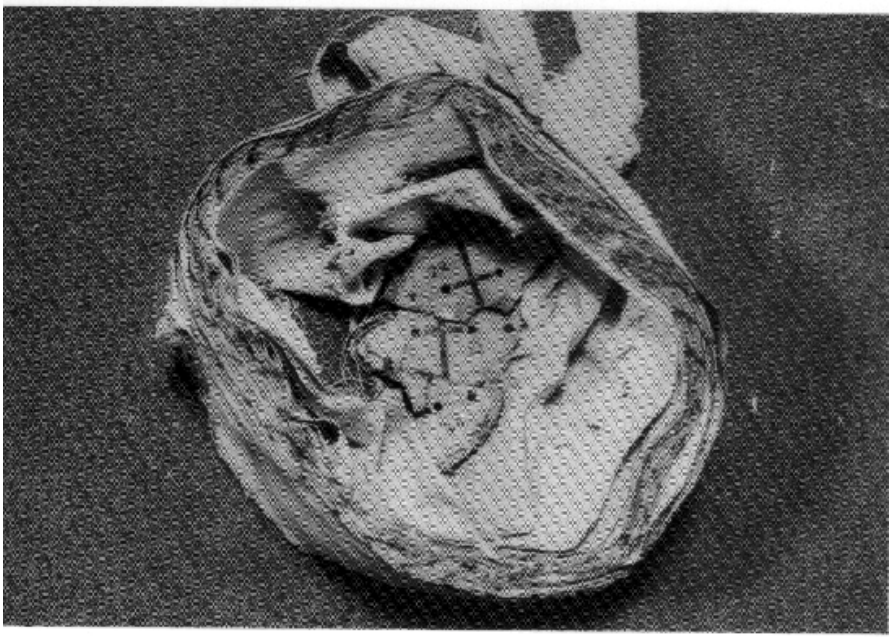

(1) RING 22

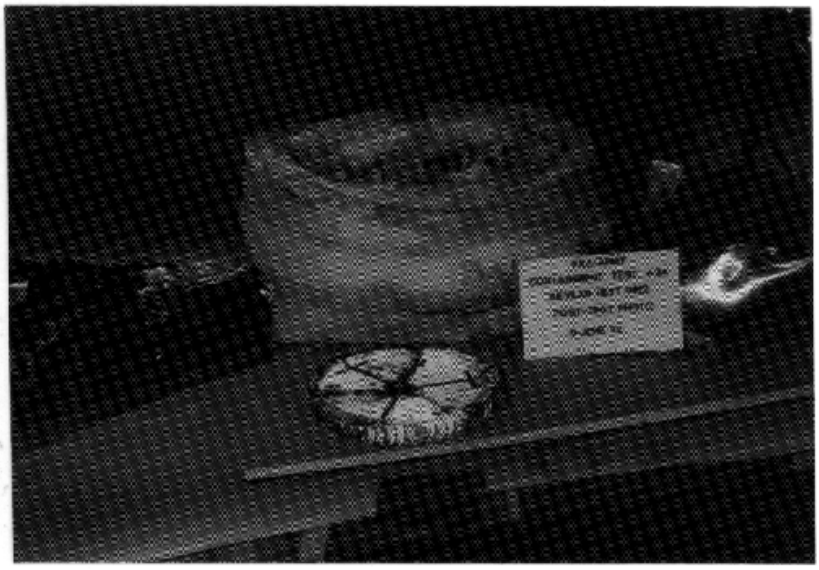

(2) RING 30

FIGURE 25. POSTTEST PICTURES OF RINGS 22 AND 30

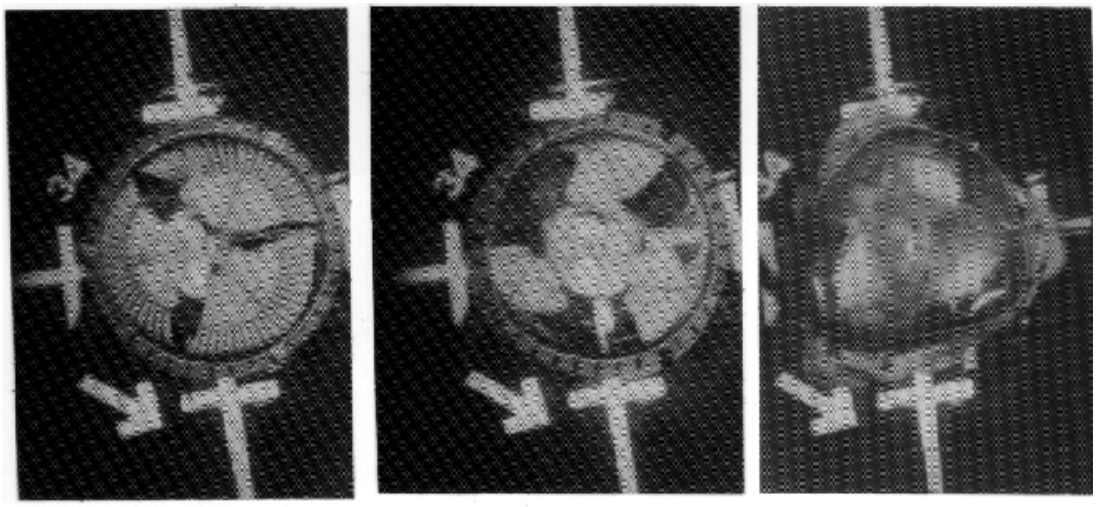

FIGURE 26. FAILURE EVENT OF RING 30

Figure 27 shows the contained area of group 4. The uncontained fragment was leaving ring 30 at the speed of approximately 399 inches per second or 23 miles per hour. Its residual energy was approximately 740 in-lbs.

Group 5 had four aluminum lined Kevlar systems (rings 27, 29, 33, and 34) which contained all fragments. Normalized weight and thickness of ring 27 were 24.08 lbs and 1.53 inches, ring 29 were 18.26 lbs and 1.19 inches, ring 33 were 18.61 lbs and 1.16 inches, and ring 34 were 16.00 lbs and 1.02 inches respectively. KE_w and KE_t of ring 27 were 40 kips/lb and 623 kips/in, ring 29 were 50 kips/lb and 766 kips/in, ring 33 were 57 kips/lb and 910 kips/in, and ring 34 were 56 kips/lb and 883 kips/in respectively. System 33 had the threshold values. One disc fragment penetrated rings 32 and 33. Figure 28 shows the posttest picture of rings 29, 32, 33, and 34. Figures 29 and 30 show the failure event of rings 32, 33, and 34.

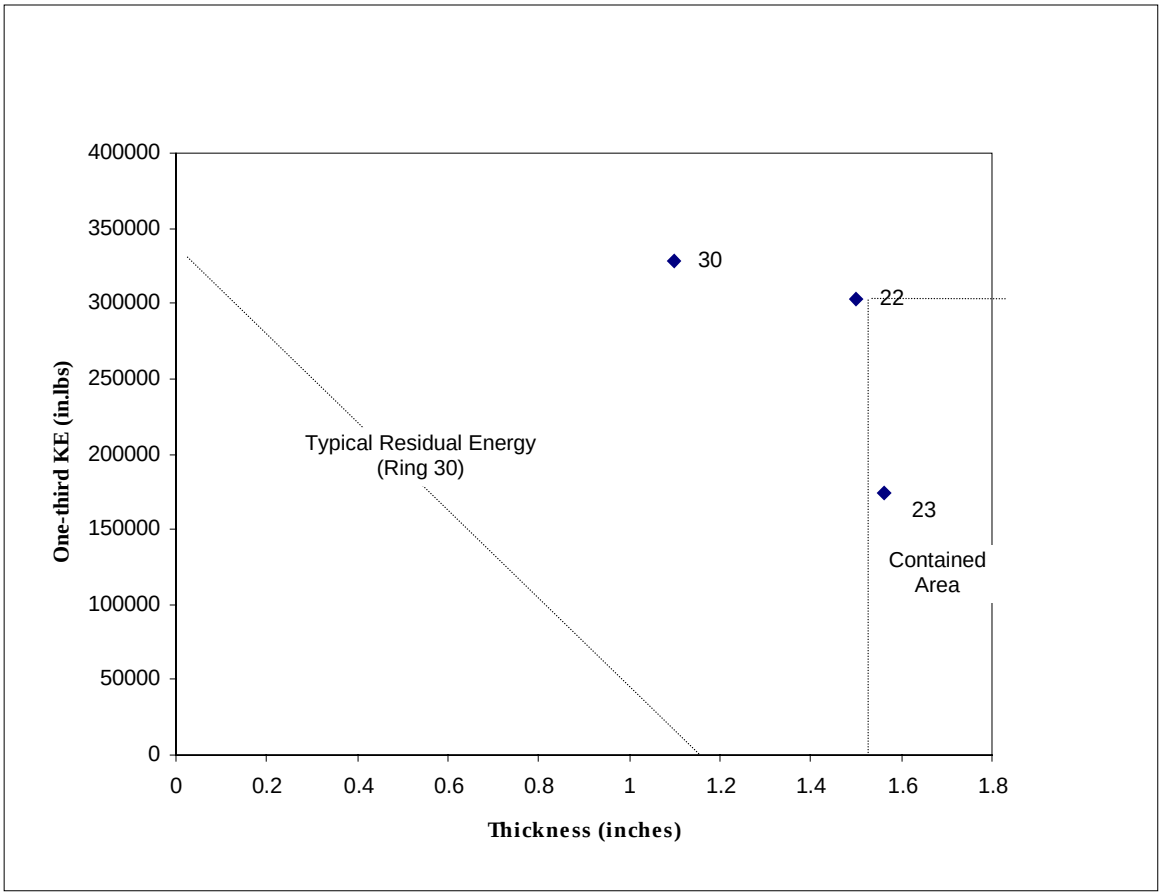

Group	Ring No.	Materials	Weight (lbs)	Normal-ized Weight (lbs)	Radial Thick-ness (in)	Axial Length (in)	No. of High-Speed Photos	Failed Speed (rpm)	Contained (C) or Not Contained (NC)	Test Temperature (°F)
4	22	Kevlar 29	18.00	18.00	1.50	9.00	37	19760	C	ambient
	23	Kevlar 29	24.00	21.60	1.56	10.00	0	15000	C	ambient
	30	Kevlar 29	17.00	13.91	1.10	11.00	38	20588	NC	ambient

FIGURE 27. GROUP 4—DRY KEVLAR 29

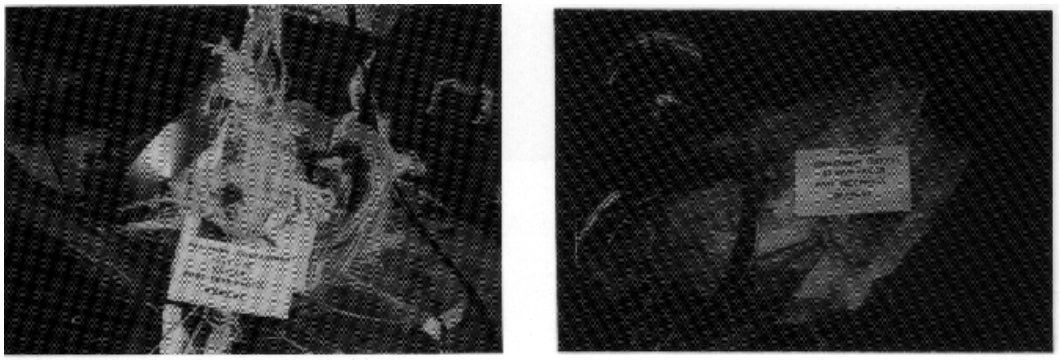

(1) RING 29

(2) RING 32

(3) RING 33

(4) RING 34

FIGURE 28. POSTTEST PICTURES OF RINGS 29, 32, 33, AND 34

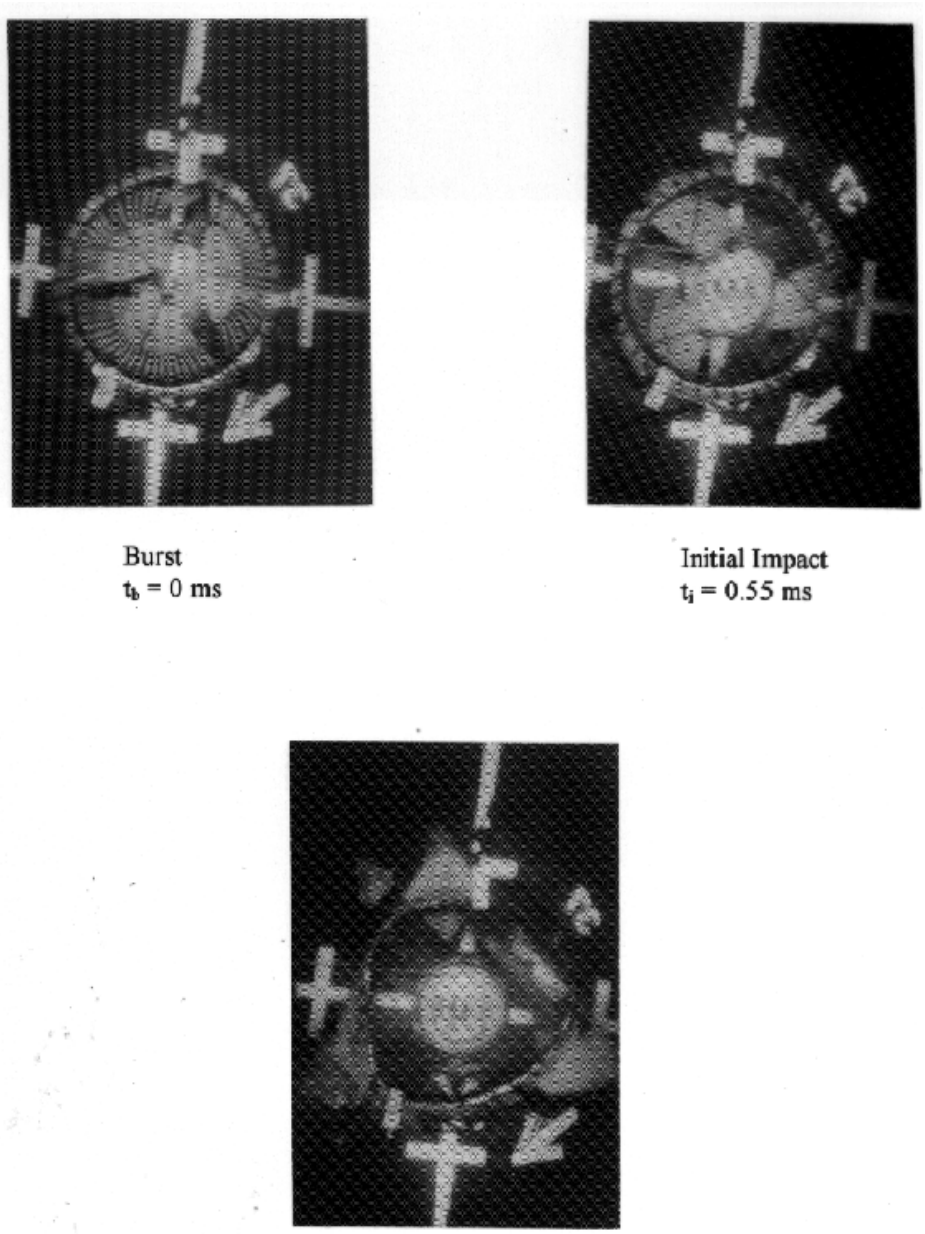

FIGURE 29. FAILURE EVENT OF RING 32

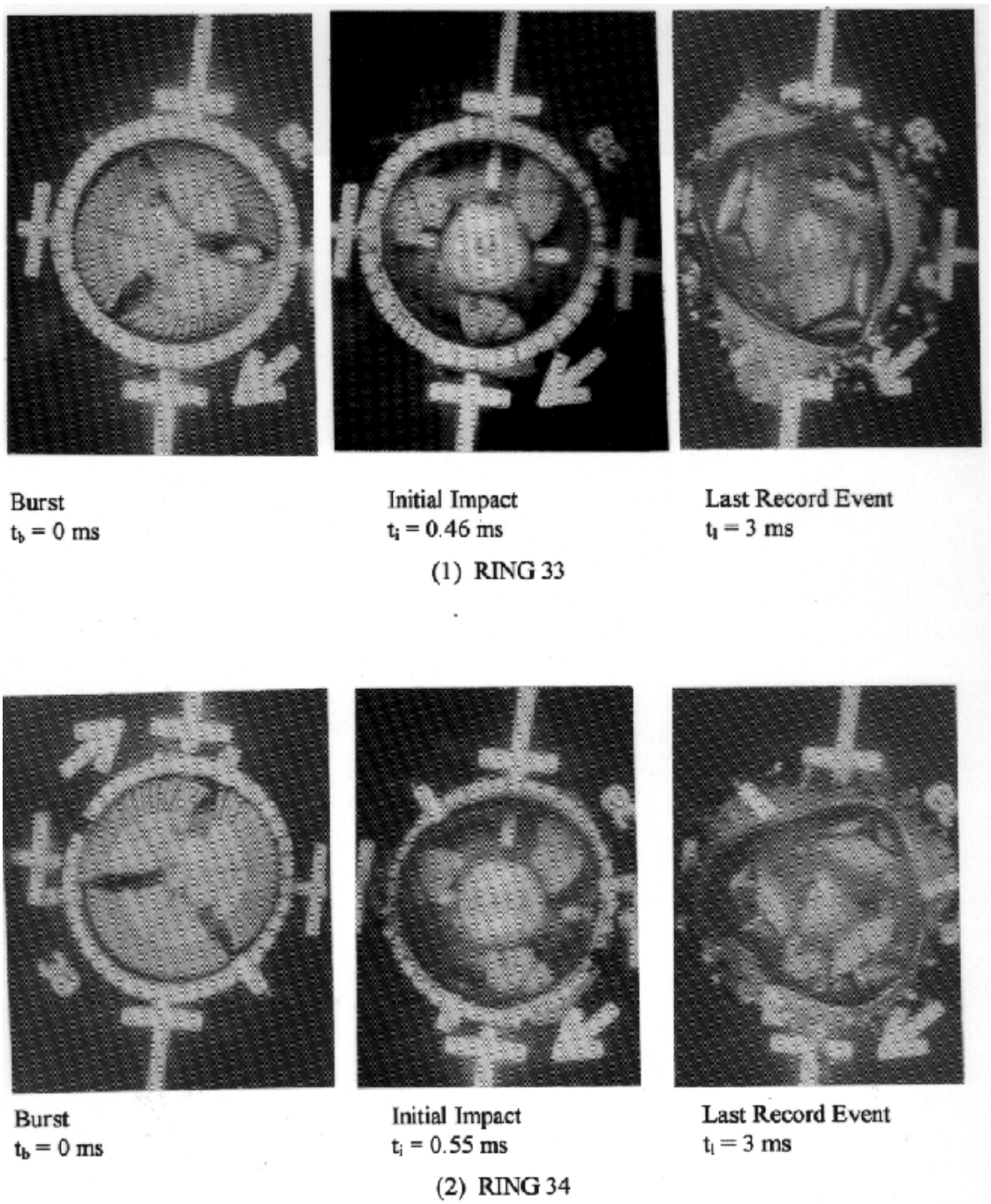

FIGURE 30. FAILURE EVENT OF RINGS 33 AND 34

Figure 31 shows the uncontained area. The uncontained fragment of ring 32 had the residual energy of 2,981 in-lbs. The uncontained fragment left ring 32 at the speed of approximately 800 inches per second or 44 miles per hour.

Group 6 had four Kevlar systems impregnated with phenolic resin (rings 1, 11, 16, and 25). Only ring 1 contained all rotor fragments. Normalized weight and thickness of ring 1 were 28.83 lbs and 1.62 inches. KE_w and KE_t of ring 1 were 34 kips/lb and 598 kips/in. These were the threshold values for this group. Three disc fragments penetrated and escaped ring 11. Two penetrated and escaped ring 16. One penetrated and escaped ring 25. Figure 32 shows the pictures of rings 1, 11, and 16. Figure 33 shows the failure event of rings 1 and 11. Figure 34 show the failure event of rings 16 and 25.

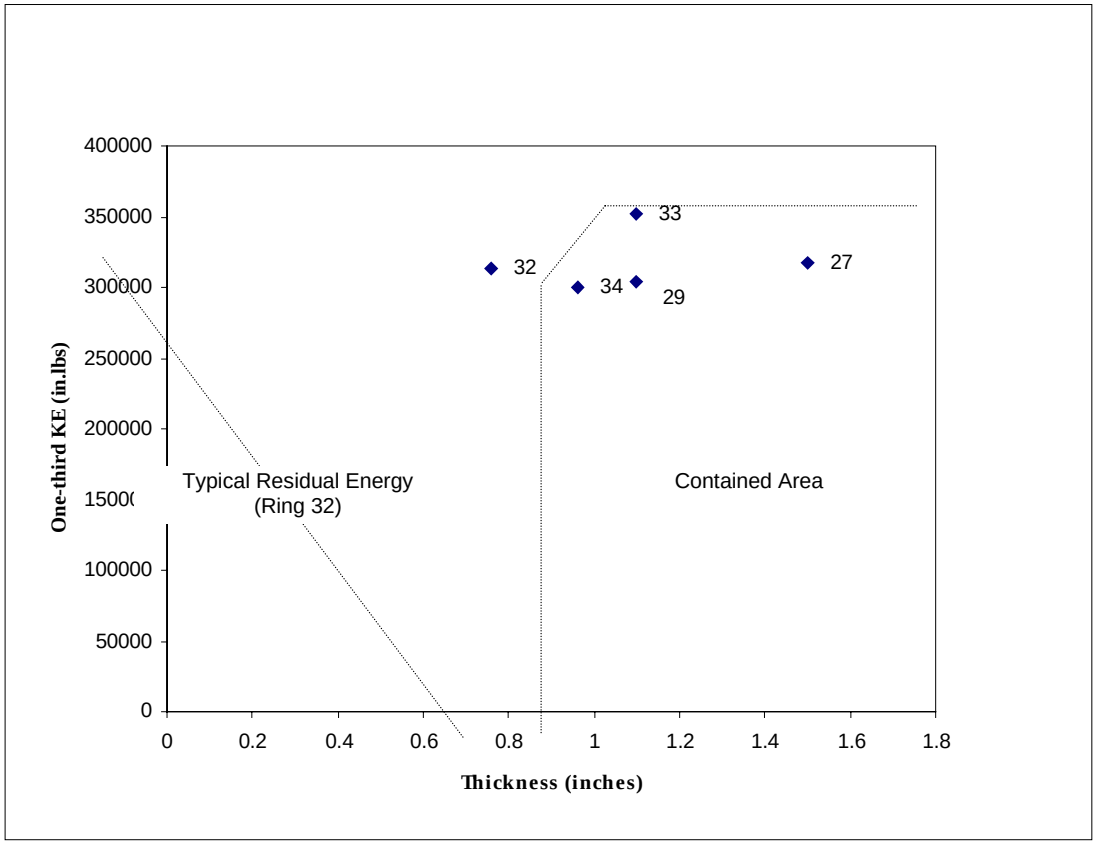

Group	Ring No.	Materials	Weight (lbs)	Normal-ized Weight (lbs)	Radial Thick-ness (in)	Axial Length (in)	No. of High-Speed Photos	Failed Speed (rpm)	Contained (C) or Not Contained (NC)	Test Temp-erature (°F)
5	27	Kevlar 29 - Al liner	24.75	24.08	1.5/.063	9.25	0	20240	C	ambient
	29	Kevlar 29 - Al liner	20.25	18.26	1.1/.063	9.98	0	19800	C	ambient
	32	Kevlar 29 - Al liner	12.00	10.65	0.76	10.14	38	20140	NC	ambient
	33	Kevlar 29 - Al liner	21.50	18.61	1.1/.063	10.40	39	21300	C	ambient
	34	Kevlar 29 - Al liner	18.50	16.00	0.96/0063	10.40	38	19675	C	ambient

FIGURE 31. GROUP 5—DRY KEVLAR 29-ALUMINUM

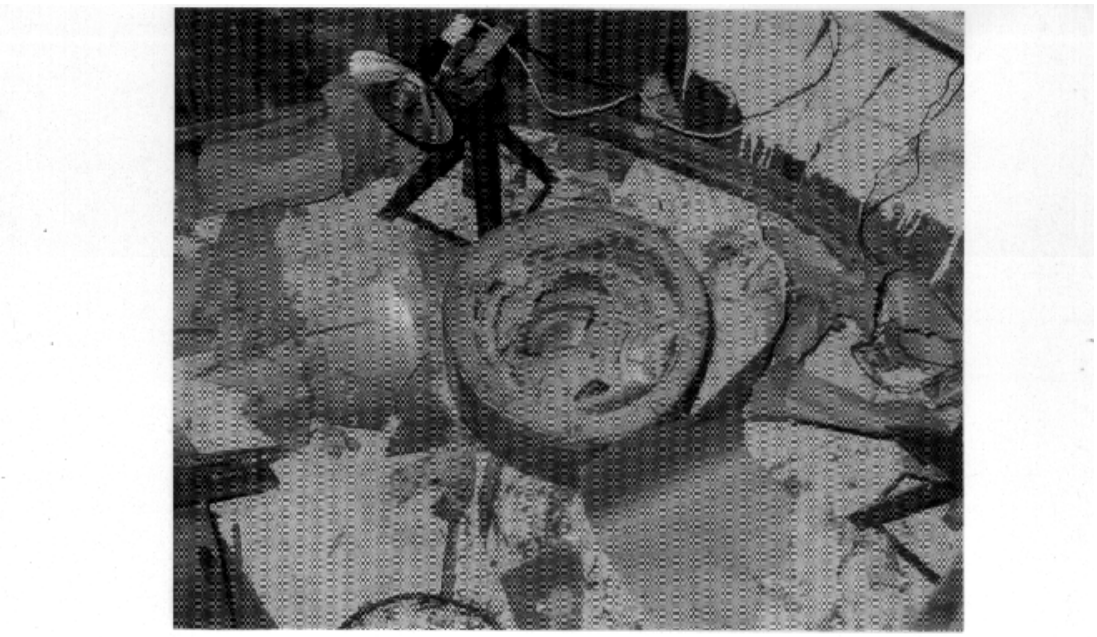

(1) RING 1

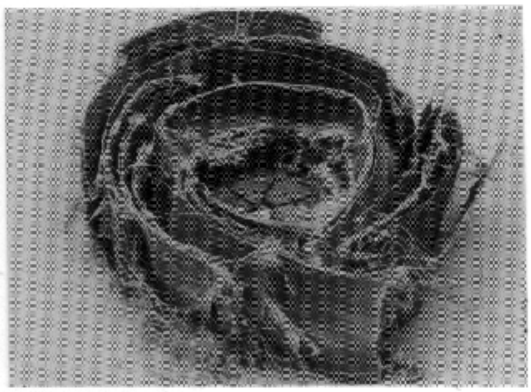

(2) RING 11

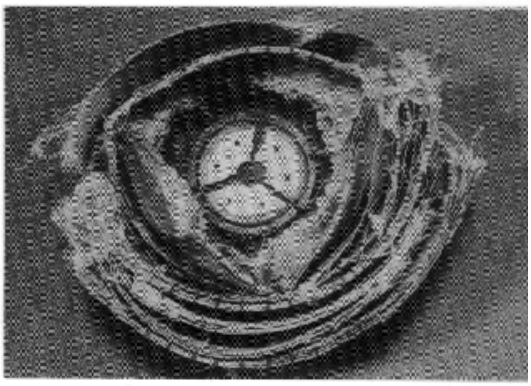

(3) RING 16

FIGURE 32. POSTTEST PICTURES OF RINGS 1, 11, AND 16

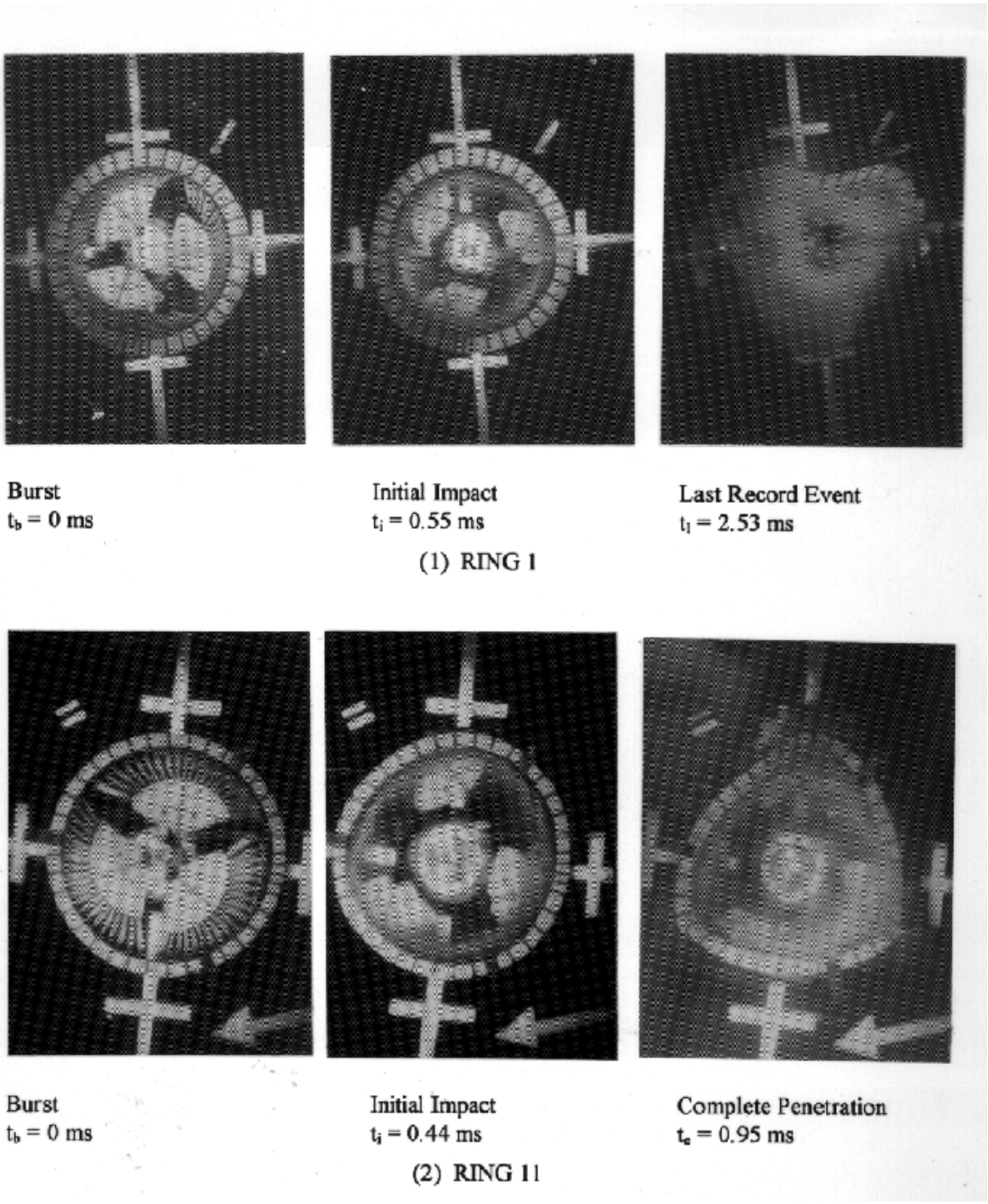

FIGURE 33. FAILURE EVENT OF RINGS 1 AND 11

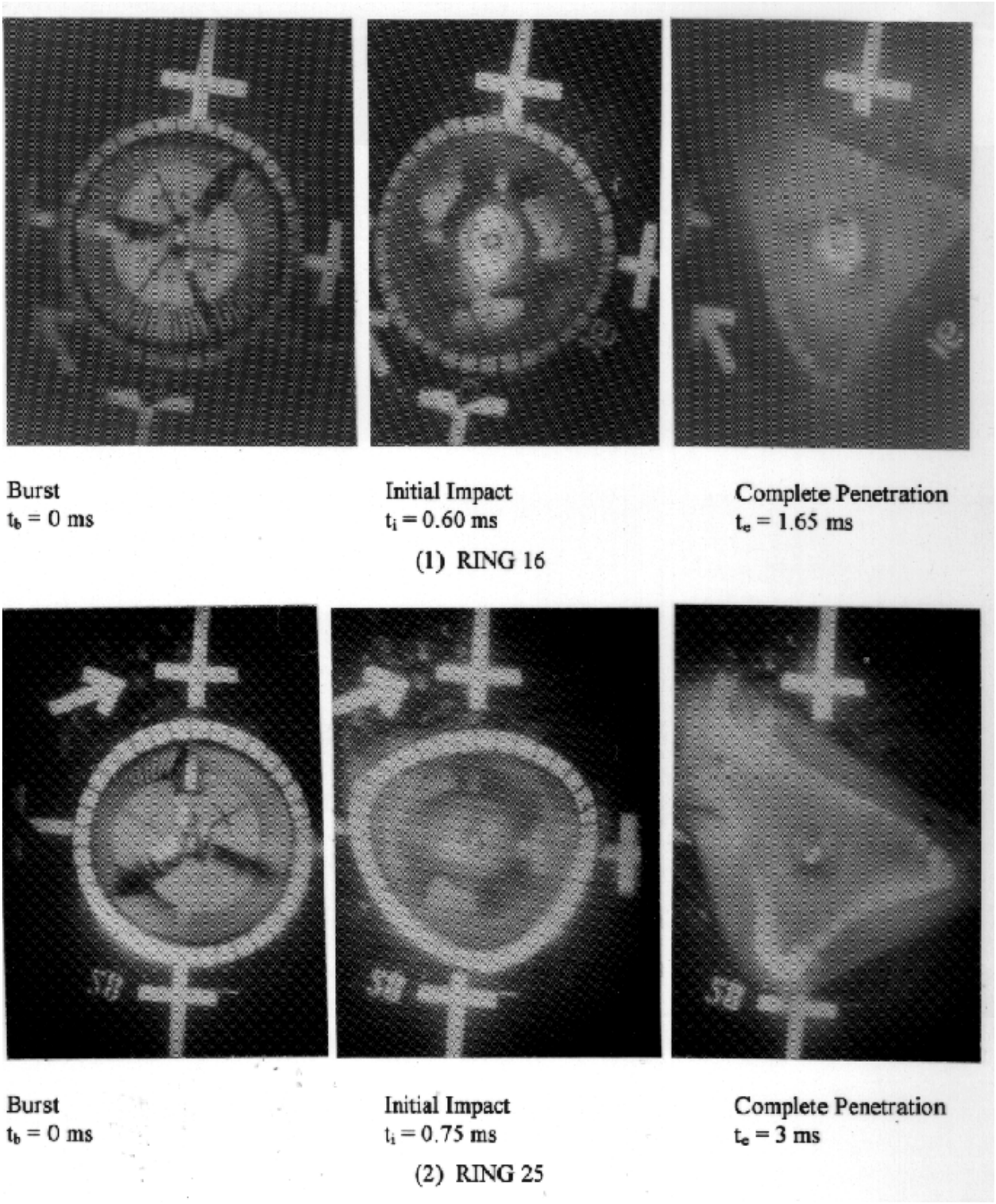

FIGURE 34. FAILURE EVENT OF RINGS 16 AND 25

Figure 35 shows that the uncontained fragment of ring 11 had the residual energy of 15.5 kips. The fragment was leaving ring 11 at the speed of approximately 1,824 inches per second or 104 miles per hour.

Group 7 had three steel and fiberglass composite systems (rings 6, 13, and 21). Fiberglass was also impregnated with phenolic resin. Rings 6 and 13 contained all rotor fragments. Steel layer thicknesses of rings 6 and 13 were 0.31 and 0.18 inch respectively. Normalized weight and thickness of ring 6 were 58.82 lbs and 1.00 inch and ring 13 were 35.00 lbs and 0.63 inch. KE_w and KE_t of ring 6 were 18 kips/lb and 1,065 kips/in and ring 13 were 30 kips/lb and 1,698 kips/in. System 13 represented the threshold configuration for this group. One disc fragment penetrated and escaped ring 21. Figure 36 shows the posttest event of rings 6, 13, and 21. Figure 37 shows the failure event of ring 13 and 21.

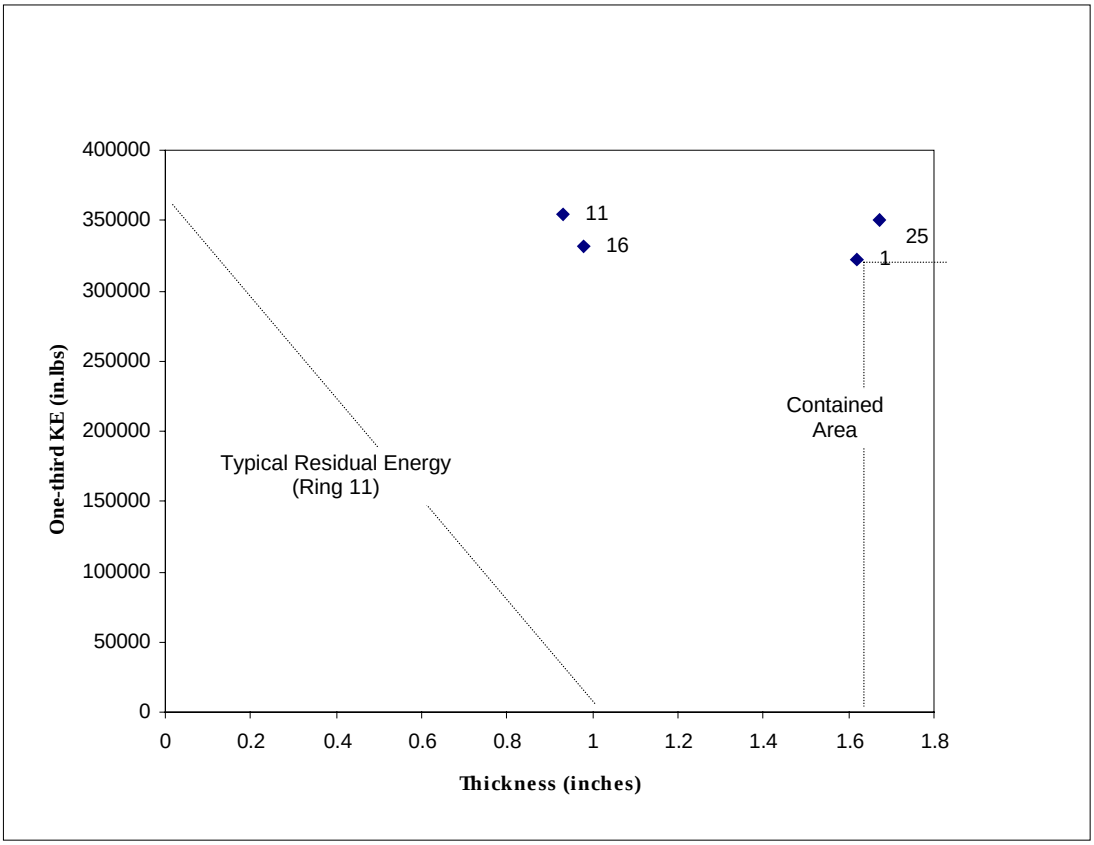

Group	Ring No.	Materials	Weight (lbs)	Normal-ized Weight (lbs)	Radial Thick-ness (in)	Axial Length (in)	No. of High-Speed Photos	Failed Speed (rpm)	Contained (C) or Not Contained (NC)	Test Temp-erature (°F)
6	1	Kevlar 29 - phenolic	32.00	28.83	1.62	9.99	38	20400	C	ambient
	11	Kevlar 29 - phenolic	19.25	19.25	0.93	9.00	41	21400	NC	ambient
	16	Kevlar 29 - phenolic	20.00	20.00	0.98	9.00	40	20665	NC	ambient
	25	Kevlar 29 - phenolic	22.50	22.50	1.67	9.00	4	21260	NC	ambient

FIGURE 35. GROUP 6—KEVLAR 29-PHENOLIC

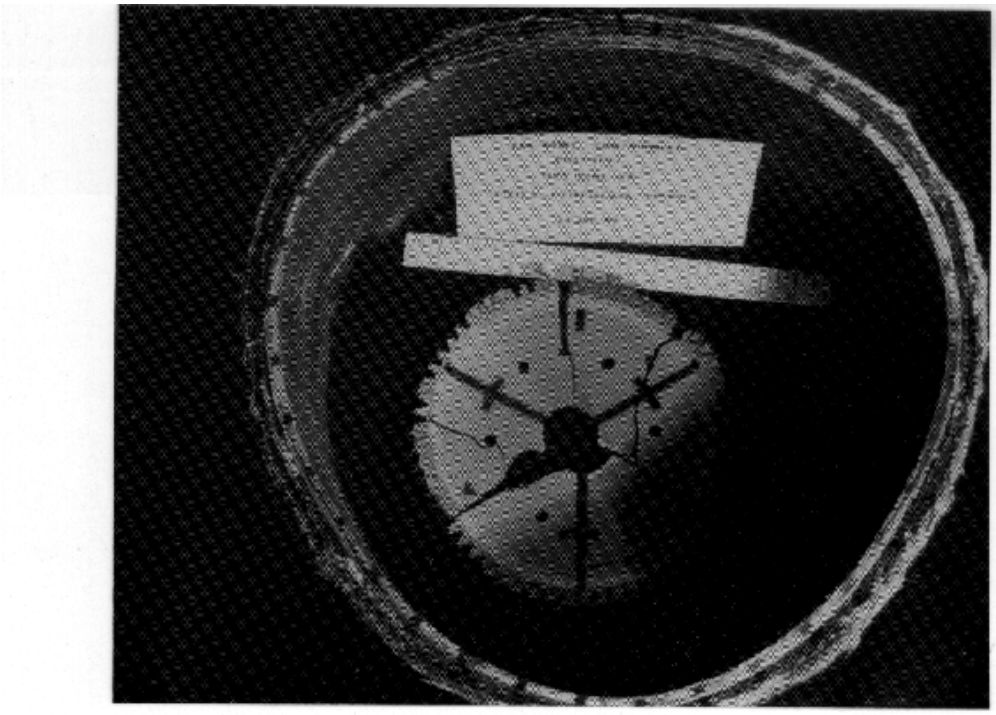

(1) RING 6

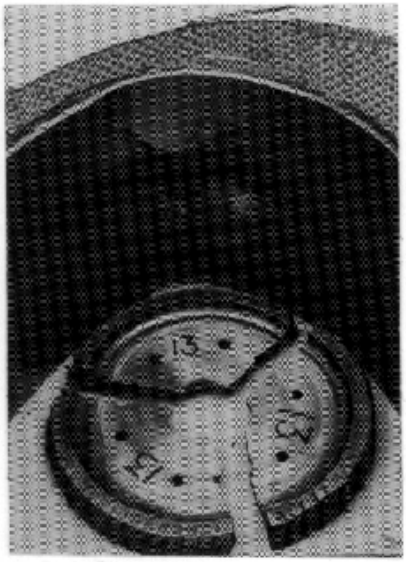

(2) RING 13

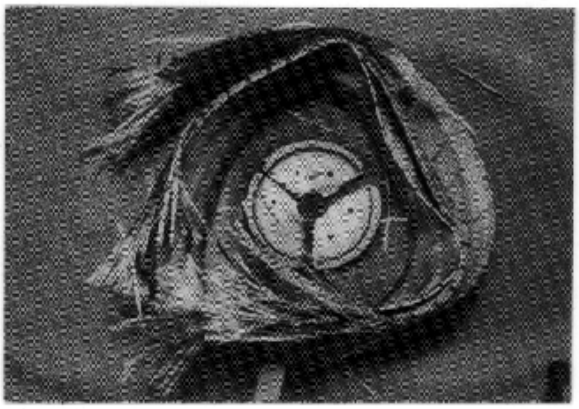

(3) RING 21

FIGURE 36. POSTTEST PICTURES OF RINGS 6, 13, AND 21

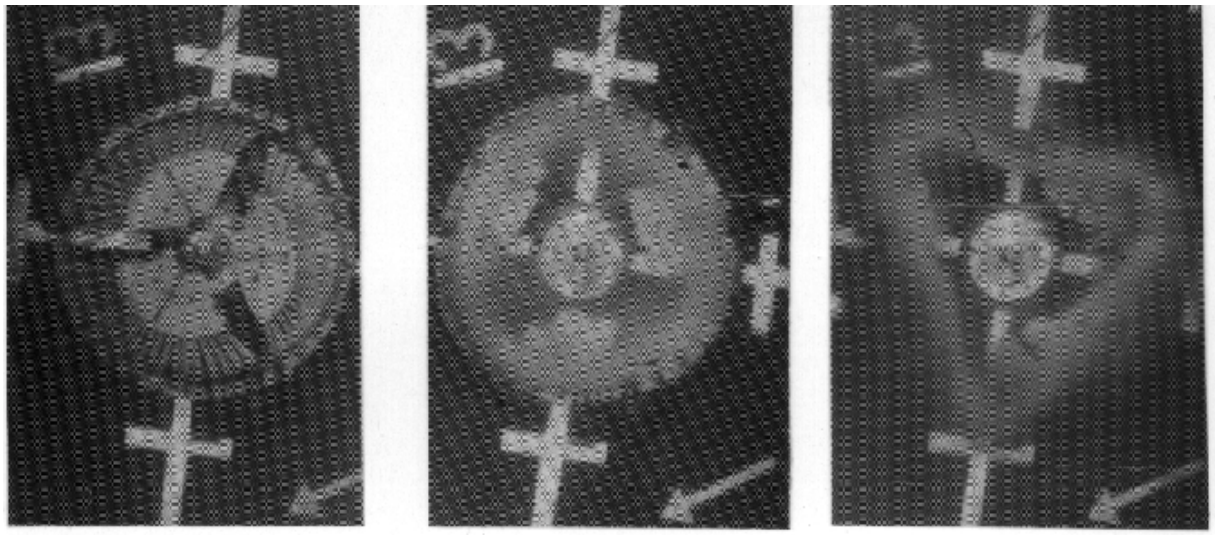

Burst
$t_b = 0$ ms

Initial Impact
$t_i = 0.50$ ms

Last Record Event
$t_l = 3$ ms

(1) RING 13

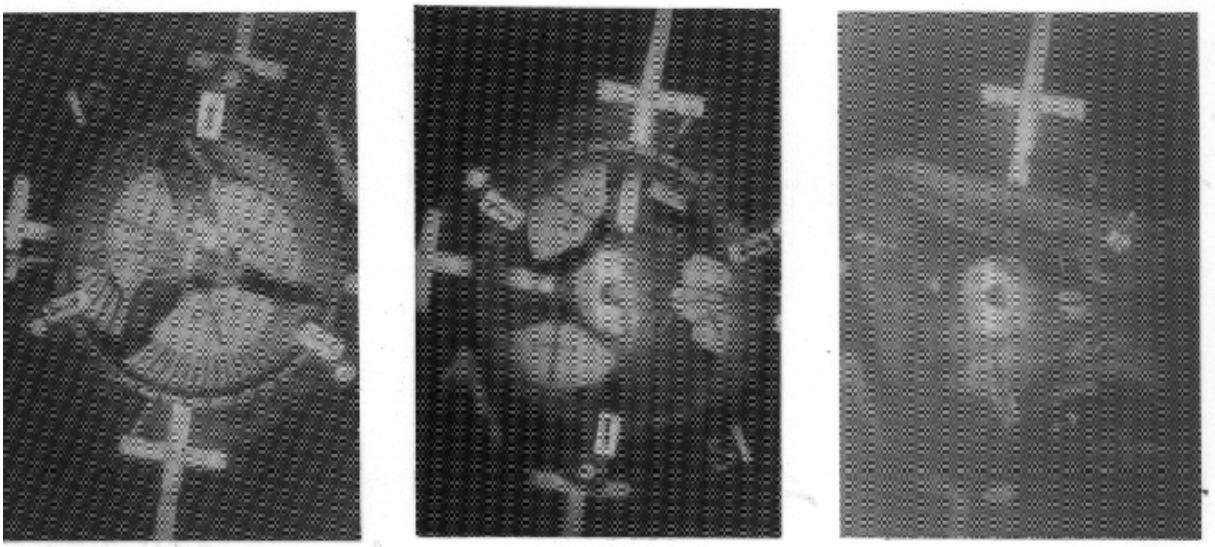

Burst
$t_b = 0$ ms

Initial Impact
$t_i = 0.57$ ms

Complete Penetration
$t_e = 3$ ms

(2) RING 21

FIGURE 37. FAILURE EVENT OF RINGS 13 AND 21

Figure 38 shows the uncontained fragment leaving ring 21 with the residual energy of 284 in-lbs at the speed of 247 inches per second or 14 miles per hour.

All systems (rings 7, 14, and 19) in group 8 contained all rotor fragments. Steel layer thickness of rings 7, 14, and 19 were 0.31, 0.19, and 0.12 inch respectively. Normalized weight and thickness of ring 7 were 63.90 lbs and 1.20 inches, ring 14 were 39.50 lbs and 0.71 inch, and ring 19 were 29.00 lbs and 0.57 inch respectively. KE_w and KE_t of ring 7 were 16 kips/lb and 831 kips/in, ring 14 were 21 kips/lb and 1,187 kips/in, and ring 19 were 31 kips/lb and 1.591 kips/in respectively. No system represented the threshold configuration. System 7 was, however, selected for ranking due to its higher energy absorbed per unit weight. Minimum damage was done on these systems. Figure 39 shows the posttest pictures of rings 7, 14, and 19. Figure 40 shows the failure event of ring 7 and 19. Figure 41 shows the contained area without the threshold value.

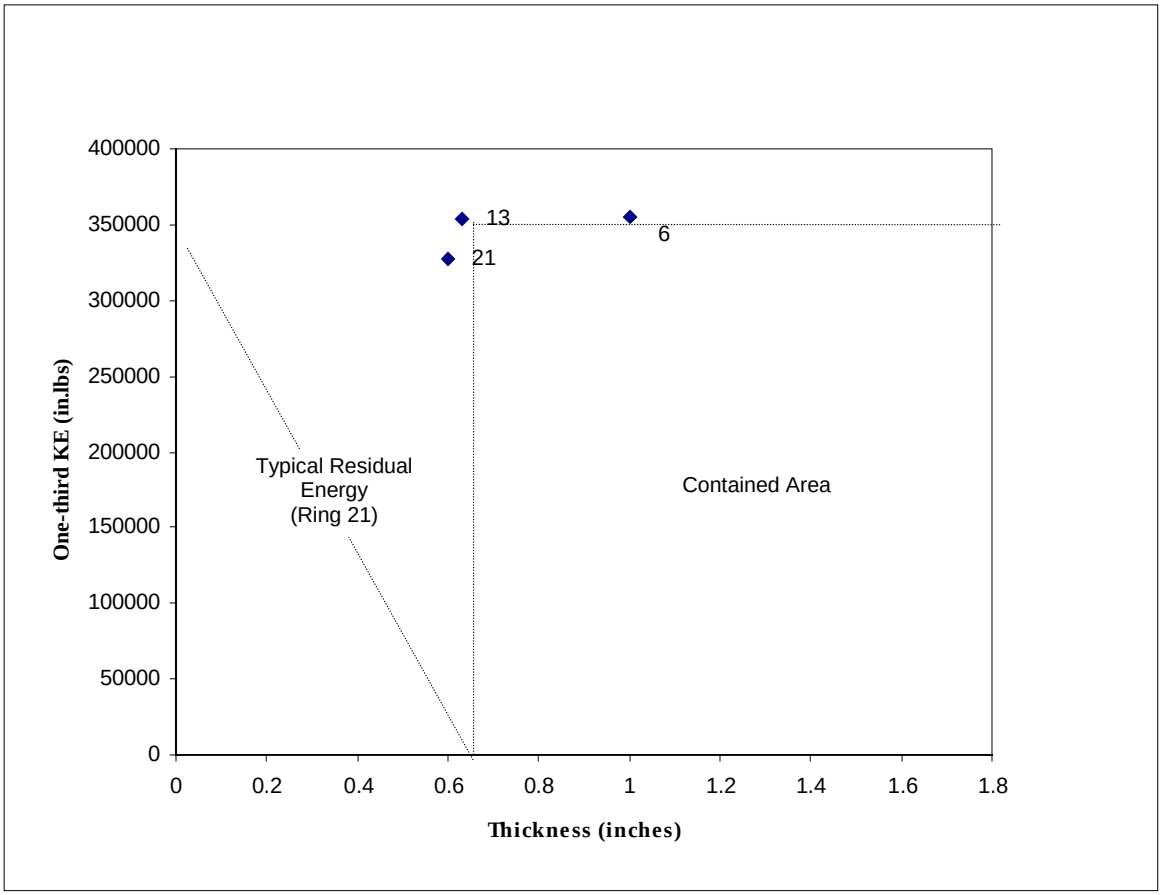

Group	Ring No.	Materials	Weight (lbs)	Normal-ized Weight (lbs)	Radial Thick-ness (in)	Axial Length (in)	No. of High-Speed Photos	Failed Speed (rpm)	Contained (C) or Not Contained (NC)	Test Temp-erature (°F)
7	6	Steel-fiberglass-phenolic	60.00	58.82	1.00 0.31/0.69	9.18	1	21400	C	ambient
	13	Steel-fiberglass-phenolic	35.00	35.00	0.63 0.18/0.45	9.00	42	21360	C	ambient
	21	Steel-fiberglass-phenolic	26.00	26.00	0.60 0.13/0.49	9.00	37	20570	NC	ambient

FIGURE 38. GROUP 7—STEEL-FIBERGLASS-PHENOLIC

(1) RING 7

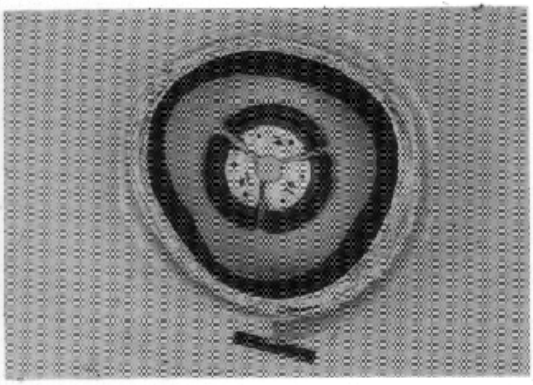

(2) RING 14

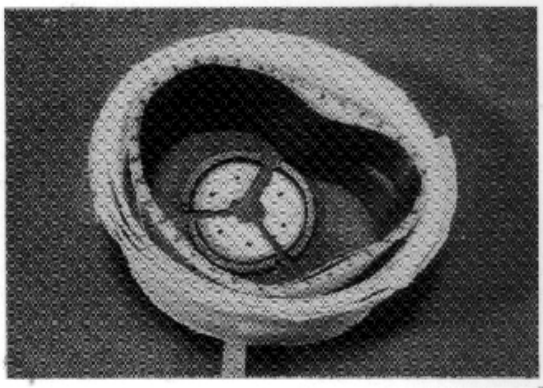

(3) RING 19

FIGURE 39. POSTTEST PICTURES OF RINGS 7, 14, AND 19

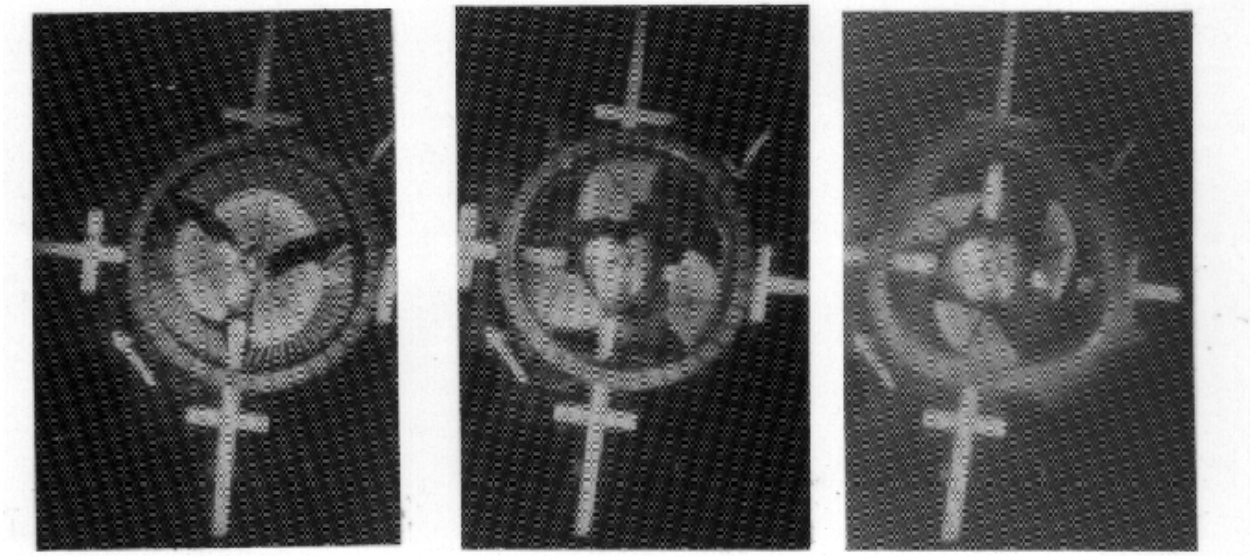

Burst
$t_b = 0$ ms

Initial Impact
$t_i = 0.75$ ms

Last Record Event
$t_l = 3$ ms

(1) RING 7

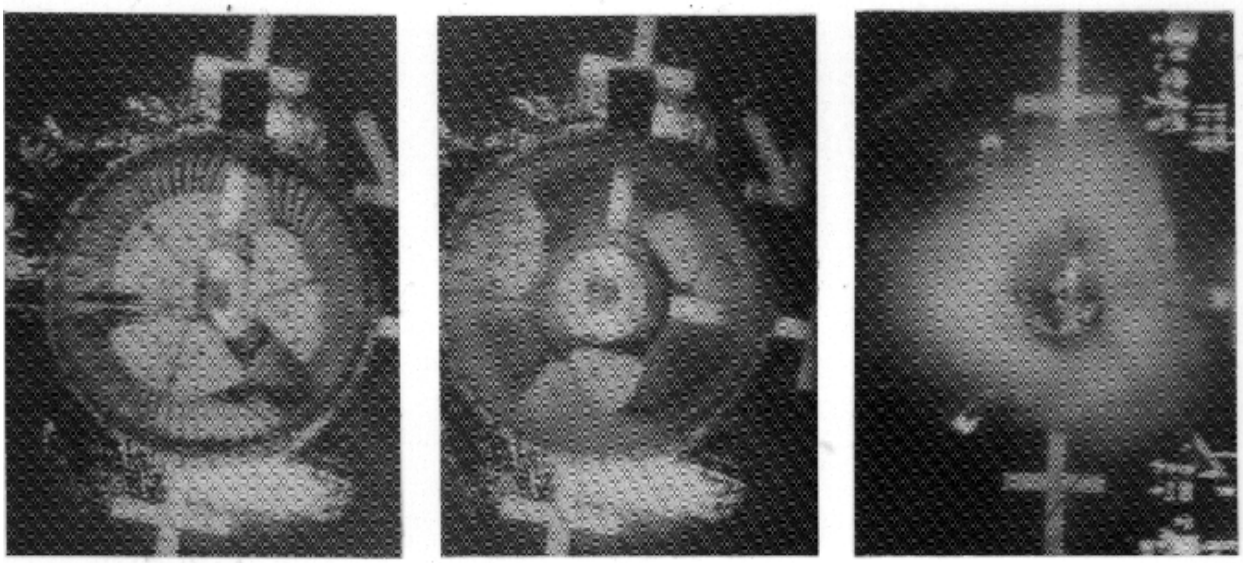

Burst
$t_b = 0$ ms

Initial Impact
$t_i = 0.57$ ms

Last Record Event
$t_l = 3$ ms

(2) RING 19

FIGURE 40. FAILURE EVENT OF RINGS 7 AND 19

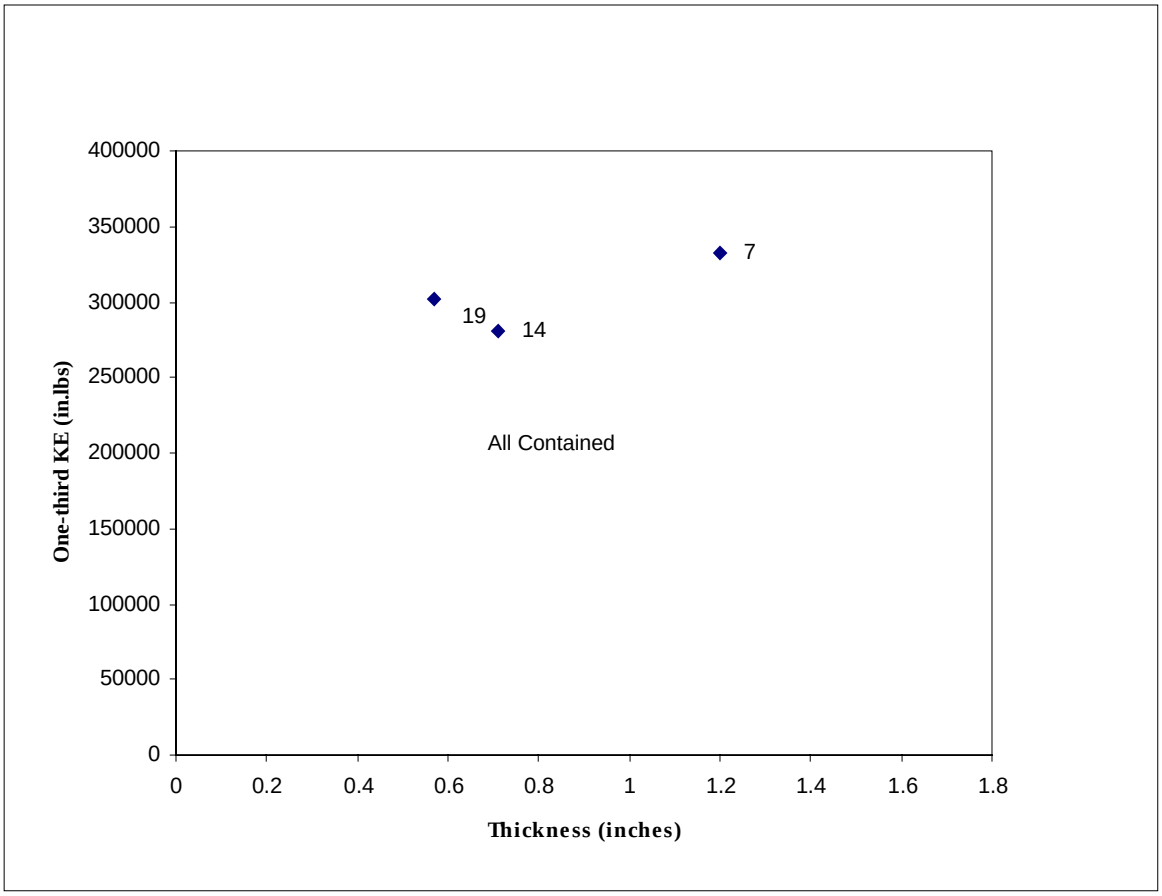

Group	Ring No.	Materials	Weight (lbs)	Normal-ized Weight (lbs)	Radial Thickness (in)	Axial Length (in)	No. of High-Speed Photos	Failed Speed (rpm)	Contained (C) or Not Contained (NC)	Test Temp-erature (°F)
8	7	Steel-fiberglass-polyester	65.75	63.90	1.20 0.31/0.89	9.26	28	20700	C	ambient
	14	Steel-fiberglass-polyester	39.50	39.50	0.71 0.19/0.52	9.00	0	19040	C	ambient
	19	Steel-fiberglass-polyester	29.00	29.00	0.59 0.12/0.47	9.00	37	19750	C	ambient

FIGURE 41. GROUP 8—STEEL-FIBERGLASS-POLYESTER

Group 9 had three titanium-Kevlar composite systems (rings 4, 12, and 15). Kevlar was also impregnated with phenolic resin. Rings 4 and 15 contained all fragments. Titanium layer thickness of rings 4 and 15 was 0.31 and 0.25 inch. Normalized weight and thickness of ring 4 were 37.13 lbs and 1.10 inches and ring 15 were 27.50 lbs and 0.73 inch respectively. KE_w and KE_t of ring 4 were 27 kips/lb and 906 kips/in and ring 15 were 36 kips/lb and 1,347 kips/in respectively. System 15 gave threshold values. One fragment penetrated the titanium layer and punched a hole in the Kevlar ring. System 4 was selected for ranking due to its higher energy absorbed per unit weight. Two disc fragments penetrated and escaped ring 15. Figure 42 shows the posttest pictures of ring 4, 12, and 15. Figures 43 and 44 show the failure event of rings 4, 12, and 15.

Figure 45 shows the typical residual energy of the uncontained fragment of this group. The fragment was leaving ring 12 with the energy of 9.5 kips at the speed of approximately 1,432 inches per seconds or an equivalence of 81 miles per hour.

The last group, group 10, consisted of three titanium systems (rings 5, 8, and 18). Rings 5 and 18 contained all rotor fragments. Minimum damage was recorded on these rings. Normalized weight and thickness of ring 5 were 43.95 lbs and 0.62 inch and ring 18 were 35.00 lbs and 0.50 inch. KE_w and KE_t of ring 5 were 22 kips/lb and 1,584 kips/in and ring 18 were 31 kips/lb and 2,168 kips/in. System 18 gave threshold values for this group and provided highest energy absorbed per unit weight. One disc fragment penetrated and escaped ring 8. Figure 46 shows the posttest pictures of rings 5, 8, and 18. Figure 47 shows the failure event of ring 18.

Figure 48 shows the contained area of this group.

Figure 49 shows the containment ring weight versus penetrating duration for uncontained systems. For a given penetrating duration, dry Kevlar performed better than Kevlar-phenolic system based on its weight. There are not sufficient data on other uncontained systems to make a parametric comparison.

Similarly, figure 50 confirms the observation made in figure 49 that dry Kevlar also performed better than the Kevlar-phenolic system based on its thickness.

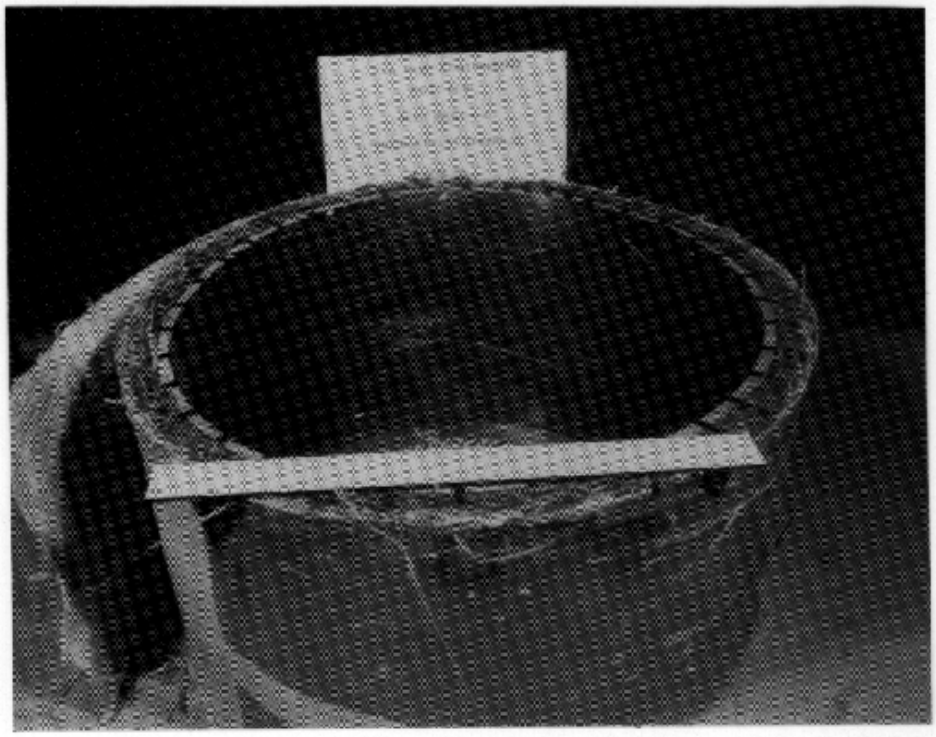

(1) RING 4

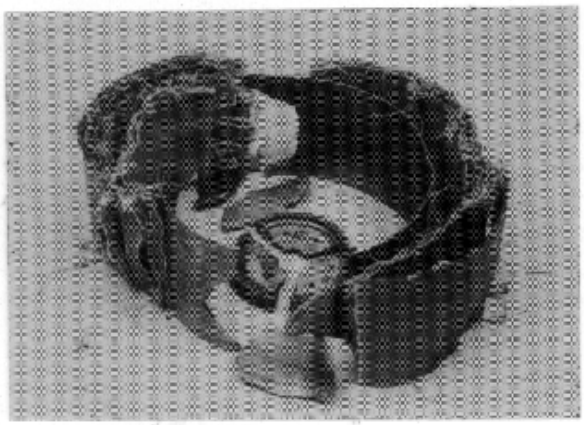

(2) RING 12

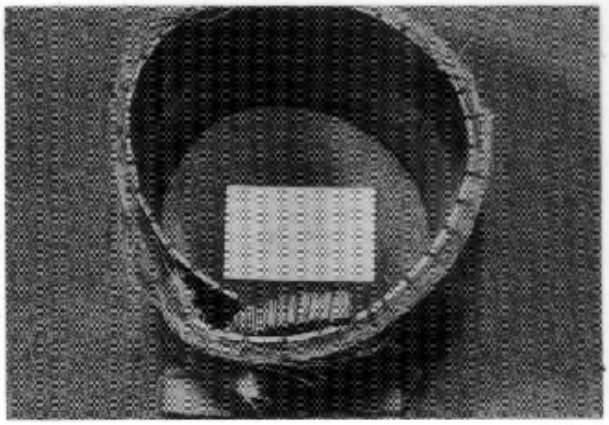

(3) RING 15

FIGURE 42. POSTTEST PICTURES OF RINGS 4, 12, AND 15

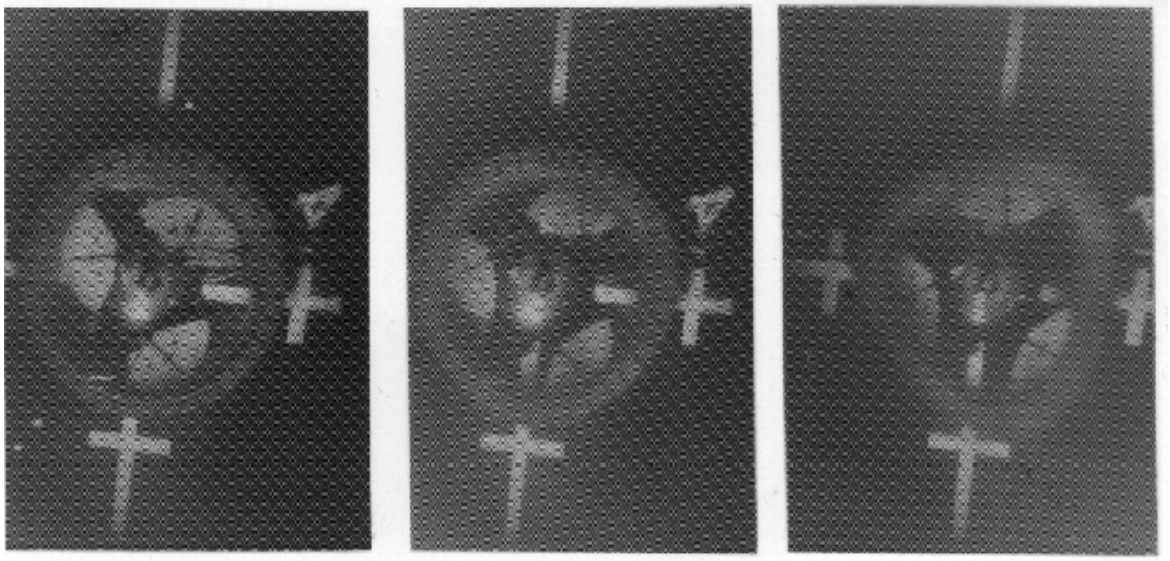

Burst
$t_b = 0$ ms

Initial Impact
$t_i = 0.36$ ms

Last Record Event
$t_l = 3$ ms

(1) RING 4

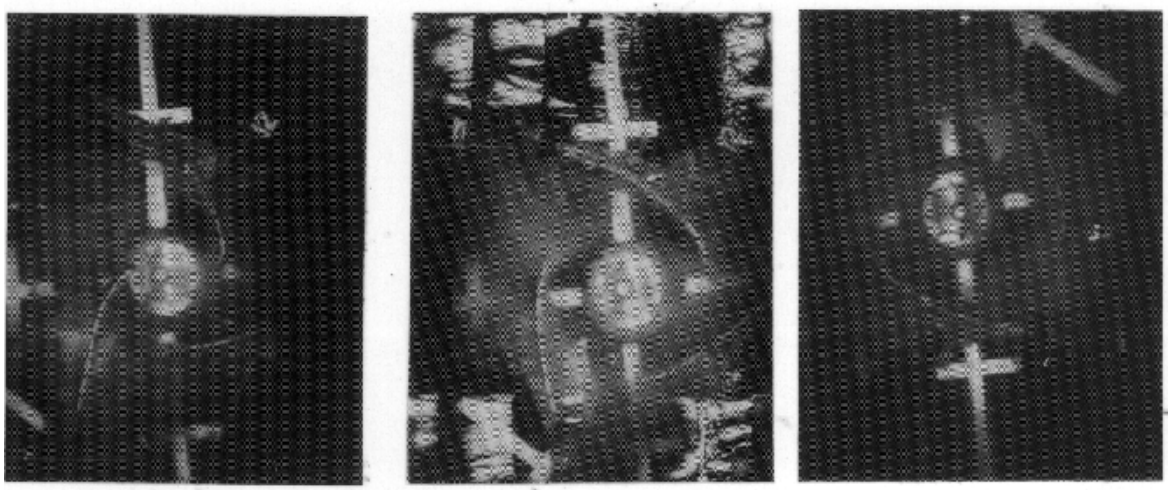

Burst
$t_b = 0$ ms

Initial Impact
$t_i = 0.59$ ms

Complete Penetration
$t_c = 1.46$ ms

(2) RING 12

FIGURE 43. FAILURE EVENT OF RINGS 4 AND 12

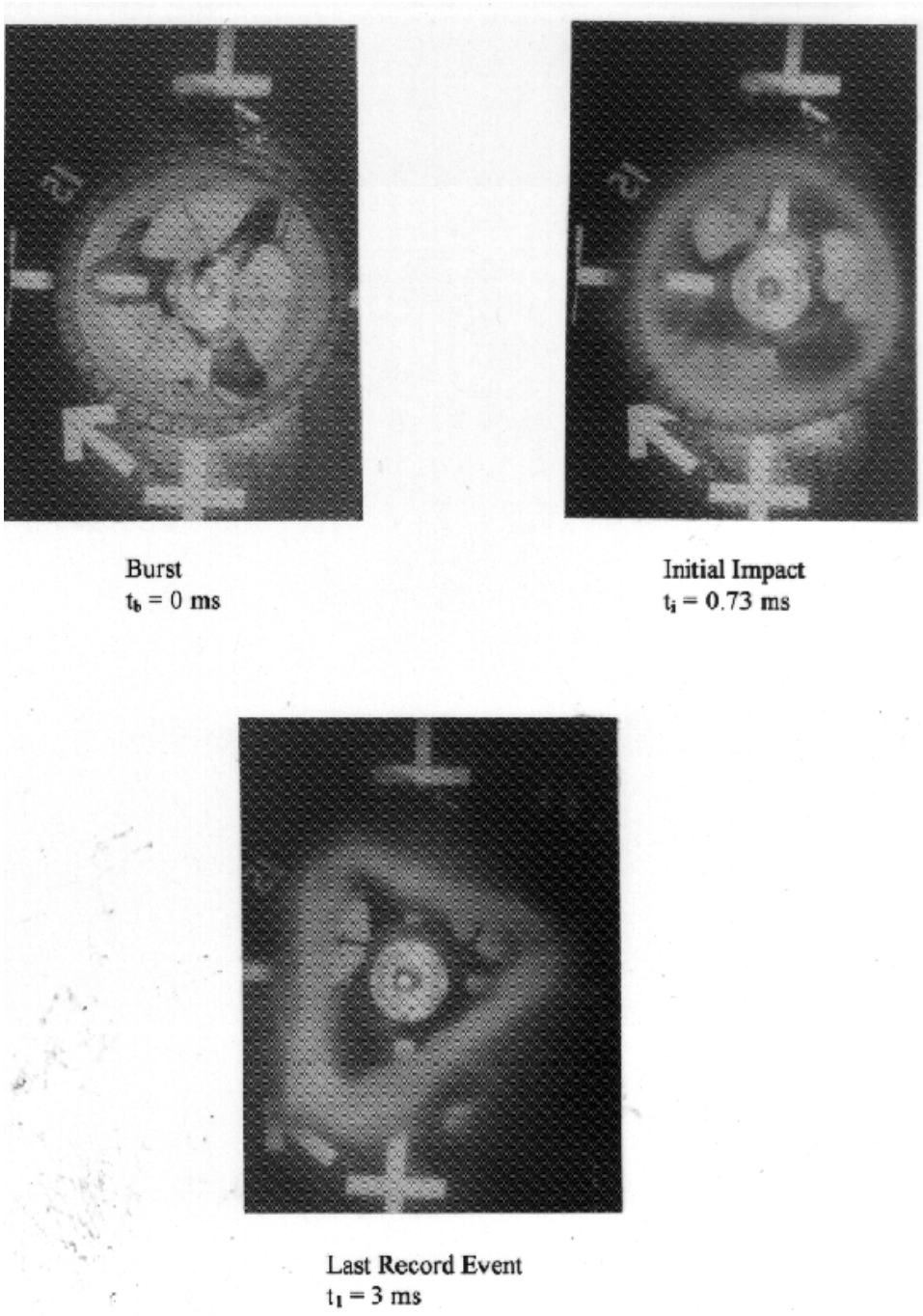

FIGURE 44. FAILURE EVENT OF RING 15

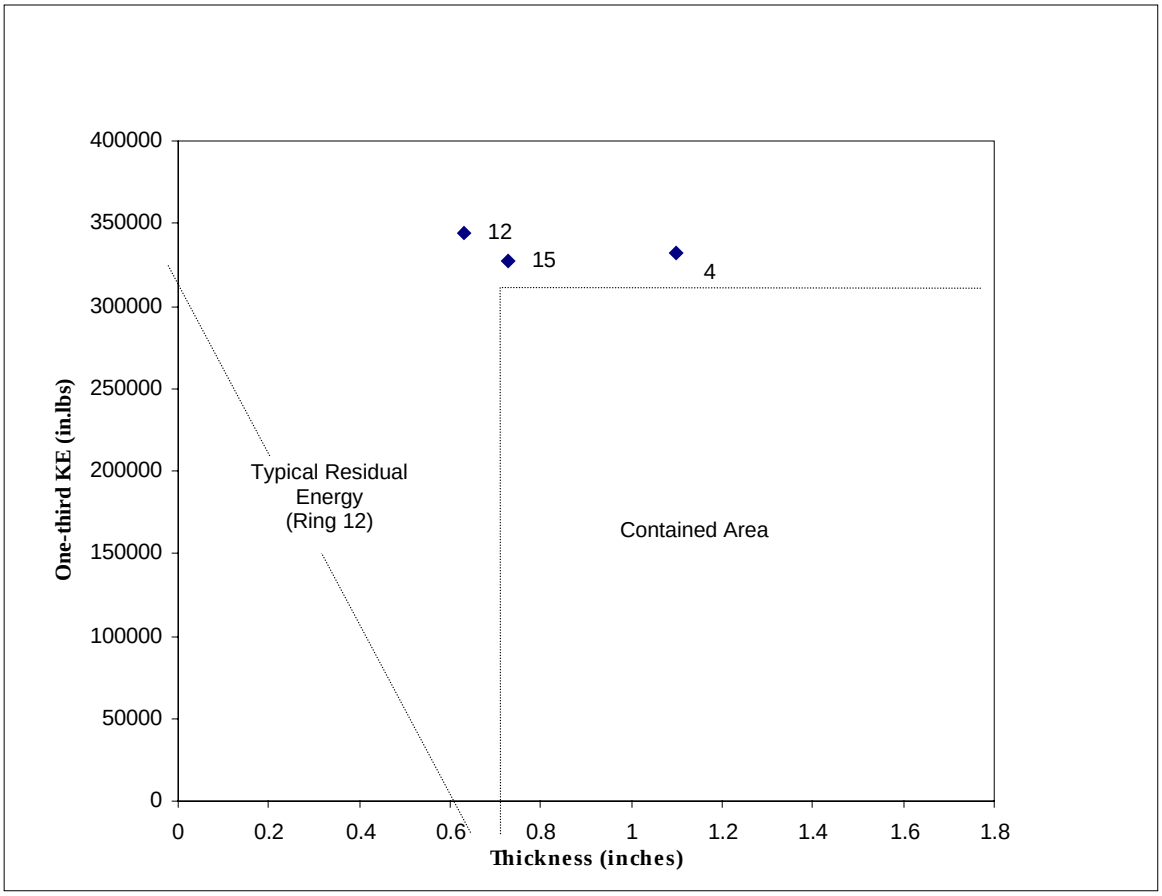

Group	Ring No.	Materials	Weight (lbs)	Normal-ized Weight (lbs)	Radial Thick-ness (in)	Axial Length (in)	No. of High-Speed Photos	Failed Speed (rpm)	Contained (C) or Not Contained (NC)	Test Temp-erature (°F)
9	4	Ti-kevlar-phenolic	37.25	37.13	1.10 0.31/0.79	9.03	42	20700	C	ambient
	12	Ti-kevlar-phenolic	22.50	22.38	0.63	9.05	41	21080	N	ambient
	15	Ti-kevlar-phenolic	27.50	27.50	0.73 0.25/0.48	9.00	37	20556	C	ambient

FIGURE 45. GROUP 9—TITANIUM-DRY KEVLAR-PHENOLIC

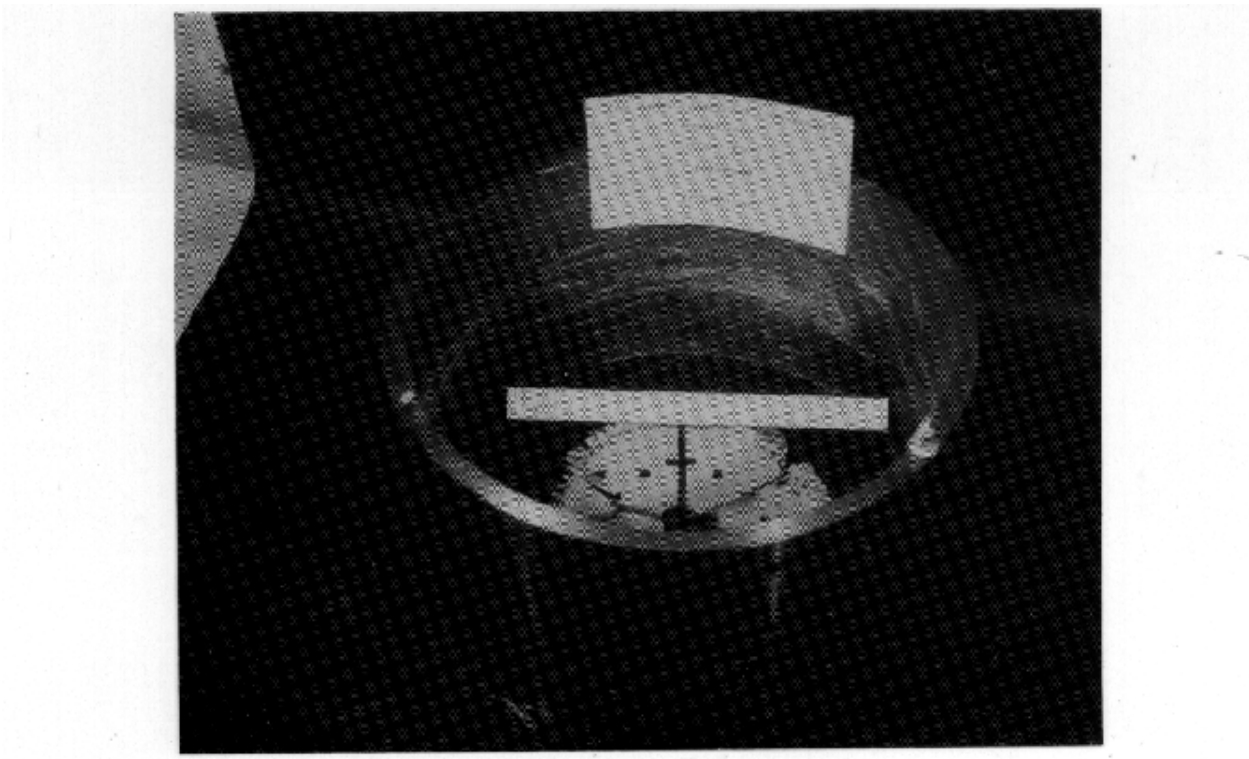

(1) RING 5

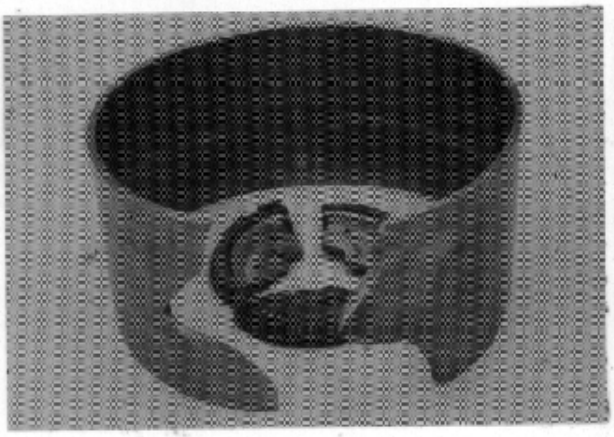

(2) RING 8

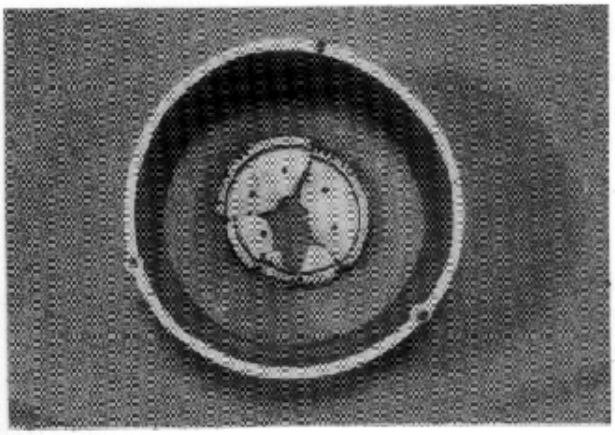

(3) RING 18

FIGURE 46. POSTTEST PICTURES OF RINGS 5, 8, AND 18

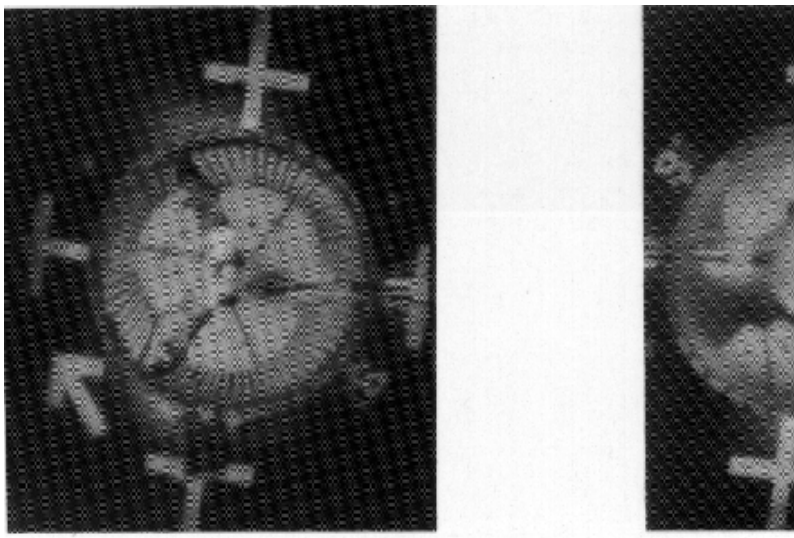

Burst
t_b = 0 ms

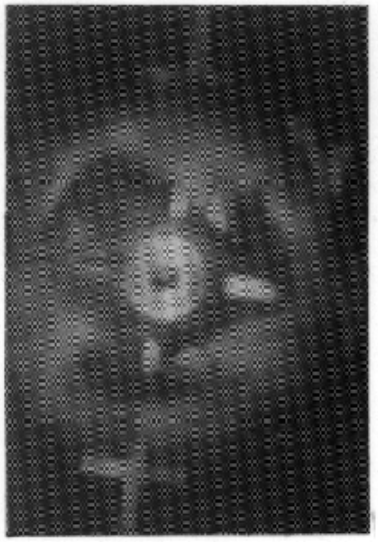

Last Record Event
t_l = 1 ms

FIGURE 47. FAILURE EVENT OF RING 18

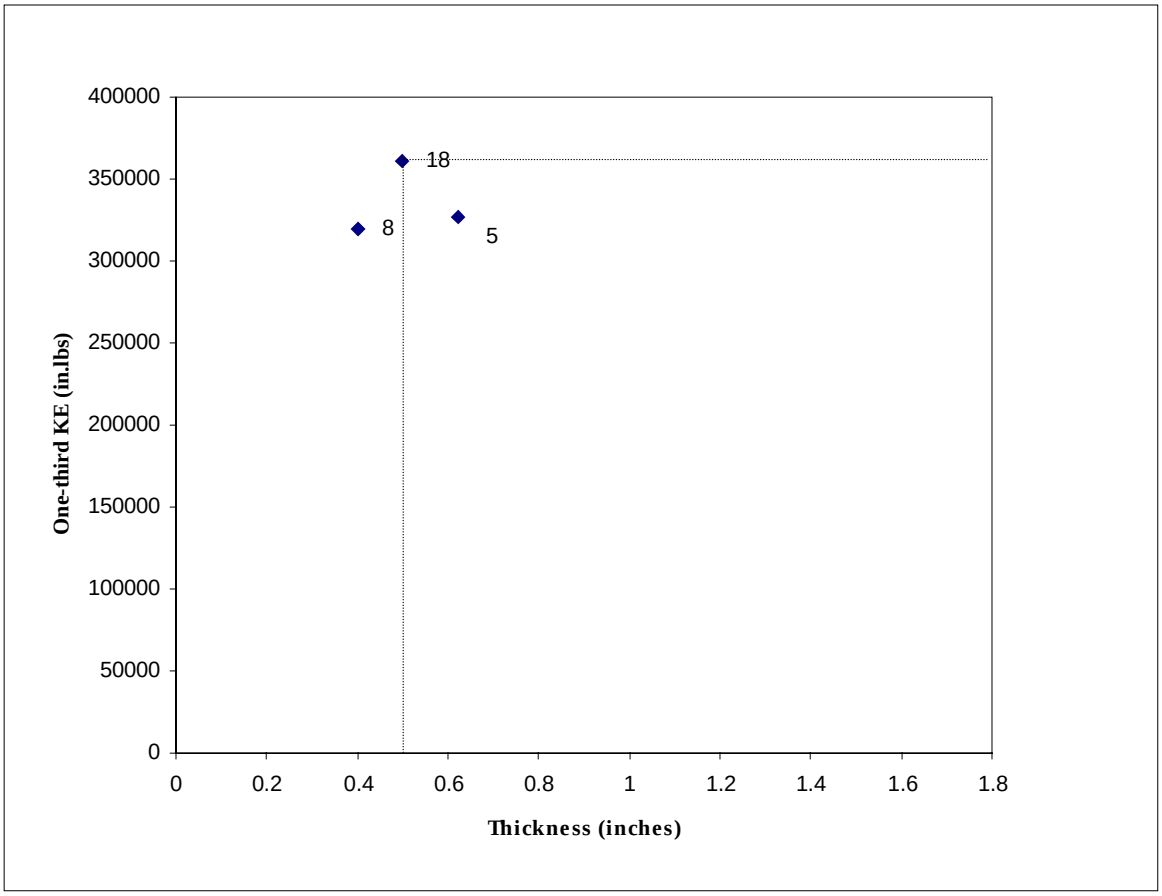

Group	Ring No.	Materials	Weight (lbs)	Normal-ized Weight (lbs)	Radial Thick-ness (in)	Axial Length (in)	No. of High-Speed Photos	Failed Speed (rpm)	Contained (C) or Not Contained (NC)	Test Temp-erature (°F)
	5	Titanium (6A14V)	44.00	43.95	0.62	9.01	1	20550	C	ambient
10	8	Titanium (6A14V)	27.25	26.37	0.40	9.30	1	20300	NC	ambient
	18	Titanium (6A14V)	35.00	35.00	0.50	9.00	37	21583	C	ambient

FIGURE 48. GROUP 10—TITANIUM

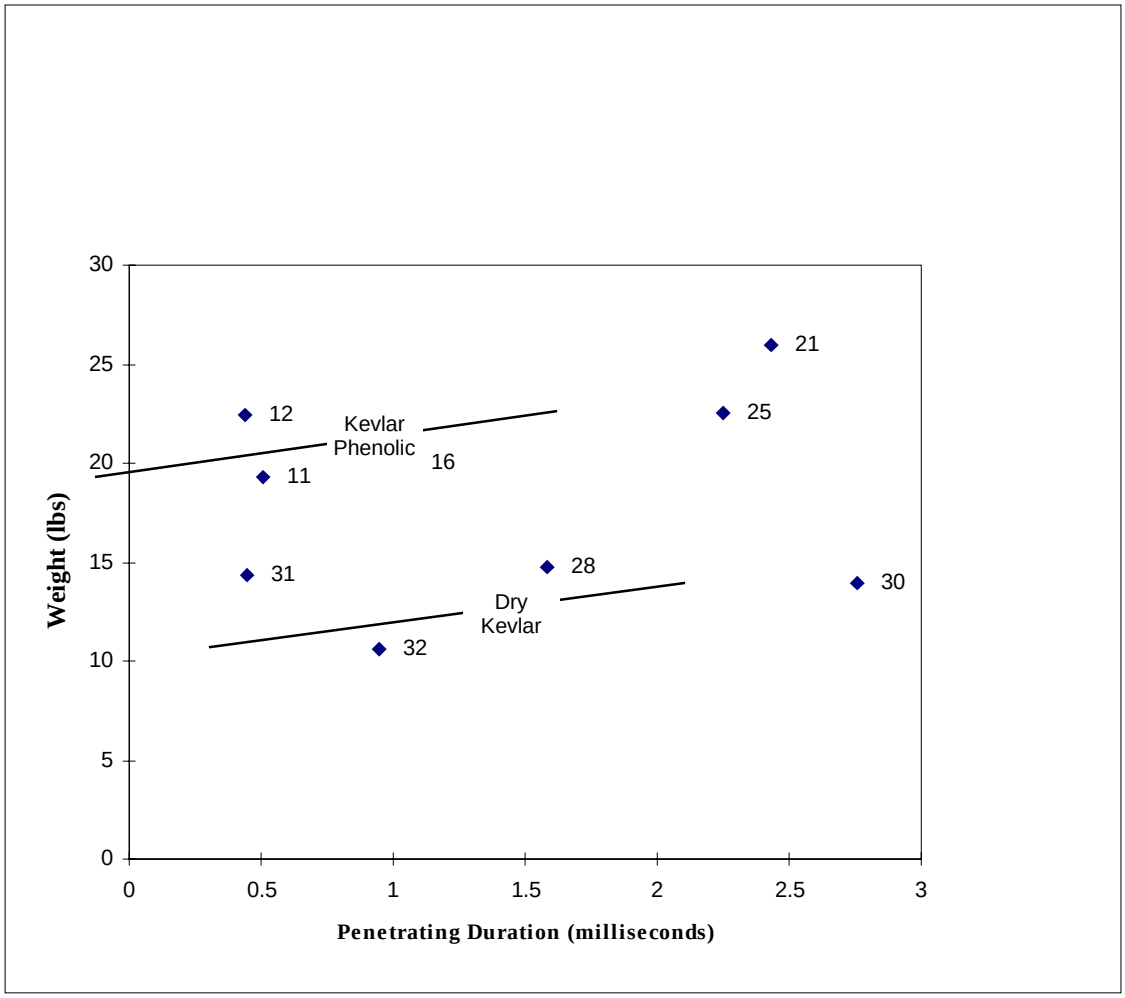

SYSTEMS

Ring 12: Titanium-Kevlar-Phenolic
Ring 21: Steel-Fiberglass-Polyester
Rings 11, 16, and 25: Kevlar-Phenolic
Ring 31: Fiberglass-Aluminum
Ring 28: Fiberglass Polyester
Rings 32 and 30: Kevlar-Aluminum

FIGURE 49. WEIGHT INCREASE VERSUS PENETRATING DURATION

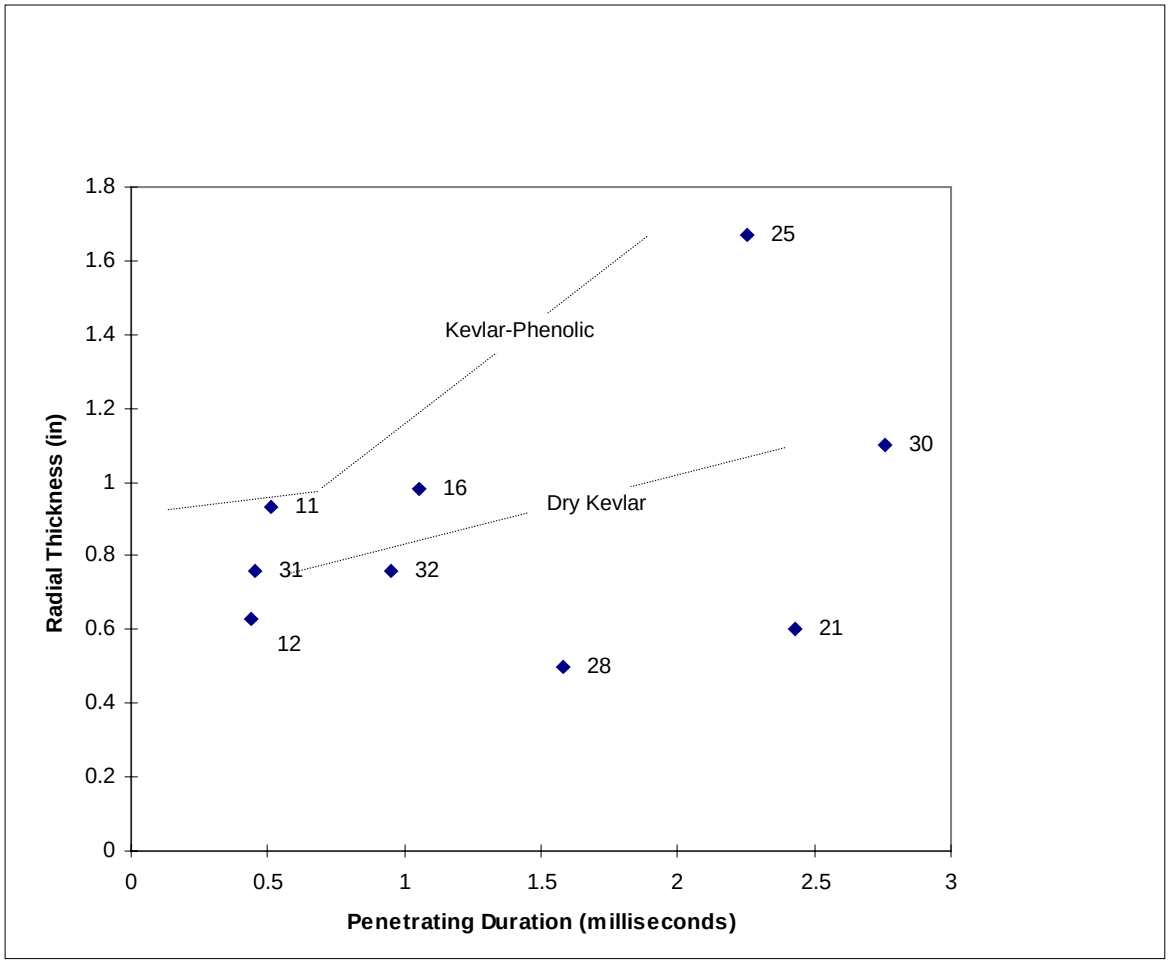

SYSTEMS

Ring 12: Titanium-Kevlar-Phenolic
Ring 21: Steel-Fiberglass-Polyester
Rings 11, 16, and 25: Kevlar-Phenolic
Ring 31: Fiberglass-Aluminum
Ring 28: Fiberglass Polyester
Rings 32 and 30: Kevlar-Aluminum

FIGURE 50. THICKNESS INCREASE VERSUS PENETRATING DURATION

Tables 5 and 6 summarizes the kinetic energy per weight, energy per thickness, and rankings of the ten systems selected in order from the highest to lowest ranking.

Based on the energy per weight and thickness, as seen in tables 5 and 6, the aluminum-lined fiberglass system has the highest energy per weight, 62 kips/lb, and hence has the highest KE_w ranking. The titanium system has the highest energy per thickness ranking, 2,168 kips/in, and hence has the highest KE_t ranking. A combined ranking score was established by multiplying the weight to thickness rankings. Fiberglass impregnated with phenolic resin has the highest score as seen in table 7. The aluminum-lined fiberglass system came in second. The fiberglass impregnated with polyester came in third. Since the energy per weight is considered critical, the aluminum-lined fiberglass system, therefore, represents an optimum system based on its energy per weight. It is interesting to recognize that three out of the top five systems in E_w ranking had fiberglass. Four out of the top five systems in E_t had fiberglass. In the combined rankings, four out of the top five systems were also fiberglass.

TABLE 5. RANKINGS OF CONTAINMENT RINGS BASED ON ENERGY PER WEIGHT (CONTAINED ALL FRAGMENTS)

Ring No.	Materials	KE/W_t x1000 (in.lbs/lb)	Rankings
36	Fiberglass-Al Liner	62	10
33	Kevlar-Al Liner	57	9
26	Fiberglass-Phenolic	51	8
22	Kevlar 29	50	7
17	Fiberglass-Polyester	49	6
15	Ti-Kevlar-Phenolic	36	5
1	Kevlar 29-Phenolic	34	4
19	Steel-Fiberglass-Polyester	31	3
18	Titanium (6A14V)	31	2
13	Steel-Fiberglass-Phenolic	30	1

TABLE 6. RANKINGS OF CONTAINMENT RINGS BASED ON ENERGY PER THICKNESS (CONTAINED ALL FRAGMENTS)

Ring No.	Materials	KE/t_r x1000 (in.lbs/in)	Rankings
18	Titanium (6A14V)	2168	10
13	Steel-Fiberglass-Phenolic	1698	9
26	Fiberglass-Phenolic	1650	8
19	Steel-Fiberglass-Polyester	1591	7
17	Fiberglass-Polyester	1527	6
15	Ti-Kevlar-Phenolic	1347	5
36	Fiberglass- Al Liner	1303	4
33	Kevlar 29-Al Liner	910	3
22	Kevlar 29	605	2
1	Kevlar 29-Phenolic	598	1

TABLE 7. COMBINED RANKINGS OF CONTAINMENT RINGS
(CONTAINED ALL FRAGMENTS)

Ring No.	Materials	Weight Rankings	Thickness Rankings	Combined Ranking Scores
26	Fiberglass-Phenolic	8	8	64
36	Fiberglass- Al Liner	10	4	40
17	Fiberglass-Polyester	6	6	36
33	Fiberglass-Al Liner	9	3	27
15	Ti-Kevlar-Phenolic	5	5	25
19	Steel-Fiberglass-Polyester	3	7	21
18	Titanium (6A14V)	2	10	20
22	Kevlar 29	7	2	14
13	Steel-Fiberglass-Phenolic	1	9	9
1	Kevlar 29-Phenolic	4	1	4

Based on the results of phase 1, the aluminum lined fiberglass ring was the best system so far, and it was selected for further testing under elevated temperatures. Three OCF S2 dry fiberglass, bonded to a 0.0625-inch aluminum liner by GE SR240 silicon, containment rings were fabricated. Only ring 40 contained all rotor fragments under elevated temperatures. However, a small hole, approximately one inch, was found on the ring. It appeared that a small fragment, probably a small piece of blade debris with low energy, penetrated the containment ring. By the time blade debris escaped the ring, its energy was further reduced due to energy absorption of the ring and, hence, probably became less harmful.

Three type "J" thermocouples (TCs) were used for ring 40 and located at the laminate/aluminum interface, at the 22nd, and at the 43rd ply. TCs 2 and 3 were fiberglass insulated and able to withstand the higher temperatures better than the Teflon sleeved wire. Normalized weight and thickness of ring 40 were 30.27 lbs and 2.10 inches. KE_w and KE_t were 31 kips/lb and 432 kips/in respectively. One disc fragment penetrated and escaped ring 38. Another disc fragment penetrated and almost escaped the ring. Tables 8 and 9 show the containment ring characteristics and their performance. Figures 51 shows the posttest pictures of ring 38. Figure 52 shows the failure event of rings 38. Figure 53 shows the failure event and pre- and posttest pictures of ring 40.

TABLE 8. HEATED CONTAINMENT RINGS

Ring No.	Materials	Weight (lbs)	Normalized Weight (lbs)	Radial Thickness (in)	Axial Length (in)	No. of High-Speed Photos	Failed Speed (rpm)	Contained (C) or Not Contained (NC)	Test Temperature (°F)
38	Fiberglass-Al Liner	19.00	18.83	0.63/063	9.08	48	21260	NC	596-869
39	Fiberglass-Al Liner	29.00	29.00	0.94/0.063	9.00	0	20400	NC	510-780
40	Fiberglass-Al Liner	37.00	30.27	2.1/0.06	11.00	50	20224	C	504-878

TABLE 9. HEATED CONTAINMENT RING PERFORMANCE
(CONTAINED ALL FRAGMENTS)

Ring No.	Materials	Weight (lbs)	Normalized Weight (lbs)	Radial Thickness (in)	Axial Length (in)	KE_w x1000 in-lbs/lb	KE_t x1000 in-lbs/in	Contained (C) or Not Contained (NC)	Test Temperature (°F)
40	Fiberglass-Al Liner	37.00	30.27	2.1/0.06	11.00	31	432	C	504-878

Under the high temperature, the absorption capability of the fiberglass material is significantly reduced. This reduction results in an increase of approximately 92 percent in material weight and 304 percent in thickness. Its E_w and E_t are reduced about 50 and 33 percent respectively.

It may not be correct to assume that all other composite systems would behave exactly similar to the fiberglass system under the high temperature. Other composite systems, i.e., dry aramid or aramid impregnated with different types of resins, could have been selected for testing under the high temperature to assess their performance and compare it with the performance of the fiberglass system. Aramid, such as Kevlar 29, performed almost the same as fiberglass at ambient temperature. Only the fiberglass system was selected for high temperature testing.

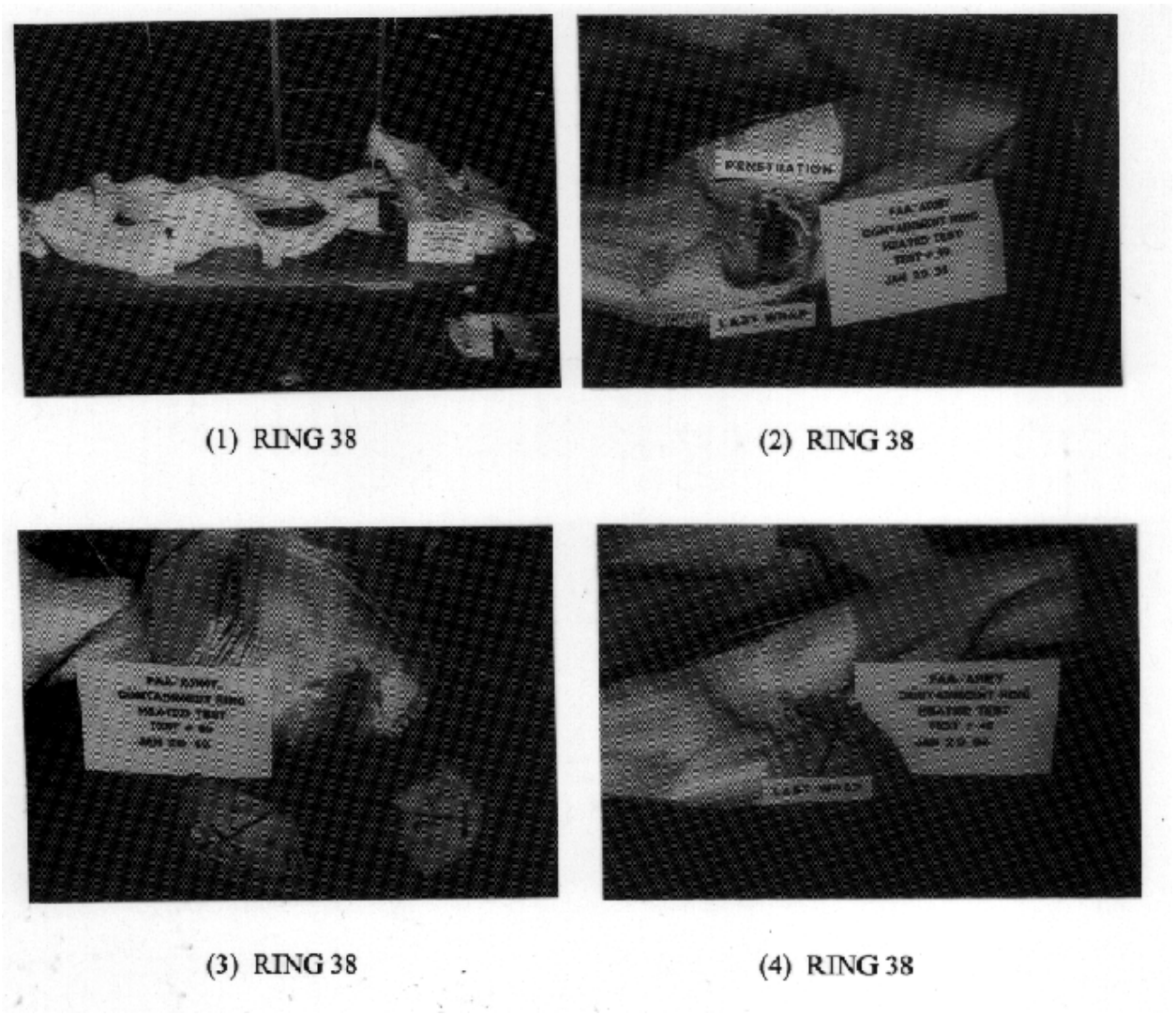

(1) RING 38

(2) RING 38

(3) RING 38

(4) RING 38

FIGURE 51. POSTTEST PICTURES OF RING 38

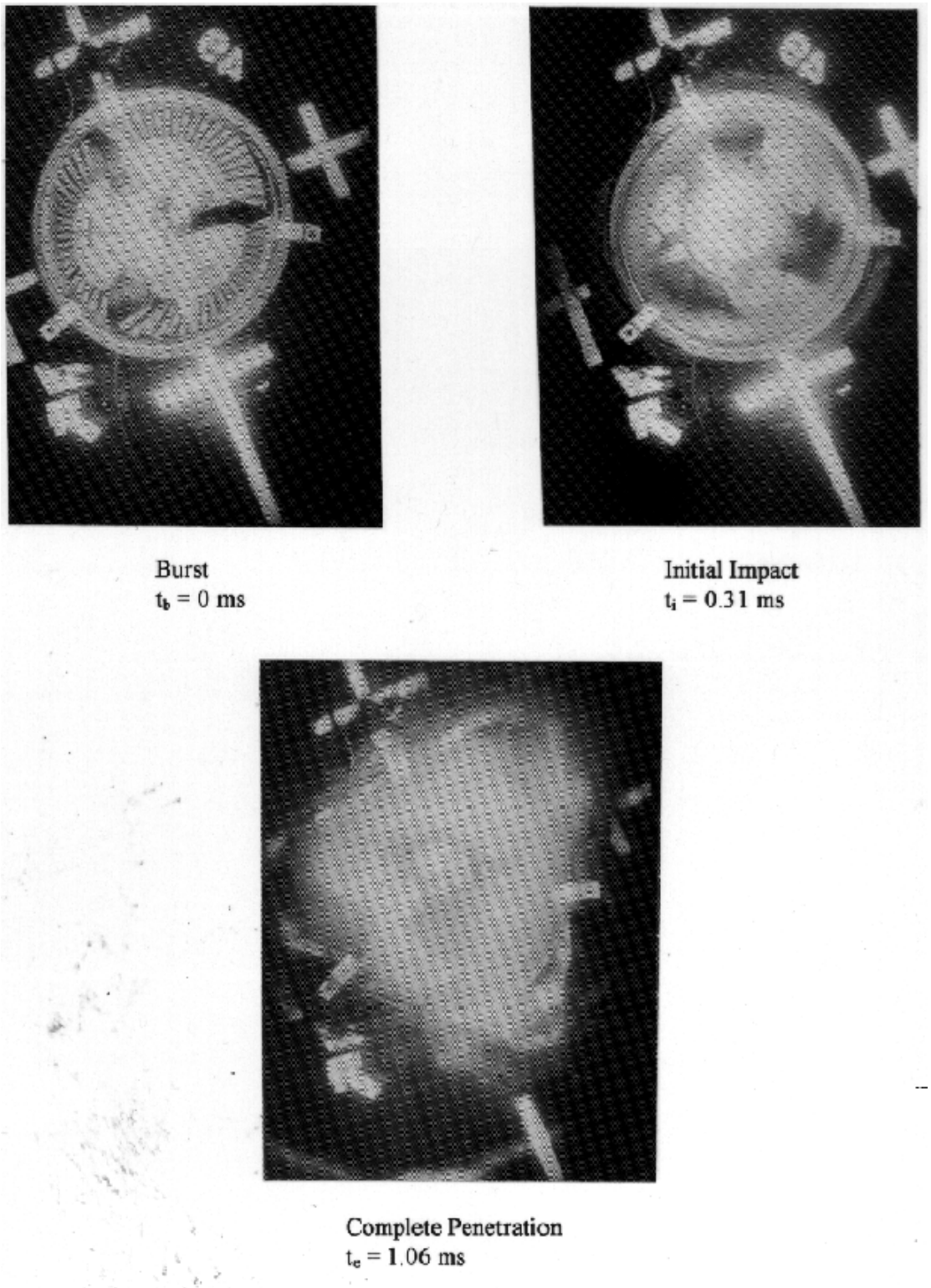

FIGURE 52. FAILURE EVENT OF RING 38

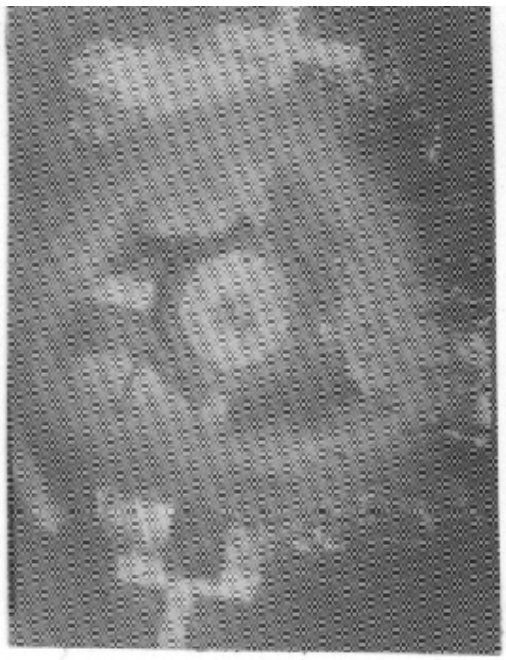

Burst
t_b = 0 ms

Initial Impact
t_i = unknown

Last Recorded Event
t_l = 3 ms

(1) FAILURE EVENT OF RING 40

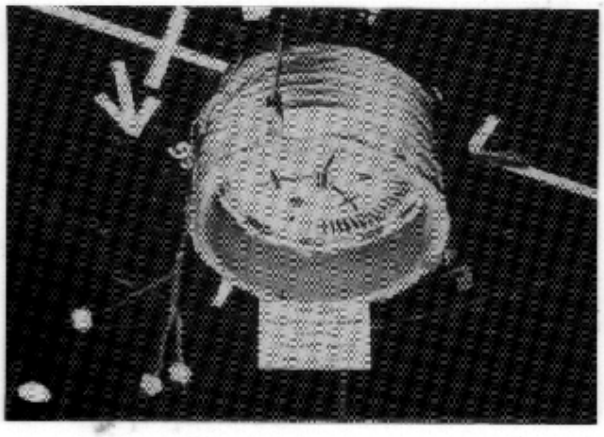

(2) RING 40 BEFORE TESTING

(3) RING 40 AFTER TESTING

FIGURE 53. FAILURE EVENT AND PRE/POSTTEST PICTURES OF RING 40

7. CONCLUSIONS.

a. Under phase 1, based on the energy per weight, we have successfully identified fiberglass as the best lightweight material so far. Dry aramid, Kevlar 29, with an aluminum liner performed almost as effectively as fiberglass under ambient conditions.

b. Fiberglass systems, with compromised weight and thickness, still outperformed other composite systems.

c. Based on the energy per weight or thickness, dry Kevlar 29 performed better than Kevlar impregnated with phenolic resin. Dry Kevlar appeared to prolong the penetrating duration.

d. Under the average temperature of 691°F, in phase 2, the performances of the aluminum lined fiberglass system, based on energy per weight and thickness, are reduced by 50 and 33 percent respectively. An increase of 92 percent in containment ring weight and 304 percent in its thickness are required to compensate for the degradation of the fiberglass system under high temperatures.

e. Fabric composite systems absorbed the kinetic energy of fragments through elastic deformation and interlaminated shear of composite layers. No evidence of tensile failure of fibers existed.

8. REFERENCES.

1. Deluca, J. J., Development of Turbine Containment for Aircraft, Ph.D. Thesis, University of Lowell, Lowell, MA, September 1991.

2. Mascianica, F. S., Ballistic Technology of Lightweight Armor—1979 (U), pg. 566, AMMRC TR 79—10, February 1979.

3. Dy, L. D., Aircraft Engine Fragment Containment Simulation Theory and Application, M.S. Thesis, The Pennsylvania State University, Malvern, October 1992.

4. Cheng, W. F. and Han, D. J., Plasticity for Structure Engineers, pages 409-427, New York: Spring-Verlag New York Inc., 1988.

APPENDIX A—KINETIC ENERGY OF DISK FRAGMENTS

The transitional kinetic energy of the pie-shaped sector is

$$KE_t = \frac{1}{2}mV^2 = \frac{1}{2}m(\bar{r}\,\omega)^2 \tag{1}$$

where V is the centroid linear velocity of mass m with angular velocity ω with respect to y axis

$$m = \rho\upsilon \tag{2}$$

where ρ is the density and υ is the volume of the sector.

Assume ϕ is very small, then

$$\upsilon = \int_{ri}^{r0} r\phi\, t\, dr \tag{3}$$

where

$$t = \frac{dt(r)}{dr} = t'(r)$$

Substitute equation 3 into equation 2, we obtain

$$m = \rho\phi \int_{ri}^{r0} rt'(r)dr = \rho\ \phi R_y \tag{4}$$

where R_y is the first moment of dA with respect to y axis.

Also

$$\bar{r}\,A = \int_{ri}^{r0} \bar{r}_{el}\,dA \tag{5}$$

where $\bar{r}_{el}$ is the centroid of element dA as seen in figure A.1.

Since

$$\bar{r}_{el} = \frac{r\sin\phi}{\phi} \tag{6}$$

$$dA = tdr = t'(r)dr \tag{7}$$

$$A = \int_{ri}^{r0} t'(r)dr \tag{8}$$

Substitute equations 6, 7, and 8 into equation 5, then

$$\bar{r} = \frac{\int_{ri}^{r0} \frac{\sin\phi}{\phi} rt'(r)\, dr}{\int_{ri}^{r0} t'(r) dr} \tag{9}$$

Multiply the denominator and nominator of equation 9 by $\frac{r}{r}$, we have

$$\bar{r} = \frac{\frac{\sin\phi}{\phi} \int_{ri}^{r0} r^2 t'(r) dr}{\int_{ri}^{r0} rt'(r) dr} \tag{10}$$

Let R_y and M_y be the first and second moment of dA with respect to y axis, then

$$R_y = \int_{ri}^{r0} rt'(r) dr \tag{11}$$

and

$$M_y = \int_{ri}^{r0} r^2 t'(r)\, dr \tag{12}$$

Substitute R_y and M_y into equation 10, we obtain

$$\bar{r} = \frac{\sin\phi}{\phi} \cdot \frac{M_y}{R_y} \tag{13}$$

Therefore,

$$V = \bar{r}\,\omega = \frac{\sin\phi}{\phi} \cdot \frac{M_y}{R_y}\omega \tag{14}$$

Substitute equations 4 and 14 into equation 1, we obtain

$$KE_t = \frac{1}{2} mv^2 = \frac{1}{2} \rho\omega^2 \frac{\sin^2\phi M_y^{\,2}}{\phi R_y} \tag{15}$$

First and second moment of dA, as seen in figure A.2, with respect to y axis are also expressed as

$$R_y = \int_A r dA = \int_A (\bar{r} + r')dA = \int_A \bar{r}\, dA + \int_A r'dA = \bar{r} A \quad (16)$$

where

$\int_A \bar{r}\, dA = \bar{r} A$ and $\int_A r'dA = r'A = 0$ as area A rotates about its own axis AA'

$$M_y = \int_A r^2 dA = \int_A (\bar{r} + r')^2 dA = \int_A (\bar{r}^2 dA + 2\bar{r}\, r'dA + r'^2 dA)$$

$\int_A \bar{r}^2 dA = A\bar{r}^2$

$2\bar{r}\int_A r'dA = 2\bar{r}\, r'A = 0$ as area A rotates about its own axis AA'

$\int_A r'^2 dA = M_{AA'}$

Therefore,

$$M_y = M_{AA'} + A\bar{r}^2$$

Also $M_{AA'} = k_g^2 A$ where k_g is the radius of gyration of area A with respect to y axis.

$$M_y = k_g^2 A + A\bar{r}^2 = (k_g^2 + \bar{r}^2)A \quad (17)$$

Finally,

$$KE_t = \frac{\rho\varpi^2 \sin^2\phi\left[\left(k_g^2 + \bar{r}\right)\right]^2 A}{2\phi\bar{r}} \quad (18)$$

The maximum translational kinetic energy occurs when equation 18 is minimized. Let

$$u = \sin^2\phi\ ,\ \frac{du}{d\phi} = 2\sin\phi\cos\phi \quad (19)$$

$$v = \phi\ ,\frac{dv}{d\phi} = 1 \quad (20)$$

$$\frac{d(KE_t)}{d\phi} = \frac{\rho A\varpi^2\left(k_g^2 + \bar{r}^2\right)^2\left[2\phi\sin\phi\cos\phi - \sin^2\phi\right]}{2\phi^2\bar{r}} = 0 \quad (21)$$

Solving equation 21 gives the maximum translational kinetic energy at ϕ = 66.8°. The maximum translational kinetic energy of the whole sector (2ϕ) is, therefore, 133.6°.

The rotational kinetic energy can be calculated from

$$KE_{total} = KE_t + KE_r \tag{22}$$

where

$$KE_{total} = \frac{1}{2} mv^2 + \frac{1}{2} M_y \omega^2 \tag{23}$$

and M_y is the second moment of inertia of the fragment with respect to y axis.

The distributions of the translational and rotational kinetic energy, therefore, are

$$KE_t\ (\%) = \frac{KE_t}{KE_{total}} \tag{24}$$

or

$$KE_r\ (\%) = \frac{KE_r}{KE_{total}} = [1 - KE_t\ (\%)] \times 100 \tag{25}$$

LEGENDS:

r_i:	inner radius
r_0:	outer radius
dr:	derivative of r
t:	disc thickness
ϕ:	sector angle
t(r):	t as function of r
dA:	element
ω:	angular velocity

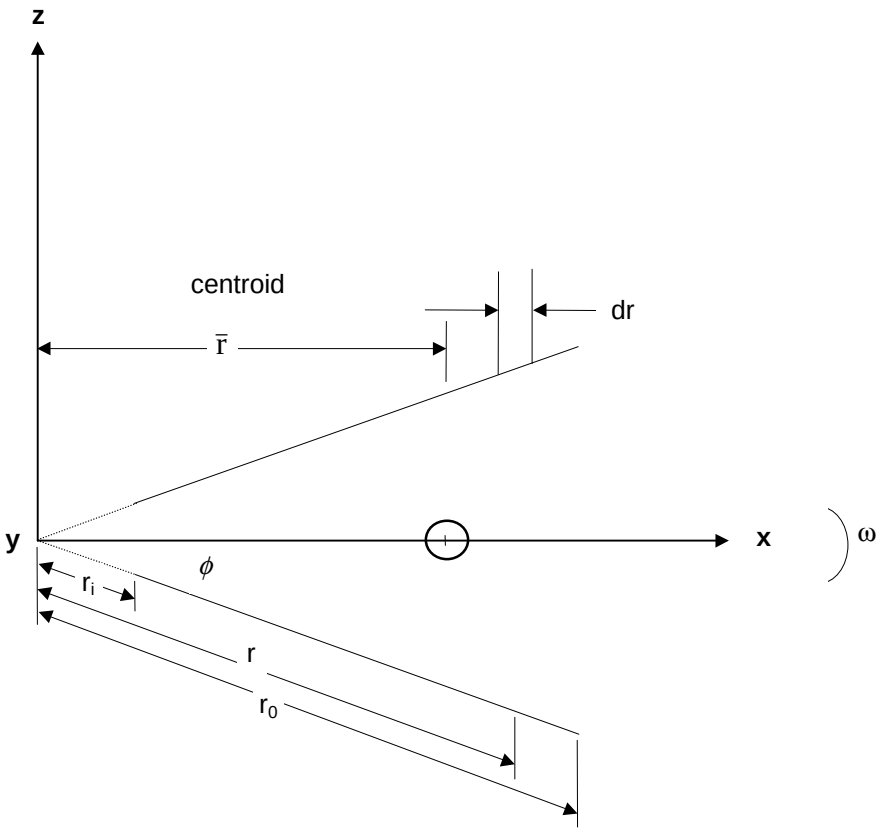

FIGURE A-1. A PIE-SHAPED SECTOR OF THE ROTOR

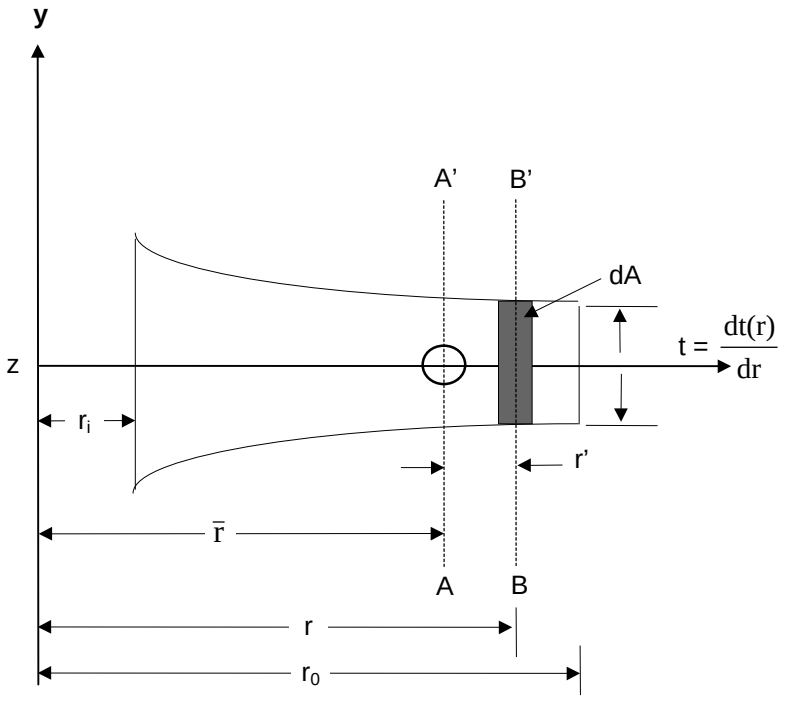

FIGURE A-2. CROSS SECTION OF A ROTOR

APPENDIX B—ROTOR FRAGMENT GENERATOR ANALYSIS

Limit analysis is used to calculate the size of one or more precut notches. These notches will cause the failure of the rotor at a speed which produces 1.0 x 10^6 in-lbs of the kinetic energy.

To simplify the problem, assume that the T53 turbine rotor was made of an elastic, perfectly plastic material and was notched as shown in figure B-1. As the rotor is gradually spinning, starting from the center of the rotor, the rotor grows elastically until the stress located at the high stress concentration area reaches the yield stress.

$$\sigma_{ij} = \sigma_y \tag{1}$$

In this case, the plastic zone will initially start from the end of the cut, point A, and move inward to the inner radius surface of the rotor. Further increases in speed will cause the plastic zone to spread, but it is still contained inside the elastic zone. As the rotor approaches its burst speed,

$$N = N_{burst} \tag{2}$$

The elastic zone is no longer dominant, and the entire section from point A to the inner radius is covered by the plastic zone. Theoretically, point A′ will experience the same yield process and eventually reach the ultimate stress at the same time as point A. At this burst speed, the material of the rotor reaches its limit stress or ultimate stress, and the rotor will burst into a predetermined number of fragments.

According to Chen and Han [4], when an equilibrium stress distribution which balances the applied load is found, plastic flow will not occur. From the equilibrium stress distribution, a lower bound solution for the size of the notches can therefore be estimated.

An upper bound solution is determined by equating the rate of the work done by the external forces to the rate of the internal energy dissipation. The upper bound theorem considers only the compatible velocity field which satisfies the constraints, and the stress distribution is not necessary in equilibrium.

As a simplification, assume that the disk was spinning and was broken in half by the centripetal force applied to the unnotched region as shown in figure B-2. The variable b defines the distance from the center of the disk to the end of the cut (b-cut), a defines the inner radius and t defines the thickness of the disk which is assumed to be constant. Then (b - a) is the length of the material left after cutting. The internal stress in the contract area may be expressed as,

$$\sigma_i = \frac{F_c}{2(b-a)t} \tag{3}$$

or

$$F_c = 2(b - a)t\sigma_i \tag{3a}$$

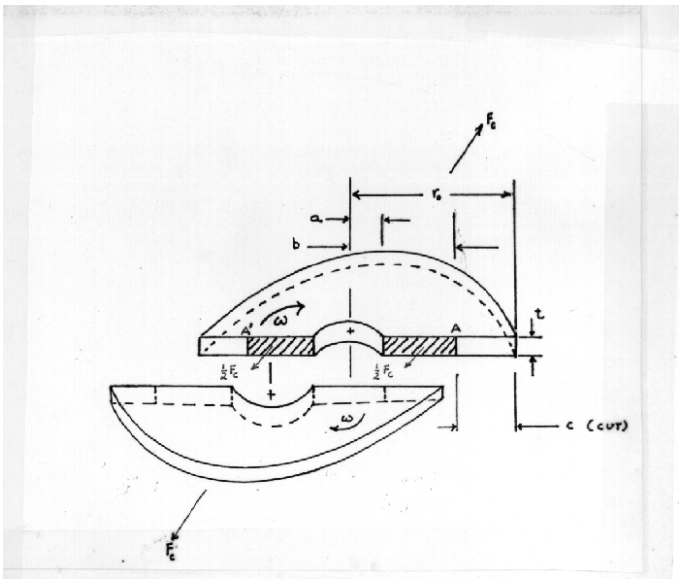

LEGENDS:

a	=	disk inner radius
b	=	slot terminal radius
r_0	=	outer disk radius
F_c	=	centripetal force
t	=	disk thickness
ω	=	angular velocity
c	=	cut length

FIGURE B-1. NOTCHED DISK LIMIT ANALYSIS DIAGRAM

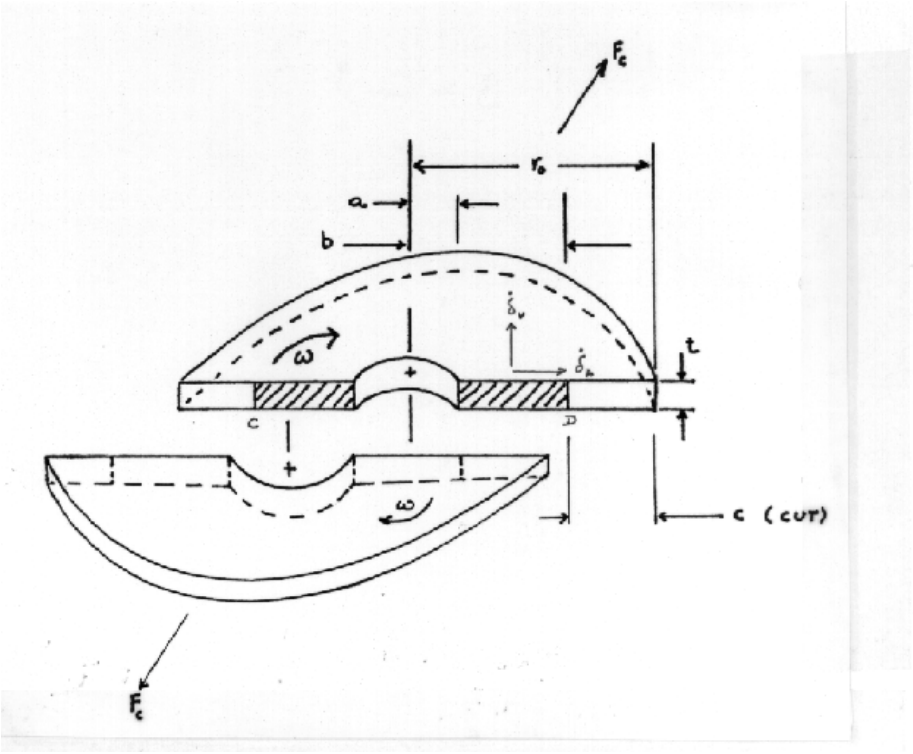

FIGURE B-2. VELOCITY FIELD OF THE NOTCHED DISK AT FAILURE

but $$F_c = m\ddot{a} \tag{3b}$$

and $$m = \frac{W_t}{g} \tag{3c}$$

then

$$\ddot{a} = \bar{r}\,\omega^2 = \frac{\bar{r}\,\pi^2 N^2}{900} \tag{3d}$$

where

m	=	mass of fragment
w_t	=	fragment weight
g	=	gravity constant

$\bar{r}$	=	fragment centroid
ω	=	angular velocity

N = rotation per minute

ä = acceleration

a = inner radius

equations 3-3d can be combined as

$$\frac{w_t \bar{r} \pi^2 N^2}{900g} = (2)(b - a)t\sigma_i \qquad (4)$$

At collapse, $\sigma_i = \sigma_u$ = ultimate stress. Substituting σ_u into equation 4 yields

$$\frac{w_t \bar{r} \pi^2 N^2}{900g} = (2)(b - a)t\sigma_u \qquad (4a)$$

or

$$b = a + \frac{w_t \bar{r} \pi^2 N^2}{1800gt\sigma_u} \qquad (4b)$$

Let c equal the minimum cut length and r_0 be the outer radius of the disk, then

$$b = r_0 - c \qquad (5)$$

equation 4b becomes

$$c = (r_0 - a) - \frac{w_t \bar{r} \pi^2 N^2}{1800gt\sigma_u} \qquad (6)$$

Equation 4b gives us the lower bound solution which predicts that at burst or collapse speed the actual b-cut would be equal or larger than the lower bound b-cut, b_1.

Figure B-2 shows the kinematically admissible velocity field in which the upper and lower half of the disk move as rigid bodies relative to each other along plane CD. If the relative velocity of plane CD is δ_h, then, the internal energy dissipation is

$$Di = (1 \text{ cut})(2k)(b-a)t\delta_h \qquad (7)$$

where k is the yield parameter or collapse parameter in this case.

If the velocity at which the upper and lower disk are separated is δ_v, the external work is

$$D_e = F_c\delta_v = \frac{w_t \bar{r} \pi^2 N^2 \delta_v}{900g} \tag{8}$$

By setting equation 7 equal to equation 8, the upper bound b-cut solution may be derived,

$$(1 \text{ cut})(2k)(b-a)t\delta_h = \frac{w_t \bar{r} \pi^2 N^2 \delta_v}{900g} \tag{9}$$

Due to symmetry,

$$\delta_h = \delta_v$$

then,

$$b = a + \frac{w_t \bar{r} \pi^2 N^2}{1800gtk} \tag{10}$$

The cut is obtained as

$$c = (r_0 - a) - \frac{w_t \bar{r} \pi^2 N^2}{1800gtk} \tag{11}$$

Since we model the disk as an elastic, perfectly plastic material, no work-hardening exists, then the stress in the disk may be assumed to be constant after yielding. Also since we are interested only in the disk burst, then

$$\sigma_y = \sigma_u \tag{12}$$

The maximum shear stress or Tresca yield criterion predicts that yielding will occur where the constant k reaches a critical value such that

$$k = \frac{\sigma_u}{2} \tag{12a}$$

Substituting equation 12a into equation 10 yields

$$b = a + \frac{w_t \bar{r} \pi^2 N^2}{900gt\sigma_u} \tag{13}$$

The distortion energy or Von Mises yield criterion predicts that k may be expressed as

$$k = \frac{\sigma_u}{3^{1/2}} \tag{13a}$$

After the appropriate substitution of equation 13a, equation 10 becomes

$$b = a + \frac{w_t \bar{r} \pi^2 N^2}{1039 g t \sigma_u} \tag{14}$$

Figure B-3 shows the plot of speed versus the b-cut length which begins at the end of the cut and stops at the disk center. From the experimental test data, the actual b-cut curve when plotted lies to the right of the lower bound curve and is close to it. The two lines on the right side of the actual b-cut curve demonstrate the difference between Von Mises and Tresca yield criteria, and the Von Mises yield criterion seems to be closer to the true b-cut than Tresca. The area between the lower bound and Von Mises upper bound curves therefore estimates the b-cut length corresponding to the design speed.

Due to the aging of the rotors which had been used in service, however, there is a definite discrepancy between the design and test data. The lower and upper bound b-cut curves are, therefore, sufficient to represent the fragment generator design guide curve for the T53 turbine rotors.

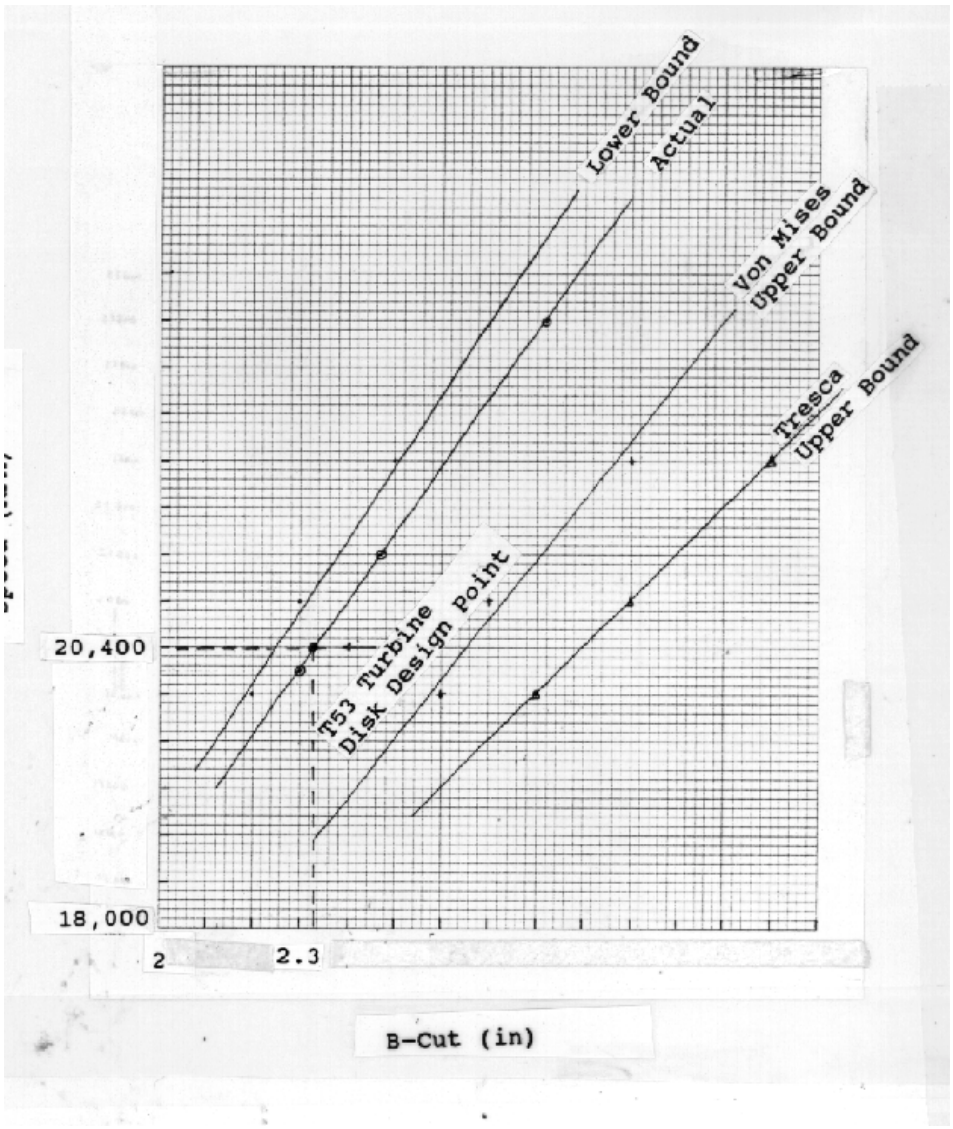

FIGURE B-3. DESIGNED b-CUT LENGTH VERSUS EXPERIMENTAL b-CUT LENGTH